Philipp Emanuel Brunner, BSc

Nanoporous Structure of Dealloyed Metals Investigated by Electrochemical Impedance Spectroscopy

MASTER'S THESIS

to achieve the university degree of

Diplom-Ingenieur

Master's degree programme: Technical Physics

submitted to

Graz University of Technology

Supervisor

Univ.-Prof. Dipl.-Phys. Dr.rer.nat. Roland Würschum

Co-Supervisor
Dipl.-Ing. Dr.techn. Eva-Maria Steyskal

Institute of Materials Physics

Graz, November 2018

AFFIDAVIT

I declare that I have authored this thesis independently, that I have not used other than the declared sources/resources, and that I have explicitly indicated all material which has been quoted either literally or by content from the sources used. The text document uploaded to TUGRAZonline is identical to the present master‘s thesis.

Date

Signature

Abstract

Characterization of nanoporous metals produced by electrochemical dealloying is in the focus of current research. By analyzing the porosity of nanoporous metals, key structural parameters, such as pore size, pore shape, and total surface area can be determined. In this master's thesis, the potentials of electrochemical impedance spectroscopy (EIS) are explored for the characterization of nanoporous metals. These studies were supplemented by the method of cyclic voltammetry (CV), which is a standard technique in this field of research.

In this thesis, nanoporous gold (npAu) and palladium (npPd) were investigated. They have been prepared by electrochemical dealloying the less noble component of the initial alloys ($Ag_{75}Au_{25}$ and $Co_{75}Pd_{25}$). Different states before and after dealloying as well as after electrochemical reduction can be distinguished by the different shapes of the impedance spectra. One key issue of this master's thesis was the fitting of the measured spectra with equivalent circuits. This analysis is performed based on models by de Levie, Keiser, and Eloot found in literature. The various components of the circuits were assigned to the corresponding parts of the spectra and yielded a deeper understanding of the processes taking place. From such equivalent circuits, the pore resistance R_{pore}, the double layer capacitance C_{tot}, and the specific surface area α were deduced. Furthermore the pore radius, the pore length, and the number of pores was estimated. By considering these parameters, a pore radius of about $10 - 15$ nm was obtained for npAu, which is in good accordance with literature. For nanoporous palladium the evaluation gave a pore radius of about $2 - 4$ nm, which is slightly too low in comparison with values cited in literature. The shape of the pores can also be estimated from the impedance spectrum in the Nyquist plot representation. All investigated nanoporous samples had a convex pore geometry (rhombohedral or deltoid like pore shapes). From the pore length, the tortuosity of the pores could be estimated. This gave further insights into the pore structure. For coarsened nanoporous gold samples significant changes in the pore parameters and the pore shape were observed. Samples aged at higher temperatures showed a larger change in their pore parameters. Significant changes in the impedance spectra occured in electrochemically active regions, especially for hydrogen absorption in nanoporous palladium.

Kurzfassung

Die Charakterisierung nanoporöser Metalle, hergestellt durch elektrochemisches Dealloying, ist Gegenstand aktueller Forschung. Die Untersuchung der Porosität nanoporöser Metalle ermöglicht die Bestimmung wichtiger Parameter, wie z.B. der Porengröße, der Porenform und der Gesamtoberfläche der Probe. In dieser Masterarbeit wurden die Anwendungspotenziale der elektrochemischen Impedanzspektroskopie (EIS) für die Charakterisierung nanoporöser Metalle getestet. Diese Untersuchungen wurden durch Zyklovoltammetrie, eine Standardtechnik in diesem Forschungsgebiet, unterstützt.

In dieser Arbeit wurden nanoporöses Gold (npAu) und Palladium (npPd) untersucht. Diese sind durch elektrochemisches Dealloying der weniger edleren Komponente der Ausgangslegierung ($Ag_{75}Au_{25}$ und $Co_{75}Pd_{25}$) hergestellt worden. Impedanzspektren wurden sowohl vor und nach Dealloying als auch nach elektrochemischer Reduktion aufgenommen. Einen Schwerpunkt der Masterarbeit bildete die quantitative Analyse der gemessenen Spektren mit Hilfe von Ersatzschaltkreisen. Diese Analyse erfolgte auf Grundlagen von Modellen nach de Levie, Keiser bzw. Eloot, die aus der Literatur bekannt sind. Die verschiedenen Komponenten der Schaltkreise wurden den entsprechenden Abschnitten der Spektren zugeordnet und ermöglichten ein tieferes Verständnis der stattfindenden Prozesse. Anhand der Ersatzschaltkreise konnten der Porenwiderstand R_{pore}, die Doppelschichtkapazität C_{tot} und die spezifische Oberfläche α bestimmt werden. Weiters wurden der Porenradius, die Porenlänge und die Anzahl der Poren ermittelt. Für nanoporöses Gold wurde ein Porenradius von ungefähr $10 - 15$ nm bestimmt. Diese Werte sind in guter Übereinstimmung mit der Literatur. Für nanoporöses Palladium wurde ein Porenradius von ungefähr $2 - 4$ nm errechnet, der im Vergleich zu Literaturwerten etwas zu niedrig ist. Auch die Porenform konnte von den Impedanzspektren abgeleitet werden. Alle untersuchten nanoporösen Proben wiesen eine mehr oder weniger konvexe Porengeometrie auf (rhomboedrische oder Deltoid förmige Poren). Ferner konnte aus der Porenlänge die Tortuosität der Poren abgeschätzt werden. Dies gab weitere Einblicke in die Porenstruktur. Vergröberung der nanoporösen Goldproben führte zu signifikanten Veränderungen in den Porenparametern und in der Porenform. Proben, die bei höheren Temperaturen vergröbert wurden, zeigten größere Veränderungen in den Porenparametern. Signifikante Unterschiede in den Impedanzspektren wurden in elektrochemisch aktiven Spannungsbereichen beobachtet, vor allem bei der Wasserstoffabsorption in nanoporösem Palladium.

Contents

1 Introduction

In the last few decades, nanoscience and nanotechnology dealt with the development of nanomaterials with the aim to produce nanoparticles, nanowires and other quantum nanostructures. Instead of discovering new materials by trial-and-error, nanomaterials can be designed systematically. The properties of such structures strongly depend on their size[1].

A branch of nanomaterials possess a nanoporous structure with a porosity between 0.20 and 0.95. In such systems the pores are as important as the remaining bulk material. Typical pore diameters are between 1 – 100 nm. The pores can be straight, curved or twisted, which is described by the tortuosity of the material. A characteristic feature of nanoporous materials is the high surface to volume ratio, with a high surface area and a large porosity[1]. Especially nanoporous metal foams, as used in this master's thesis, have big advantages compared to the corresponding bulk materials. They combine characteristic properties of metals, such as the good conductivity, catalytic activity and ductility with nanoscale properties as a high surface area and a large porosity[2]. Typical fields of application of nanoporous metals are catalysis, sensing, actuation, electronic and ultracapacitor materials, high-temperature templates and battery anodes[3]. Palladium is known for the capability to absorb hydrogen. Therefore nanoporous palladium with a larger surface area is even better suitable for hydrogen storage, which can be labeled as further application.[4,5].

Beside templating and versatile sol-gel approaches, dealloying plays an important role in the formation of nanoporous metals[2]. Although dealloying was known for a long time in the context of corrosion, since 2001 this process becomes a standard technique to fabricate high-surface-area nanoporous metals. By dissolving the less noble components of an alloy, a nanoporous structure is formed[3].

To investigate the structure of nanoporous materials, electron microscopy is very helpful, but also X-ray photoelectron spectroscopy or auger spectroscopy can be used[2]. With cyclic voltammetry measurements, the nanoporous surface area and out of it the ligament size can be determined[6]. Since in the 1960s de Levie developed his elegant work about the theory of porous electrodes and the extansions on this theory by Keiser, electrochemical impedance spectroscopy (EIS) can also be used to investigate such systems. EIS offers the opportunity to get information about the nanoporous structure, like the pore shape, and to calculate the surface area and pore parameters, as the pore radius, the pore length and the number of pores[7].

The power of electrochemical impedance spectroscopy originates from several aspects. A main advantage compared to a steady state method, as cyclic voltammetry, is the huge frequency range used during measurements. Therefore the impedance contains almost all of the information that can be obtained from the system. EIS data are often fitted and interpreted in terms of electrical equivalent circuits. Since such a circuit is only a model, the gained information about the involved physico-electrochemical processes is limited [7].

In the present work, electrochemical impedance spectroscopy is introduced in the research group of the Institute of Materials Physics. By characterizing those nanoporous metals which are in the focus of research at the institute, the potentials of this technique were explored. For this purpose, the obtained results have been compared with already known ones from steady state methods. These techniques are well established at the institute.

In the first part of this master's thesis, different models are used to determine suitable equivalent circuits for nanoporous electrodes. The obtained pore resistances and total capacities are compared and spectra at different potentials are recorded. The second part deals with a further analysis of the equivalent circuit with the aim to assign the different parts of the spectrum to the corresponding parts of the circuit. Furthermore the pore structure is determined and pore parameters like the pore radius, the pore length and the number of pores are calculated. The obtained results are analyzed and deviations from literature are discussed. Nanoporous gold and palladium are used as samples and are produced via electrochemical dealloying.

2 Fundamentals

2.1 Fundamentals of Electrochemistry

In electrochemistry, structures and processes at the interface between an electrode and an electrolyte are studied. The electrode is an electronic, the electrolyte an ionic conductor. In this field of research a typical system is the metal-solution interface. This interface is charged, which results from an excess charge of the metal surface and is balanced by a charge of equal magnitude and opposite sign on the solution side of the interface[8]. This different charge distribution is a result of the different electro-chemical potentials μ_i of electrode and electrolyte. If $\mu_\mathrm{electrode} > \mu_\mathrm{electrolyte}$, the electrode (metal) gets negatively and, therefore, the electrolyte side positively charged, if $\mu_\mathrm{electrode} > \mu_\mathrm{electrolyte}$ the opposite occurs, the metal gets positively and the electrolyte side negatively charged. In the end, the two chemical potential have to be equal. To achieve such a condition, the electrolyte has to contain substances that can be converted into one another by oxidation (loss of electrons) or reduction (acceptance of electrons). Because of charge conservation these reactions occur pairwise. Thereby, the electrode acts in that case as electron donor or acceptor and gets charged. The equilibrium Galvani voltage $\Delta\phi_0$ between the electrode and the electrolyte is given by the Nernst equation[9]:

$$\Delta\phi_0 = \Delta\phi_{00} + \frac{RT}{nF} \ln \frac{a_\mathrm{ox}}{a_\mathrm{red}}. \tag{1}$$

In equation (1), $\Delta\phi_{00}$ denotes the standard Galvani potential difference, R the gas constant, T the temperature, n the number of electrons, F the Faraday constant and a_ox and a_red are the activity of the oxidized or reduced species of the electrolyte[9]. The equilibrium Galvani potential $\Delta\phi_0$ is typically about 1 V[8]. In equilibrium no current flow occurs[9].

Since the Galvani voltage can not be measured directly, a standard hydrogen electrode (SHE) is used as a reference point. So the standard Galvani potential ϕ_{00} of the SHE half reaction ($2\,\mathrm{H^+_{aq}} + 2\,\mathrm{e^-_{(g)}} \rightleftharpoons \mathrm{H_{2(g)}}$), which has a value of 4.44 V with respect to the vacuum level, is set to zero[9,10].

A metal is a very good conductor, so the excess charge is restricted to a small surface region of about 1 Å. Usually electrolytes are used in concentrations between 0.1 – 1 M. Although they are good conductors too, their conductivity is orders of magnitudes smaller than that of metals. So the lower charge carrier concentration causes the charge to extend over a larger region of space, which has a length of typically 5 – 20 Å. The resulting charge distribution is the so called electric double layer and consists of two different sized regions of equal, but opposite charges. It acts as a capacitor with a small plate separation and has therefore a very high capacitance[8]. The most accurate description of a double layer is made by Stern. In his model two double layer regions exist, one compact layer next to the metal electrode followed by a diffusive one[9].

An electrochemical cell is usually operated in a three-electrode configuration, consisting of a working (WE), a reference (RE), and a counter electrode (CE). The working electrode is the investigated one. RE is needed to determine the potential of WE and since no current should flow between these two electrodes, a counter electrode is needed, which takes up the current [8]. In practice electrodes of the second type (silver-silver chloride or saturated calomel electrode) are used. They are connected via a salt bridge to the electrochemical cell [9].

2.2 Cyclic Voltammetry (CV)

Cyclic voltammetry is the first choice if one is faced with an unknown electrochemical system. The measurement setup consists of a three-electrode configuration connected to a potentiostat. With a constant rate, the working electrode potential is varied cyclically between two turning points. The resulting current is measured. In Fig. 1, the sawtooth-like potential shape over time is shown. The potential range is mostly chosen to be between the oxygen and the hydrogen evolution regime. By plotting the current as a function of the applied potential, processes occurring in the potential range can be studied [8,9].

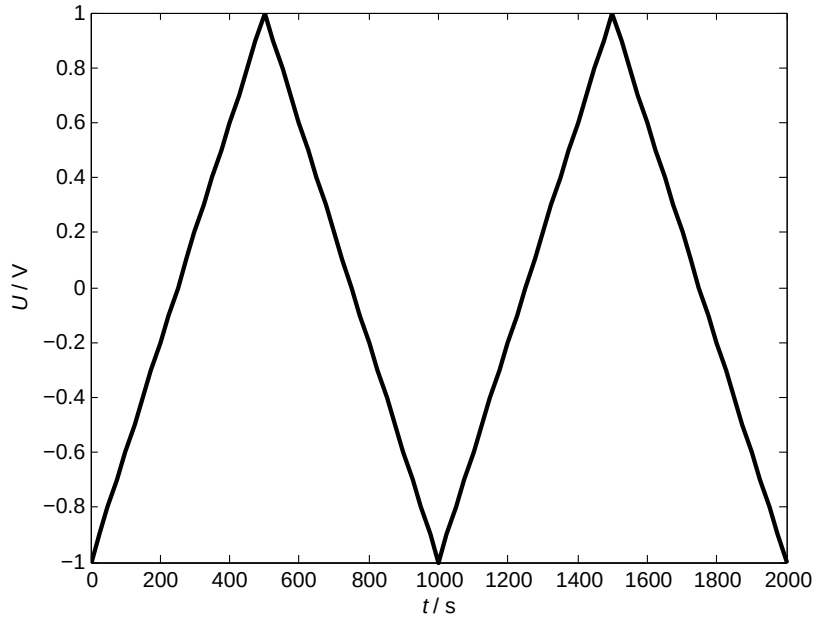

Figure 1: Sawtooth-like shape of electrode potential over time applied in cyclic voltammetry.

If there are no additional substances in the electrolyte, which are electrochemical active in the applied potential range, the current peaks are due to hydrogen and oxygen chemisorption. In such cyclic voltammograms one can distinguish between a hydrogen, a double layer and an oxygen region[9]. The shape of the measured CV is strongly depended on the used electrolyte. Exemplary, in Fig. 2a and 2b, CVs of nanoporous gold and palladium are shown in 0.01 M $HClO_4$.

The hydrogen evolution reaction for npAu is kinetically hindered, so that the cyclic voltammogram does not show a hydrogen adsorption region. Only at very negative potentials a measurable rate is detectable[8]. Nanoporous gold has therefore a very large double layer region, which ranges from −200 mV to 800 mV in Fig. 2a. The peak at about 500 mV is unexpected and should not exist in comparison with literature. At higher potentials in the anodic part, oxygen adsorption starts with a significant peak at about 900 mV. In the cathodic part, upon decreasing the potential, the oxygen gets desorbed again. This desorption peak starts at about 1000 mV and ends at 600 mV.

In contrast, the cyclic voltammogram of nanoporous palladium, as shown in Fig. 2b, has a strong hydrogen region. Palladium can not only adsorb, but also absorb hydrogen. The first peak in the cathodic range of the CV, slightly below −100 mV, marks the hydrogen adsorption ($H^+ + Pd + e^- \rightleftharpoons PdH_{ads}$). At lower potentials, the absorption into the sub-layers of palladium ($PdH_{ads} + Pd_{surface} \rightleftharpoons Pd_{surface} + PdH_{abs(subsurface)}$) occurs and finally at very low potentials the hydrogen evolution reaction starts[4,5]. Between about 0 and 600 mV the double region is located. At higher potentials, the oxygen adsorption in the anodic range and the reduction of oxygen in the cathodic range occurs.

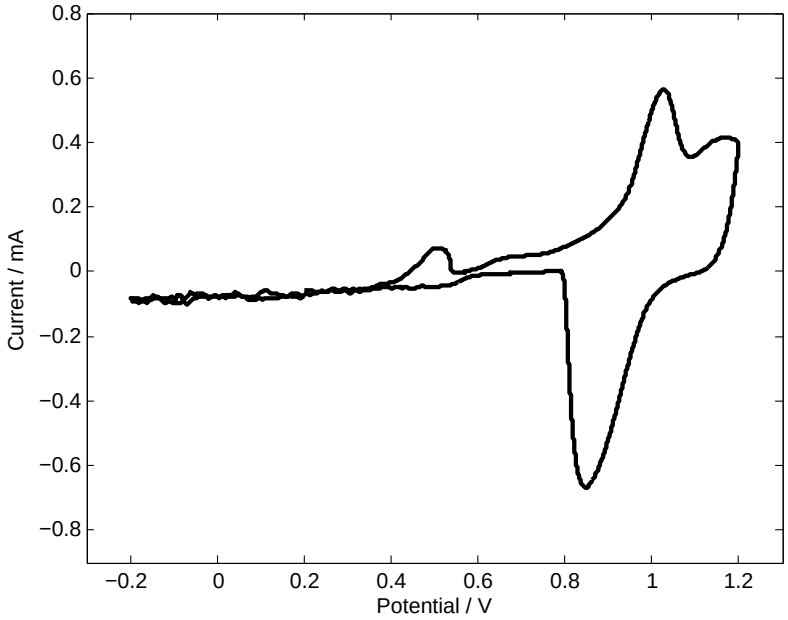

(a) CV of npAu

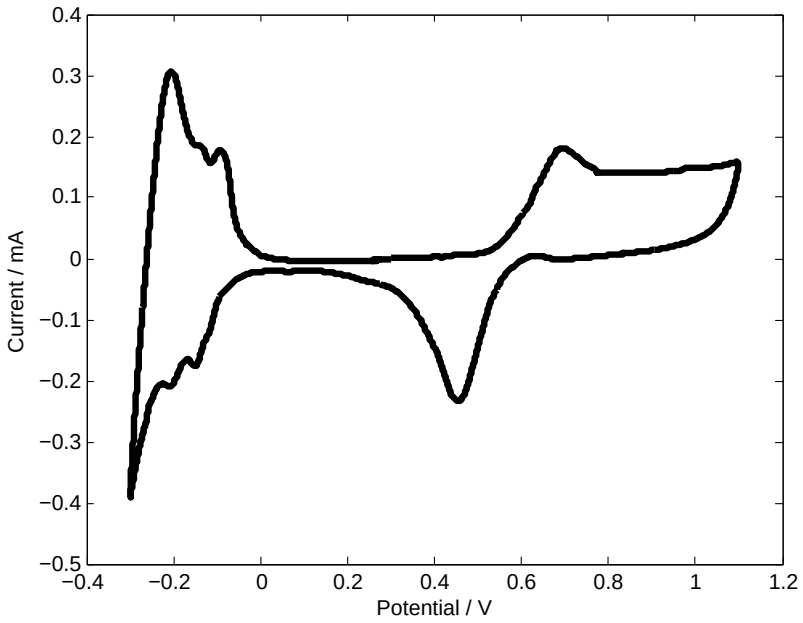

(b) CV of npPd

Figure 2: Cyclic voltammograms of npAu (a) and npPd (b) measured in 10 mM $HClO_4$ with a scan rate of 0.1 mVs^{-1}.

2.3 Dealloying

Dealloying is the selective dissolution of one or more components of an alloy. This process is used to fabricate nanoporous metals for a variety of applications (catalysis, sensing, actuation, supercapacitors, etc.). The electrochemical dealloying process starts at a composition-dependent critical potential V_c. By applying a constant potential below this value, a full-coverage layer of the more noble component forms and results in a passivation of the alloy surface[11]. Above V_c, atoms can easily be removed from low-coordination sites such as step edges. Since these surface sites are rapidly passivated by the remaining more noble species, the rate-limiting step of the nanoporosity evolution is the dissolution of atoms from high-coordination sites (Fig. 3a). The remaining noble atoms diffuse from low concentration areas to high concentration areas (Fig. 3b). In that way thermodynamically unfavorable adatoms are prevented. Because of this surface rearrangement and the resulting formation of noble metal clusters, new dissolvable atoms are exposed to the electrolyte and the dealloying process continuous (Fig. 3c). If not enough noble atoms are provided to passivate the formed mounds, they get undercut, which results in bifurcates pores. Such a process increases the surface area dramatically, allowing porosity evolution to proceed into the bulk of the alloy. Beside the critical potential, the parting limit, which is the fraction of the dissolving species, below which dealloying does not proceed, plays an important role[3].

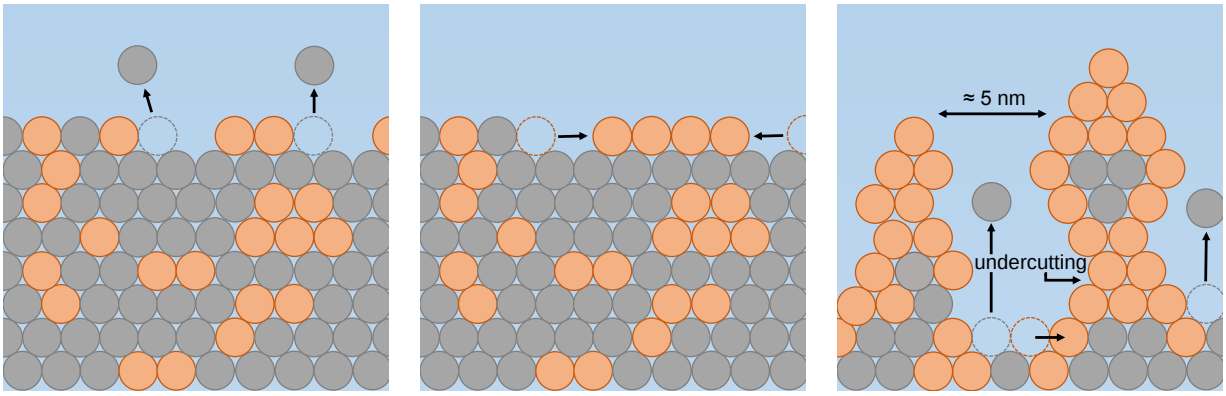

(a) Formation of terrace vacancies

(b) Surface diffusion

(c) Continuing dealloying, formation of undercutting

Figure 3: Dealloying process of an alloy A_xB_{1-x}.

A characteristic measure of a nanoporous structure is the average ligament diameter. This quantity depends on the temperature during dealloying, the dealloying rate and the alloy composition. Furthermore the melting point T_{m} of the nanoporous metal affects the final ligament size, the higher T_{m}, the smaller are the ligaments. Therefore, for nanoporous gold a larger ligament size is suggested than for nanoporous palladium [11].

Since nanoporous metals have a very large surface area, they are always thermodynamically metastable. Beside the coarsening process at ambient temperatures, a controlled growth of the ligaments at elevated temperatures is used to get the desired ligament/pore sizes [3].

2.4 Electrochemical Impedance Spectroscopy (EIS)

This chapter is related strongly on the book of Orazem and Tribollet [12], *Electrochemical Impedance Spectroscopy*, chapter *A Brief Introduction to Impedance Spectroscopy*. All theoretical aspects are based on this book.

The main benefit of impedance spectroscopy, in contrast to steady state measurements, is the expansion of information that can be extracted from the measurements. This arises from the frequency dependence of the macroscopic measurements.

To explain the theory of impedance spectroscopy in the simplest way, a sinusoidal input signal is applied on the sample and the output signal is measured. The relation between the input and the output for a linear-time-invariant system is called a transfer function. It characterizes the frequency response of the system. Impedance spectroscopy is therefore a special case of a transfer function.

The mathematical expression for such a sinusoidal input is given by the following equation:

$$X(t) = \bar{X} + |\Delta X| \cos(\omega t), \tag{2}$$

where $\bar{X}$ is the steady state or time invariant part of the signal and $|\Delta X|$ represents the magnitude of the oscillating part of the signal. If $|\Delta X|$ is small, the response is linear and the output will have the same form as the input signal at the same frequency with an additional phase lag between the input and the output *Y(t)*:

$$Y(t) = \bar{Y} + |\Delta Y| \cos(\omega t + \phi). \tag{3}$$

The transfer function itself is independent of time and of the input signal magnitude. It depends only on the frequency. The magnitude of a transfer function at a given frequency is defined as the ratio of the amplitudes of the output $|\tilde{Y}(\omega)|$ and the input signal $|\tilde{X}(\omega)|$:

$$|H(\omega)| = \frac{|\tilde{Y}(\omega)|}{|\tilde{X}(\omega)|}. \tag{4}$$

The phase shift can be calculated via:

$$\phi(\omega) = 2\pi\frac{\Delta t}{T}, \tag{5}$$

where Δt is the time lag between the two signals and T is the period of the signals. In most cases, the input signal $\tilde{X}(\omega)$ is real and the output signal $\tilde{Y}(\omega)$ is a complex number, with magnitude $|\tilde{Y}(\omega)|$ and phase $\phi(\omega)$. So the transfer function attains the following form:

$$|H(\omega)| = \frac{\tilde{Y}(\omega)}{\tilde{X}(\omega)} = \frac{|\tilde{Y}(\omega)|}{|\tilde{X}(\omega)|}(\cos\phi(\omega) + i\sin\phi(\omega)). \tag{6}$$

For an electrochemical system, the input signal is a potential and the output signal is a current. The transfer function is therefore called admittance, the inverse of the impedance. Although the admittance is measured, the impedance in dependence of the frequency is considered, i.e.,

$$Z(\omega) = \frac{\tilde{V}(\omega)}{\tilde{i}(\omega)}. \tag{7}$$

For potentiostatic impedance measurements, as performed in this thesis, an oscillatory potential $V = \bar{V} + |\Delta V|\cos(\omega t)$ is applied. This yields a current $I = \bar{I} + |\Delta I|\cos(\omega t + \phi)$ and an impedance as shown in Eq. (7).

Impedance data can be represented in complex-impedance-planes, also called Nyquist plots, as shown in Fig. 4. On the x-axis the real part $\mathrm{Re}(Z)$ and on the y-axis the negative imaginary part -$\mathrm{Im}(Z)$ is plotted. Each data point corresponds to a different measurement frequency. Such a representation of the measured data is very popular because the shape of the locus of points yields insight into possible mechanisms or governing phenomena. In this thesis most analysis is based on Nyquist plots, because, e.g., the pore geometry can be estimated out of it. The disadvantage of such a plot is that the frequency dependence is obscured. Furthermore, the measured data can be shown in a Bode representation, where the total impedance $|Z|$ (Fig. 5a) or the phase angle (Fig. 5b) is plotted in dependence of the frequency.

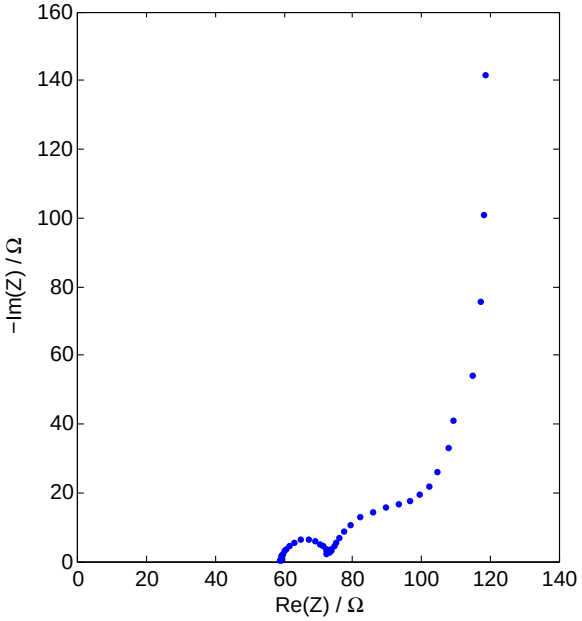

Figure 4: Nyquist plot of measured impedance data of a nanoporous gold electrode.

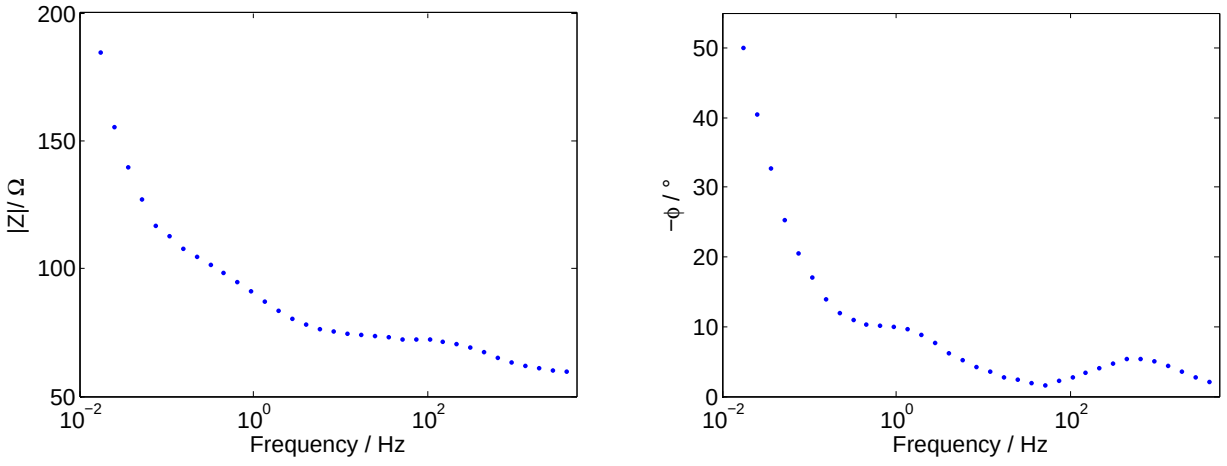

(a) Bode plot **(b)** Bode phase

Figure 5: Measured total impedance and phase angle of a nanoporous gold electrode in dependence of the frequency.

2.4.1 Fitting of Impedance Spectra

Fitting of impedance spectra to equivalent circuits is a first step in analysis. Since it is difficult to find circuits that are simply related to the underlying mechanism, the interpretation of certain elements is not so easy[13].

The simplest equivalent circuit is shown in Fig. 6. It consists of the solution resistance R_s (often called electrolyte resistance R_e) and a capacitance C_dl being parallel to a charge transfer resistance R_ct. Such a circuit describes for example a simple redox reaction at the interface between a metal and a solution[13]:

$$\mathrm{A_{aq}} \rightleftharpoons \mathrm{A_{aq}^+} + \mathrm{e^-}. \tag{8}$$

The mass transport of reactant A and product $\mathrm{A^+}$ maintains constant concentrations at the interface. No adsorption occurs at the metal-solution interface. Point X in Fig. 6 corresponds to the potential on the metal side, point Y to the potential at the electrolyte side. The potential difference between X and Y drives the reaction, which is modeled by R_ct. Point Z gives the potential at the reference electrode. In general, C_dl characterizes the interface, R_ct the reaction, and R_s the solution. The total impedance of this system is given by[13]:

$$Z = R_\mathrm{s} + \frac{R_\mathrm{ct}}{1 + i\omega C_\mathrm{dl} R_\mathrm{ct}}. \tag{9}$$

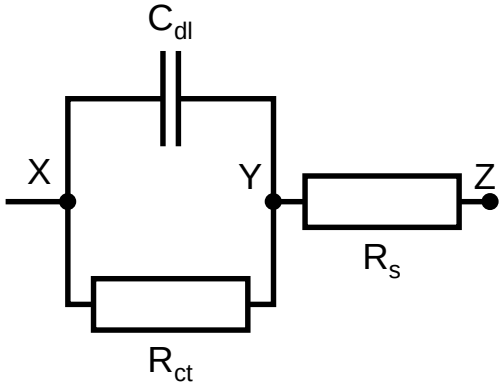

Figure 6: Equivalent circuit of a redox reaction at metal-solution interface.

In Fig. 7a, an impedance spectrum consisting of three semicircles is shown. Therefore three capacitors and three resistances are needed in the equivalent circuit, which is shown in Fig. 7c. The solution resistance is set to zero in this Nyquist plot. Each RC element fits one semicircle. Their diameters are R_a, R_b and R_c. The corresponding double layer capacitance is $C_\mathrm{dl}^{-1} = C_\mathrm{a}^{-1} + C_\mathrm{b}^{-1} + C_\mathrm{c}^{-1}$. A disadvantage of such an equivalent circuit is that its impedance is insensitive to exchanges of, e.g., the $R_\mathrm{a}C_\mathrm{a}$ element and the $R_\mathrm{b}C_\mathrm{b}$ element. This can cause the fitting routine to have some convergence difficulties. The circuit shown in 7b, is equivalent to the other circuit, but the RC elements do not correspond to a certain semicircle any more. In such a ladder circuit, the elements can not be exchanged as described above, because the values of the resistances or capacities depend on the position in the circuit. Although these two circuits (Fig. 7b and 7c) are equivalent, in practice they differ in their application [13].

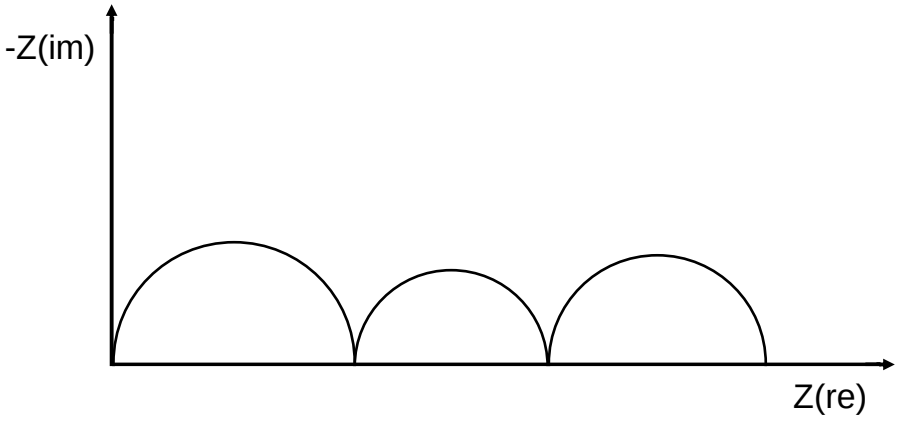

(a) Impedance spectrum consisting of three semicircles.

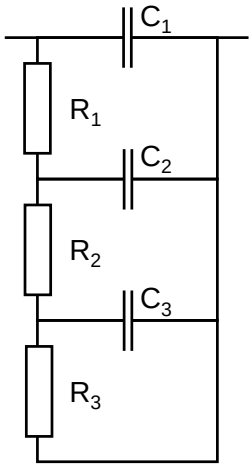

(b) Equivalent circuit, RC elements ordered in a transmission line.

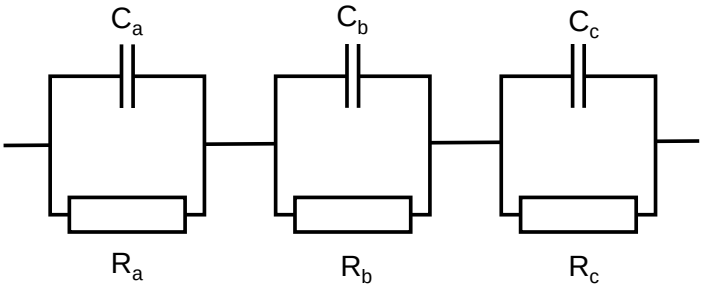

(c) Equivalent circuit, RC elements in series connection.

Figure 7: Impedance spectrum and equivalent circuits used for the fit.

By fitting impedance spectra, instead of a capacitance often a constant phase element (CPE) is used. This very general element is used to model imperfect capacitors with phase shifts deviating from 90°. A CPE improves the fit by the assumption that a distribution of time constants is present in the investigated system. The equivalent circuit of Fig. 6, can also be expressed via a constant phase element (Fig. 8). The total impedance of such a circuit is given by[12]:

$$Z = R_{\mathrm{s}} + \frac{R_{\mathrm{ct}}}{1 + (i\omega)^{\alpha} Q R_{\mathrm{ct}}}. \tag{10}$$

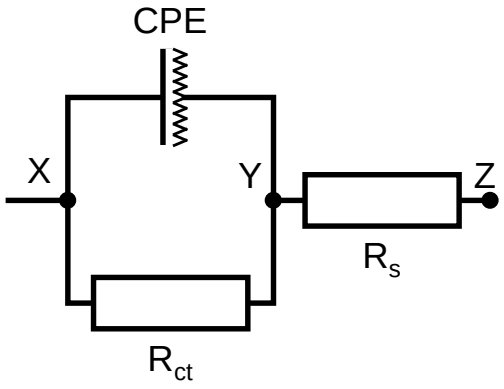

Figure 8: Equivalent circuit of a redox reaction at metal-solution interface. The capacitance is replaced by a constant phase element (CPE).

By comparing these two equations, the only difference is that $i\omega C_{\mathrm{dl}}$ is replaced by $(i\omega)^{\alpha} Q$. The parameter α describes the deviation from the vertical behavior of a pure capacitance in the Nyquist plot presentation and can be associated with the slope of a certain part of the spectrum. If $\alpha = 1$, the system is described only by one single time constant, and the parameter Q is equal to the capacitance C_{dl}. If $\alpha < 1$, the system has a certain surface heterogeneity or continuously distributed time constants for charge transfer reactions. In such a case the CPE parameter Q cannot represent a capacitance. The corresponding capacitance value of the CPE, in that case is given by[12,14]:

$$C_{\mathrm{dl}} = Q^{1/\alpha} R_{\mathrm{ct}}^{(1-\alpha)/\alpha}. \tag{11}$$

2.4.2 Porous Electrodes in Electrolyte Solution

The theory of porous electrodes and the calculation of their impedance has been developed during the last few decades. In the 1960s, de Levie published his elegant work in this field of research, which becomes something like the basic of all other theories[7]. The model of de Levie makes several assumptions. For example, the pores in his calculation are cylindrical with uniform cross-section, and exhibit semi-infinite length with no cross-links. They are homogeneously filled with electrolyte and a large amount of it is inert. The electrode material has no resistance and the curvature of the equipotential surfaces within the pores may be neglected[15].

In his model, each pore may be represented by a transmission line (Fig. 9) consisting of the electrolyte resistance for pores of unit length, also called the pore resistance, R (units of Ωcm^{-1}) and the interfacial impedance Z for pores of unit length (units of Ωcm)[12,15]. The bulk electrolyte resistance outside the pore is labeled as R_e. R and Z are constant over the whole transmission line. The interfacial impedance Z consists in the general case of a capacitance and a charge transfer resistance part. In literature such a configuration is often called the non-blocking condition, where faradaic reactions between the electrode and the electrolyte are possible. If Z consists only of a capacitance, the electrode is in the so called blocking condition, where no faradaic reactions and therefore no charge transfer between the electrode and electrolyte are allowed[16,17]. In the following, special care will be taken on the analysis of electrodes in blocking condition. The pore resistance R and the interfacial impedance Z can therefore be expressed in function of the pore radius:

$$R = \frac{\rho}{\pi r^2}, \tag{12}$$

$$Z = \frac{Z_{eq}}{2\pi r}. \tag{13}$$

In these equations, ρ is the electrolyte resistivity and Z_eq is the interfacial impedance[1][12]. The impedance Z depends on the potential, if slow electrode reactions exist, and on time, if the reaction is diffusion controlled[15].

[1] $[Z_\text{eq}] = \Omega\text{cm}^2$, (capacitance per unit area C: $[C] = \frac{\text{F}}{\text{cm}^2}$; interfacial impedance $Z_\text{eq} = \frac{1}{i\omega C}$, $[Z_\text{eq}] = \frac{\text{scm}^2}{\text{F}} = \Omega\text{cm}^2$)

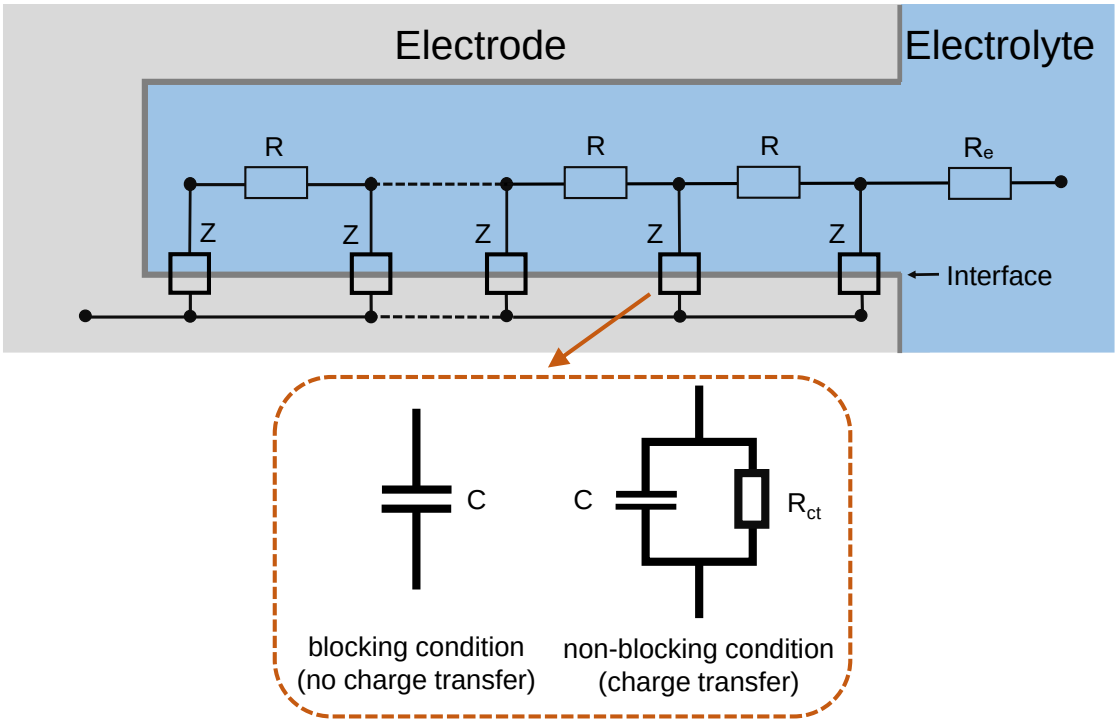

Figure 9: Representation of a pore via a transmission line in blocking and non blocking condition.

The impedance Z depends for small amplitudes ($<< 5mV$) only on the angular frequency ω. By applying only small amplitudes and considering only steady state harmonic response, Z can be easily calculated. As shown in Fig. 10, the equivalent circuit is divided into an infinitesimally small section dz[15].

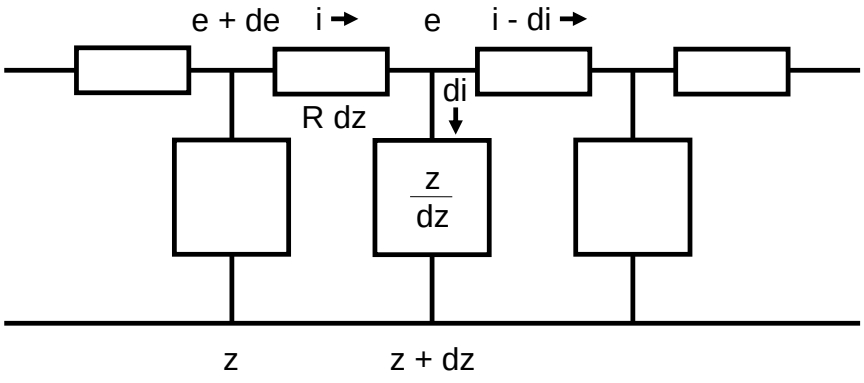

Figure 10: Equivalent circuit divided into an infinitesimally small section dz. Here, e corresponds to the potential, de to the infinitesimally small potential change, i to the current and di to the infinitesimally small current change.

This circuit can mathematically be described by[15]:

$$de = -iRdz,$$

$$\frac{de}{dz} + iR = 0, \tag{14}$$

$$di = -\frac{e}{Z}dz,$$

$$\frac{di}{dz} + \frac{e}{Z} = 0. \tag{15}$$

The quantities e and i are described in Fig. 10. Eq. (14) and (15) can be combined to[15]:

$$\frac{d^2i}{dz^2} - \frac{R}{Z}i = 0, \tag{16}$$

$$\frac{d^2e}{dz^2} - \frac{R}{Z}e = 0. \tag{17}$$

For shallow pores of depth l, the boundary conditions for solving Eq. (17) are[15]:

$$e(0) = E \tag{18}$$

$$\left(\frac{de}{dz}\right)_{z=l} = 0 \tag{19}$$

de Levie solved this differential equation and specified the pore impedance as[12,15]:

$$Z_{\text{pore}} = \sqrt{RZ}\coth\left(l\sqrt{\frac{R}{Z}}\right). \tag{20}$$

With n as the number of pores in the electrode, the total impedance of a porous electrode can then be expressed as following[12]:

$$Z_{\text{tot}} = R_{\text{e}} + \frac{Z_{\text{pore}}}{n}. \tag{21}$$

The quantity $\sqrt{\frac{Z}{R}}$ is defined as the penetration depth λ. So the impedance of the pore can be expressed as[7]:

$$Z_{\text{pore}} = \sqrt{RZ}\coth\left(\frac{l}{\lambda}\right). \tag{22}$$

The penetration depth λ depends on the frequency of the applied ac wave[7]. The penetration depth for a pure capacitive effect ($Z = \frac{1}{i\omega C}$) is proportional to $\lambda \propto \sqrt{\frac{1}{\omega}}$ and therefore $\frac{l}{\lambda} \propto \sqrt{\omega}$[18]. At high frequencies the penetration depth is very small ($l >> \lambda$) and $\frac{l}{\lambda}$ very high, and therefore $\coth\left(\frac{l}{\lambda}\right)$ tends towards unity[7]. In this case the pore appears to be semi-infinite and $Z_{\text{pore}} = \sqrt{RZ}$[7,12]. This impedance for a semi-infinite pore can also be obtained by solving Eq. (17) with the boundary condition $e(\infty) = 0$ instead of Eq. (19)[15]. In the representation of the impedance in a Nyquist plot, as shown in Fig. 11, the loci of the impedance have a phase angle of 45° in the high frequency region. As the frequency is lowered, the penetration depth increases ($\lambda >> l$) and the fraction $\frac{l}{\lambda}$ gets very small. $\coth\left(\frac{l}{\lambda}\right)$ and therefore Z_{pore} tends towards infinity. Therefore, in the low frequency region the electrode surface appears to be quasi-planar and the impedance loci take on the form that is characteristic for a capacitor, which corresponds to a phase angle of 90°[7]. This is also demonstrated in Fig. 11.

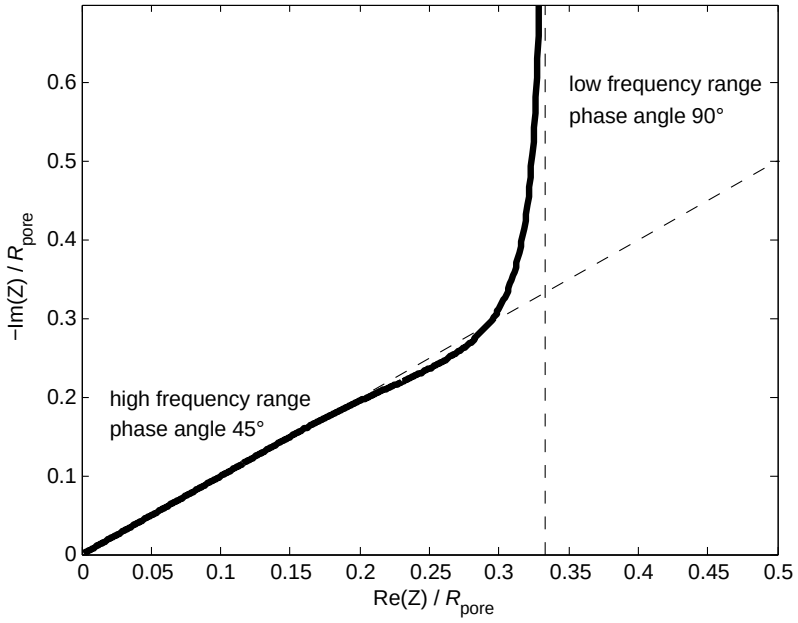

Figure 11: Shape of the Nyquist plot of a cylindrical pore with pure capacitive behavior according to the assumption of de Levie. The impedance is plotted with respect to R_{pore}, the total pore resistance of the cylindrical pore, which is the sum over all resistance values R.

Keiser extended the transmission line model and calculated the impedance of a porous electrode for non-cylindrical pore shapes. The transmission line in his work consists of an electrolyte resistance within the pore and a double layer capacitance as electrode impedance. Therefore de Levie transmission line matches that one of Keiser by considering only a pure capacitance effect at the electrode interface. The pore radius a in Keiser's work is allowed to change in dependence of unit length. With that assumption, he was able to calculate the impedance of pore with different pore shapes. The electrolyte resistance per unit length $R(x)$ and the

double layer capacitance per unit length $C(x)$ are analog to Eq. (12) and (13), but with values depending on the position within the pore. They are given by[19]:

$$R(x)dx = \frac{\rho}{\pi a^2(x)}dx, \tag{23}$$

$$C(x)dx = 2\pi C_{\mathrm{dl}} a(x)dx, \tag{24}$$

where C_{dl} is the specific double layer capacitance. The equations in Keisers model (Eq. 23 and 24) are written with respect to a cylindrical pore with length l and radius r and are therefore dimensionless. By doing this normalization, a so-called shape factor $f(\xi)$ arises. This factor is the ratio of pore radius $a(\xi)$ at position $\xi = \frac{x}{l}$ and the pore radius r of the corresponding cylindrical pore ($f(\xi) = \frac{a(\xi)}{r}$). For cylindrical pores, the pore radius is the same over the whole pore and so the shape factor $f(\xi)$ is equal to one. In that case the impedance can be calculated analytically[19]. It matches the solution of the model of de Levie (Z_{pore} in Eq. (20) and (22), impedance of the electrode (21), Nyquist plot in Fig. 11). For all other pore shapes, the shape factor is unequal one. In that cases the solution of the impedance has to be solved using a recursion formula. For different pore shapes, Keiser calculated the loci of the impedance, which are shown in Fig. 12. As one can see, for a conical shaped pore (number 5) the locus is much more steeper than for cylindrical pores. For pores with a more convex form (numbers 2, 3, 4), the locus tends towards the real axis of the Nyquist plot as the pore radius gets wider and tends towards infinity as the radius decreases.

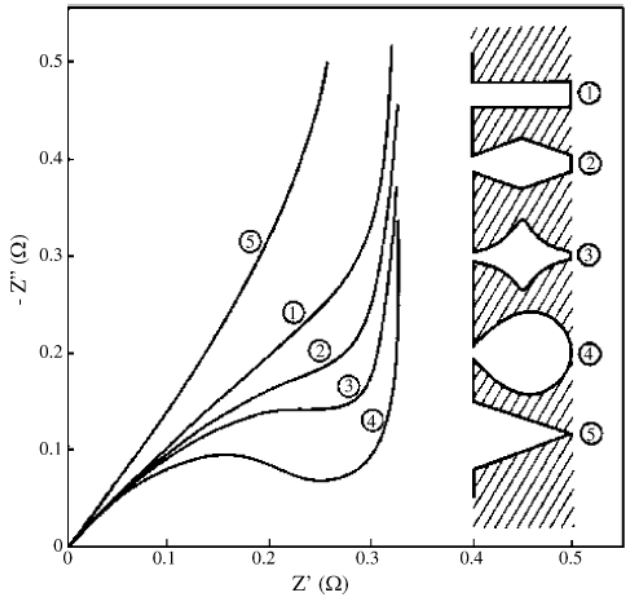

Figure 12: Loci of the impedance for different pore shapes calculated of Keiser. The impedance is plotted with respect to the electrolyte resistance of the cylindrical pore. Image reprinted from Macdonald[7].

If the pore shape and the shape factor $f(\xi)$ are known, the pore radius r and the pore length l for the cylindrical equivalent pores can be calculated. The required equations are[19]:

$$\lim_{\omega \to 0} Re(Z_{\text{tot}}) = \frac{R_{\text{pore}}}{3n} = \frac{l\rho}{3n\pi r^2} = R_{\Omega}, \tag{25}$$

$$V_{\text{pore}} = n\pi r^2 l \int_0^1 f^2(\xi) d\xi, \tag{26}$$

$$C_{\text{tot}} = nC_{\text{dl}} 2\pi r l. \tag{27}$$

From these equations the radius and the length of the pore can be calculated[19]:

$$r = \frac{2V_{\text{pore}}}{A \int_0^1 f^2(\xi) d\xi}, \tag{28}$$

$$l = \sqrt{\frac{3V_{\text{tot}} R_{\Omega}}{\rho \int_0^1 f^2(\xi) d\xi}}. \tag{29}$$

In Eq. (28):

$$A = \frac{C_{\text{tot}}}{C_{\text{dl}}}, \tag{30}$$

is the surface of the porous sample. Eq. (25) is the mathematical proof of the impedance loci behavior of Fig. 12. By decreasing the frequency, all pore shapes have the same limiting factor for the real part of the impedance. For one single pore this limiting factor is equal to $\lim_{\omega \to 0} Re(Z_{\text{pore}}) = \frac{R_{\text{pore}}}{3}$. Fig. 11 and 12 are plotted with respect to R_{pore} and so the limiting factor is $\frac{1}{3}$, which can be clearly seen[19]. The pore resistance and the total capacitance can also be calculated via the truncated transmission line:

$$R_{\text{pore}} = \sum_i^N R_{\text{i}}, \tag{31}$$

$$C_{\text{tot}} = \sum_i^{N+1} C_{\text{i}}, \tag{32}$$

where N is the number of used resistances[16]. Since the shape factor $f(\xi)$ cannot be determined experimentally, in measurements the corresponding cylindrical pore radius and length are calculated. For this purpose $f(\xi) = 1$ and the equation for radius and length simplify to[20]:

$$r = \frac{2V_{\text{pore}}}{A}, \tag{33}$$

$$l = \sqrt{\frac{3V_{\text{pore}}R_{\Omega}}{\rho}}. \tag{34}$$

Furthermore the number of pores can be calculated[20]:

$$n = \frac{A}{2\pi r l}. \tag{35}$$

To be able to compare the total capacitance of different electrodes of the same material, the specific surface area α, the surface area A per mass m, is very useful[21]:

$$\alpha = \frac{A}{m}. \tag{36}$$

In the matrix calculation method for the determination of the pore impedance for arbitrary pore shapes, Eloot comes to the point that the limiting factor of the real part is not $\frac{1}{3}$, but instead converges to a geometry constant Λ_{g}. Λ_{g} depends on the pore geometry and is equal to $\frac{1}{3}$ for cylindrical pores (Fig. 13, pore shape *d*). For pores with a narrowing cross section $\Lambda_{\text{g}} < \frac{1}{3}$ (Fig. 13, pore shapes *a* and *b*) and for pores with broadening cross section $\Lambda_{\text{g}} > \frac{1}{3}$ (Fig. 13, pore shapes *c* and *e*). The limit of the imaginary part is independent of the pore shape and can be written as $\frac{Z}{2\pi r l}$. By assuming only capacitive effects at the electrode interface, the impedance reads $Z = \frac{1}{i\omega C_{\text{tot}}}$. Therefore in the limiting low frequency case, the pore impedance has the form[22]:

$$Z_{\text{pore}} = \Lambda_{\text{g}} R_{\text{pore}} + \frac{Z}{2\pi r l}. \tag{37}$$

As one can see in Fig. 13, additional to the different geometry constant, the phase angle becomes smaller than 45° for a pore which narrows at the pore mouth and becomes larger than 45° for a pore which broadens at the pore mouth.

The equivalent circuit used by Eloot is more complex and shown in Fig. 14. Additional to the electrolyte resistance R_{e}, the electrolyte resistance within the pore R_{s} (identical to the pore resistance in the previous models) and the interface impedance Z, the impedance Z_{m} of the material around the pore, the impedance of the electrode surface at the pore mouth Z_{I}, the pore base impedance Z_{U} and the material layer impedance Z_{b} are considered. All quantities except of R_{e} and Z_{b} depend on the position coordinate x of the pore and are used in the calculation of the total pore impedance Z_{pore}. i_{m} and i_{s} describes the currents flowing into the electrode material and the electrolyte, respectively[22].

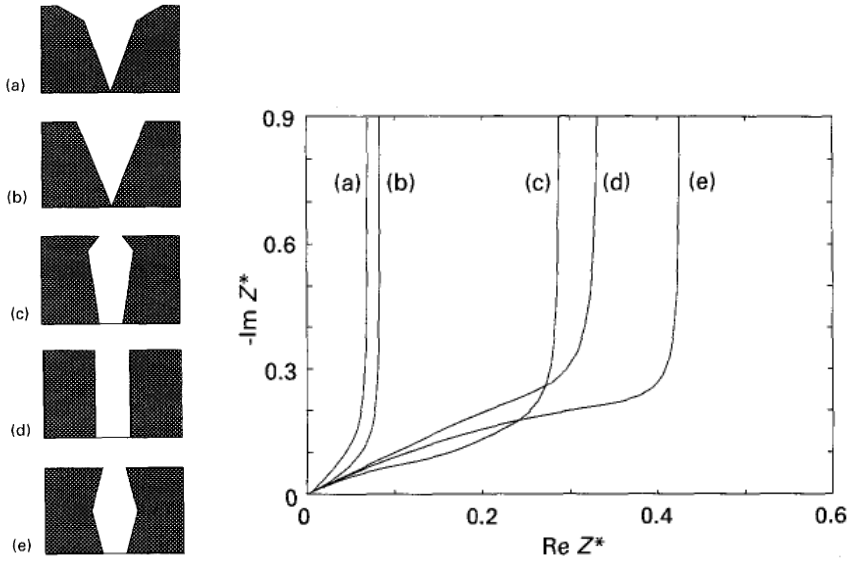

(a) Different pore shapes

(b) Nyquist plots belonging to the different pore shapes

Figure 13: Comparison of the normalized pore impedances of different pore shapes, images reprinted from Eloot et al. [22].

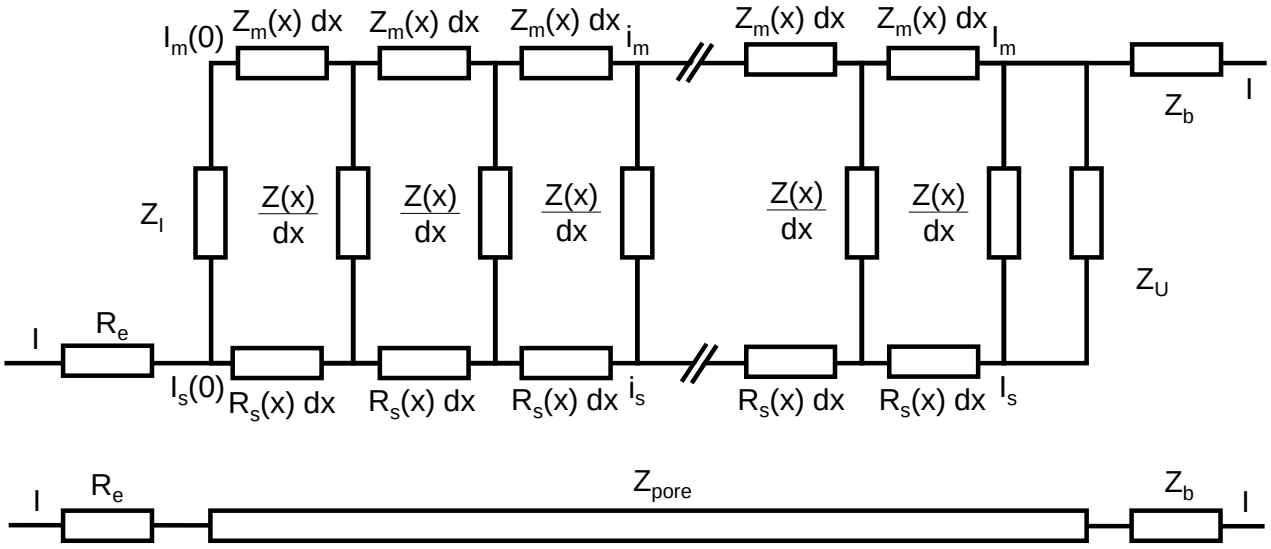

Figure 14: Equivalent circuit used by Eloot.

3 Experimental

3.1 Alloy Production

An silver-gold and a cobalt-palladium alloy with a stoichiometric ratio of 75% silver and cobalt and 25% gold and palladium, respectively, was used. The starting materials have been a silver wire (ChemPur, 99.9%, 0.5 mm diameter), gold granules (ChemPur, 99.99%), cobalt slug (AlfaAeser, 99.95%), and palladium granules (AlfaAeser, 99.95%). After weighting the materials in the correct ratios, as listed in Table 1, they are melted together by an arc melter MAM 1 (Edmund Bühler GmbH). To achieve perfect mixing of the components, the melting process was repeated several times. After the melting process, the alloys have a spherical like shape. Therefore they are rolled to the desired thickness. To avoid cracks and fractures, the thickness decrease of the specimen per rolling step is only allowed to be half the initial thickness and an annealing step has to be made afterwards. The annealing was made in a furnace under vacuum conditions for 1 h at 650°C for $Ag_{75}Au_{25}$ and 1 h at 750°C for $Co_{75}Pd_{25}$. After several rolling and annealing steps the final thicknesses of 170±10 μm for the silver-gold and 250±10 μm for the cobalt-palladium alloy are obtained. To guarantee homogeneity of the produced alloys, XRD measurements have been made. It should be noted that during the formation of $CO_{75}Pd_{25}$ alloy, the tip of the arc melter was in contact with the sample. During the resulting circuit, copper could be incorporated into the alloy.

Table 1: Stoichiometric ratio ST of the alloy AB and masses of the different starting materials. m_A is the mass of component A, m_B the mass of component B and m_{tot} the mass of component A and B.

alloy AB	***ST*** **/ at%**	***ST*** **/ wt%**	m_A **/ mg**	m_B **/ mg**	m_{tot} **/ mg**
AgAu	75.0 : 25.0	62.2 : 37.8	1257.49	770.73	2028.21
CoPd	75.0 : 25.0	62.4 : 37.6	1302.32	786.44	2089.23

3.2 Electrochemistry

All electrochemical measurements have been done with an Autolab PGSTAT128N, operated via the NOVA software. As reference electrode served an Ag/AgCl electrode of Methrom, filled with saturated KCl as reference electrolyte. For the dealloying of $Ag_{75}Au_{25}$ and further measurements with nanoporous gold, occasionally an Ag/AgCl electrode with an additional salt bridge (KNO_3) was used. The Ag/AgCl reference electrode has a standard electrode potential of +197 mV versus the standard hydrogen electrode (SHE). As electrolytes served 1 M $HClO_4$ (Fluka Analytical, 1N), 0.01 M $HClO_4$, 1 M H_2SO_4 (Roth, 2N) and 0.1 M H_2SO_4. The electrolytes with lower concentration are prepared by diluting the corresponding 1 molar with distilled water (Roth).

The used samples have been cut out of the rolled thin alloy stripes. Two different sample types are used. Some samples are connected via a wire to the measurement instrument. The sample area was then chosen to be either 3×5 mm^2 or 5×6 mm^2, respectively. Depending on the alloy, a gold or palladium wire was used. To ensure a proper connection of the wire with the alloy, the wire is pressed on the sample. Other samples are connected directly with the potentiostat. The sample area is therefore chosen to be about 5×20 mm^2.

3.2.1 Dealloying

For the electrochemical dealloying of $Ag_{75}Au_{25}$, either 1 M $HClO_4$ or 1 M H_2SO_4, was used as electrolyte. The alloy was used as working electrodes, a curled platin wire served as counter electrode for both electrolytes. For dealloying, a constant working potential of 1.15 V was applied for both $HClO_4$ and H_2SO_4. If the current flow had reached a certain residual value, 500 μA for $Ag_{75}Au_{25}$, the dealloying process was stopped.

The $Co_{75}Pd_{25}$ alloy was dealloyed in 0.1 M H_2SO_4. Again the alloy was placed as working electrode. A curled palladium wire served as counter electrode. A constant working potential of 0.55 V was applied during the dealloying process. The stopping condition is 100 μA.

Samples directly connected (without a wire) to the measurement instrument are dealloyed in the same way as described above. They are only immersed few millimeter into the electrolyte. Therefore the predominant part of the alloy is not in contact with the electrolyte. The resulting nanoporous structure is then a part of the remaining alloy.

To remove the remaining electrolyte in the pores of the deallyoed samples, they have been immersed into distilled water four several hours. After drying, the samples are ready for further investigaitons.

3.2.2 Electrochemical Measurements (CV and EIS)

For **cyclic voltammetry measurements** 0.01 M $HClO_4$ was used as electrolyte. The dealloyed samples served as working electrodes. Since too high current densities at the counter electrode must be avoided, a counter electrode with a high surface area is needed. Therefore a porous carbon fabric connected via a platinum wire or a curled platinum wire with a surface area of about 5 cm^2 have been used.

The setup for **electrochemical impedance spectroscopy measurements** differs not quite much from that of CV measurements. Electrolyte and working electrode stayed the same. To prevent inductive artefacts, as counter electrode the curled platinum wire was chosen. Subsequent studies with nanoporous palladium suggest that also a porous carbon fabric connected via a platinum wire can be used. The main modification compared to the CV setup is the parallel connection of the reference electrode with a 1 μF capacitance in series with a platinum wire, as recommended from the producer of the reference electrode. This capaci-

tance is needed to reduce the reference electrode impedance in the high frequency domain[23]. Therefore the three electrode configuration used in CV measurements changes to a quasi four electrode configuration because of the parallel connection. The schematic representation of the electrochemical cell setup with the electrode configuration is shown in Fig. 15.

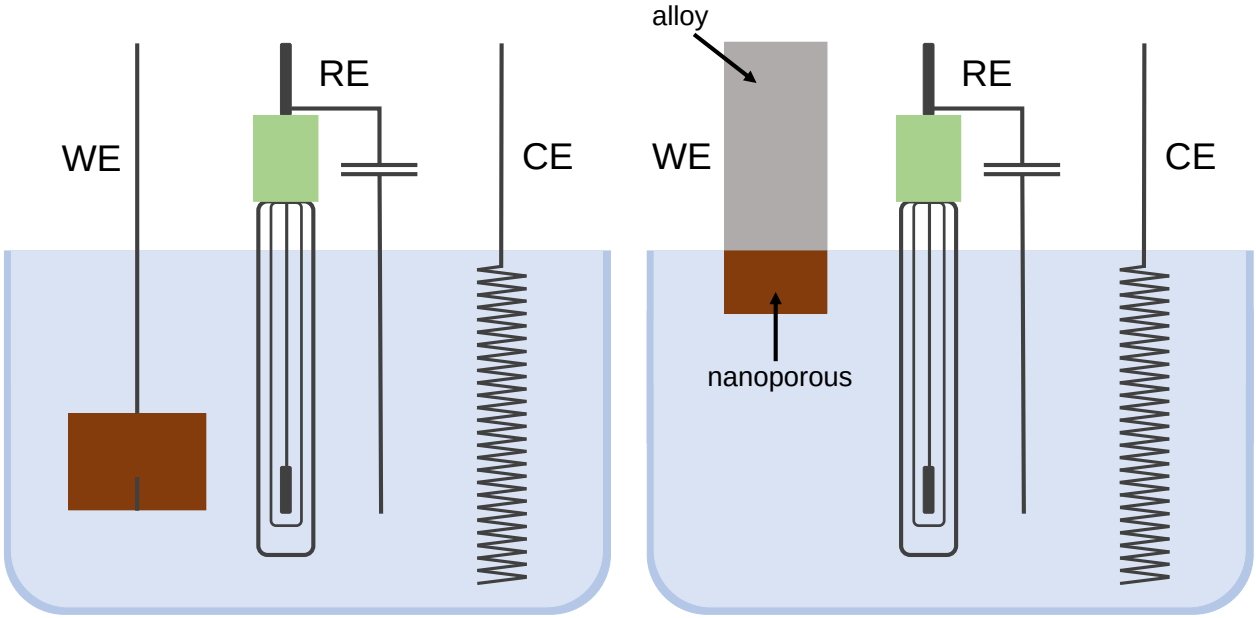

(a) Sample connected via a wire to the potentiostat.

(b) Sample directly connected to the potentiostat, lower part of the alloy is nanoporous.

Figure 15: Schematic representation of the electrochemical cell setup. WE stands for working electrode, RE for reference electrode with the additional parallel-connection with a capacitance, CE for counter electrode.

Most impedance spectra after electrochemical reduction (Sect. 4.3) are recorded at potentials in the double layer region. Therefore, potentials of 200 mV for npAu and of 150 mV or 125 mV for npPd are used for recording spectra in the double layer region. The spectra of the inital alloy and the spectra right after dealloying covered with primary oxide are recorded at the open circuit potential, to prevent a charge transfer. For further analysis, the impedance spectrum is fitted with an equivalent circuit by the impedance data analysis tool of the NOVA software. Two different parameters are used to determine the convergence of a fit. The first is the maximum change in the χ^2 parameter. If the absolute change in χ^2 is lower than a certain value, the fitting of the circuit stops. This value is set to 0.001 for the simulations. The second parameter is the maximum number of iterations without improvement. If the χ^2 value does not change after 50 iterations, the calculation stops and the fit has converged[24]. All equivalent circuits used in this chapter fulfill these requirements.

4 Results

In the following chapter equivalent circuits following the theories of de Levie [18] and Keiser et al. [19], and Eloot et al. [22] are applied to obtain a better understanding of impedance spectra. The spectra have different shapes and certain parts are assigned to the corresponding elements of the circuit. Most investigations concerning the determination of the ideal equivalent circuit have been made on nanoporous gold. For comparison nanoporous palladium has been studied.

4.1 EIS Prior to Dealloying ($Ag_{75}Au_{25}$)

An $Ag_{75}Au_{25}$ master alloy electrode acts as a flat electrode. The recorded impedance spectrum is shown in Fig. 16a, the absence of a semicircle indicates that no faradaic reactions occurs. Therefore the corresponding equivalent circuit as shown in Fig. 16b consists of the electrolyte resistance R_e, one RC element and one RQ element. Since the spectrum does not have a uniform slope, the circuit needs more than one RC or RQ element to produce an acceptable fit. The two charge transfer resistances have values in the kΩ range, so almost no current flows through these components. This is an indication of a purely capacitive behavior as already mentioned.

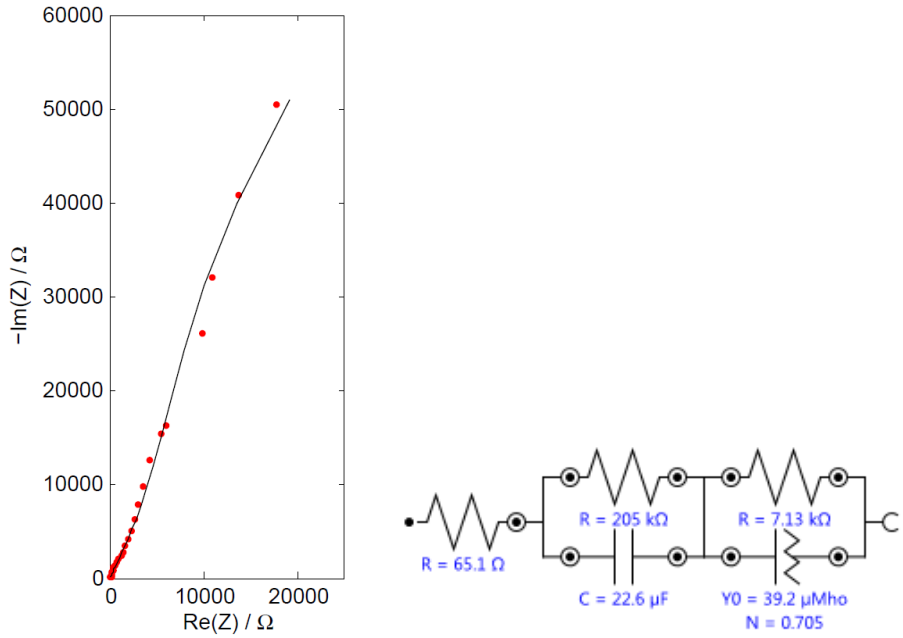

(a) Measured impedance spectrum (red dots) and fit by equivalent circuit (b) (black)

(b) Equivalent circuit consisting of the electrolyte resistance R_e, one RC element and one RQ element

Figure 16: Impedance spectrum of $Ag_{75}Au_{25}$ recorded at 240 mV with frequencies between 100000 and 0.13 Hz, the equivalent circuit is represented and the corresponding fit is added to the spectrum.

4.2 EIS after Dealloying (npAu, npPd)

After the electrochemical dealloying process in aqueous electrolytes, the nanoporous electrode is typically covered by a primary oxide. This strongly oxidized state is only obtained directly after dealloying and can not be reproduced once the electrode has been reduced. The corresponding impedance spectrum of npAu in Fig. 17a consists of one arc at high frequencies and a second one in the middle to the commencing low frequency range. At very low frequencies the impedance loci increase linearly.

Fig. 17b and 17c show two different equivalent circuits for fitting the spectrum of npAu. In both circuits the first single resistance, framed blue, has almost the same value and is identified as the electrolyte resistance R_e. The equivalent circuit in Fig. 17b consists of five RC elements constructed following the transmission line model of de Levie and Keiser[18,19]. Since the sum of the first two resistances of the RC elements, framed green, is almost the resistance value of the first semicircle, it is obvious that theses two RC elements cause this high frequency arc. A better understanding of this fact is gained by looking at Fig. 18.

Comparing Fig. 18a and 18b clearly shows that a better accordance of the fitted circuit elements with the spectrum is achieved with two RC elements. The following RC elements in Fig. 17 describe the middle and low frequency part of the spectrum. For a correct and easy distinction between the two parts, the elements describing the high frequency semicircle are added in series (green), whereas the middle and low frequency part of the spectrum is represented in a typical transmission line, framed red. Such a subdivision of the equivalent circuit is made for all circuits in this section.

The first part, i.e., the high frequency semicircle of the second equivalent circuit in Fig. 17c, framed green, consists of one RC element. The subsequent part of the spectrum is described by a single RQ element, framed red. This circuit also allows to reproduce all characteristic features of the measured Nyquist plot.

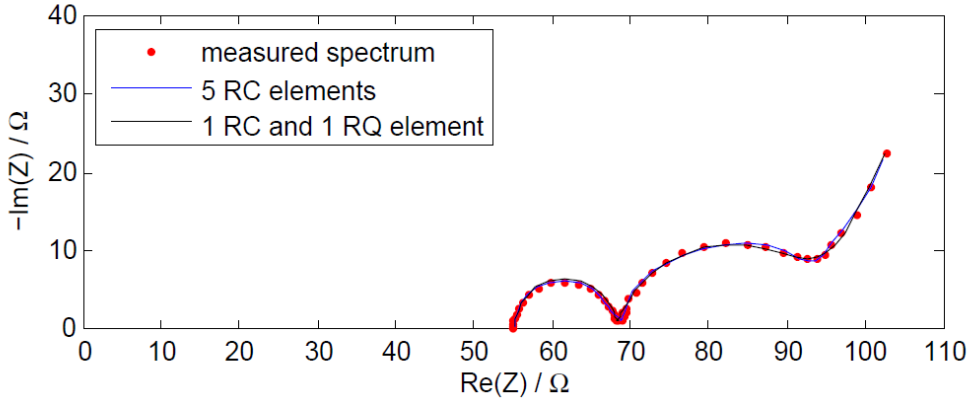

(a) Measured impedance spectrum (red dots) and fits by equivalent circuits (b) (blue) and (c) (red)

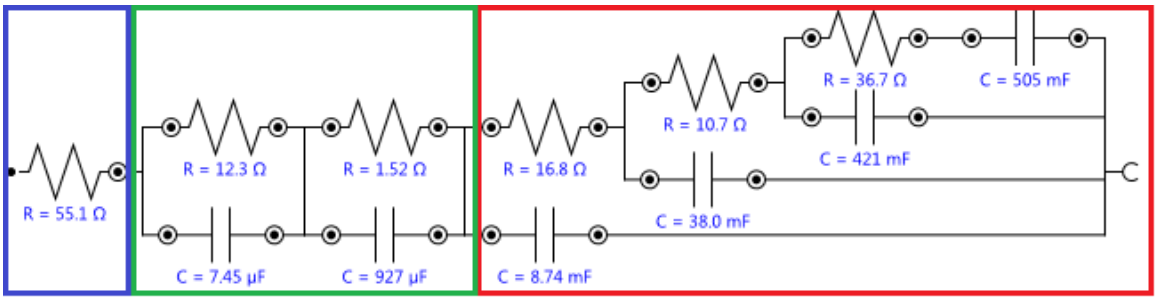

(b) Equivalent circuit consisting of five RC elements

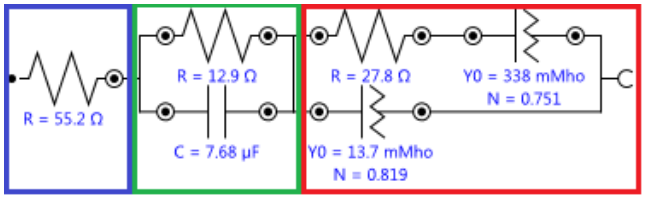

(c) Equivalent circuit consisting of one RC and one RQ element

Figure 17: Impedance spectrum of npAu recorded at 1080 mV with frequencies between 80000 and 0.01 Hz (a), with fits by the equivalent circuits presented in (b) and (c). The framed blue resistance corresponds to the electrolyte resistance of the spectrum, the framed green RC elements describe the high frequency arc, the framed red the middle and low frequency range.

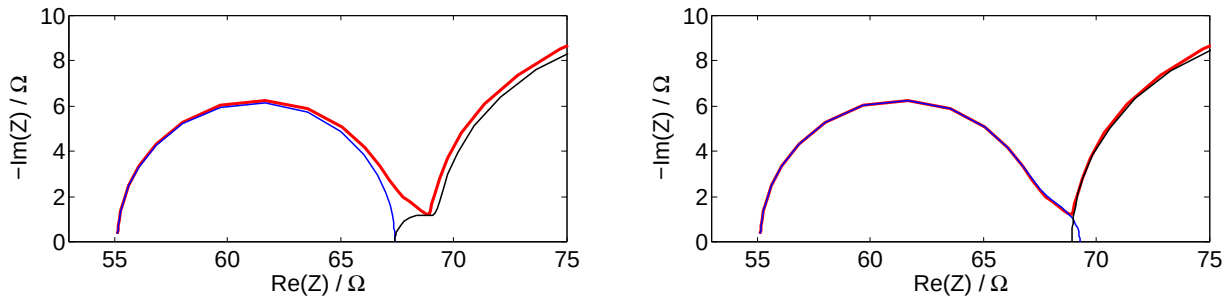

(a) Semicircle caused by one RC element

(b) Semicircle caused by two RC elements

Figure 18: Comparison of detailed impedance spectra between 53 and 75 Ω obtained for fits using one (a) or two (b) RC elements. Fit: black; measurement: red.

In contrast to npAu, the impedance spectrum of freshly dealloyed nanoporous palladium in Fig. 19a consists only of one semicircle, occurring at high frequencies. In the middle frequency range, the impedance loci has a very small slope, which proceeds into a steeper increase at low frequencies. Again two different equivalent circuits for fitting the experimental results are given (Fig. 19b and 19c). Similar to npAu, the first single resistance in both circuits, framed blue, corresponds to the electrolyte resistance R_e. The first equivalent circuit (Fig. 19b) used for fitting consists of eight RC elements and represents a typical transmission line. For the same reasons mentioned for npAu, the first three green framed RC elements represent the high frequency semicircle. The remaining part of the circuit, framed red, belongs to the increasing impedance loci in the middle and low frequency range. In contrast to 17b, a parallel-connected resistance to the last capacitance in the transmission line is necessary to give a proper fit. The second equivalent circuit, shown in Fig. 19c, is very similar to 17c and consists of one green framed RC and one red framed RQ element, where the RC element describes the high frequency semicircle and the RQ element the remaining part of the spectrum. As already mentioned, by fitting the impedance spectrum with RQ elements, the number of circuit elements decreases. However, in general lower fit qualities are obtained for npPd compared to npAu.

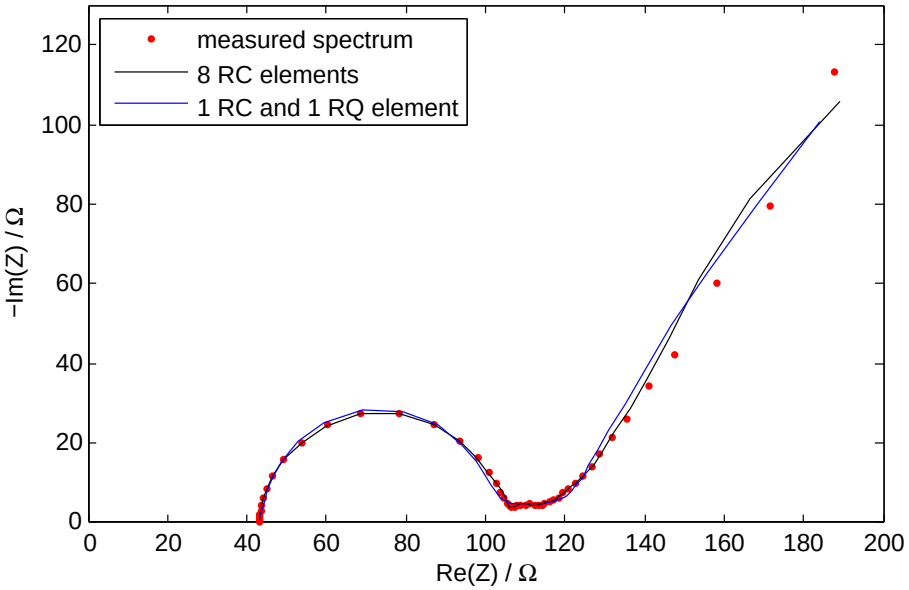

(a) Measures impedance spectrum (red dots) and fits by equivalent circuits (b) (black) and (c) (blue)

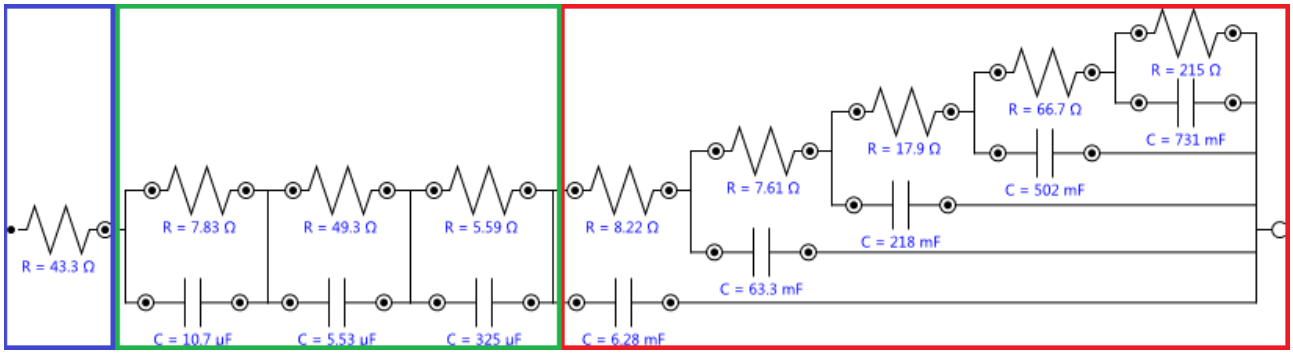

(b) Equivalent circuit consisting of eight RC elements

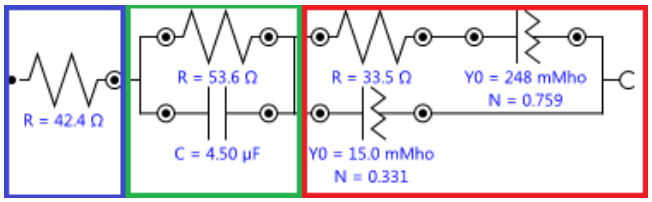

(c) Equivalent circuit consisting of one RC and one RQ element

Figure 19: Impedance spectrum of npPd recorded at 550 mV with frequencies between 100000 and 0.001 Hz (a). Equivalent circuits in (b) and (c). As for npAu (Fig. 18), blue frame: electrolyte resistance; green frame: high frequency arc; red frame: middle and low frequency range.

4.3 EIS after Electrochemical Reduction (npAu, npPd)

The primary oxide is removed by CV–cycling consisting of two cycles in a potential range of -200 – 1200 mV for npAu and of three cycles in a potential range of -300 – 1100 mV for npPd. The corresponding cyclic voltammogram for npAu is shown in Fig. 20a, and for npPd in Fig. 20b. The CV starts at the potential where the impedance spectra are recorded. Since the freshly dealloyed state (red circle) is a highly oxidized one, a jump in the potential from the open circuit potential, which lies in the oxygen regime, to the potential of impedance spectrum recording (double layer regime) results in a large current. This large current is not fully displayed in the cyclic voltammograms. Since the CV measurement starts in the negative direction, the major part of the sample gets reduced by the large current flow at the beginning. Therefore the oxygen desorption peak (red circle, cathodic peak in oxygen regime) is almost similar to the electrochemical reduced one (blue circle). During the irreversible oxygen reduction, a reordering of the structure is possible.

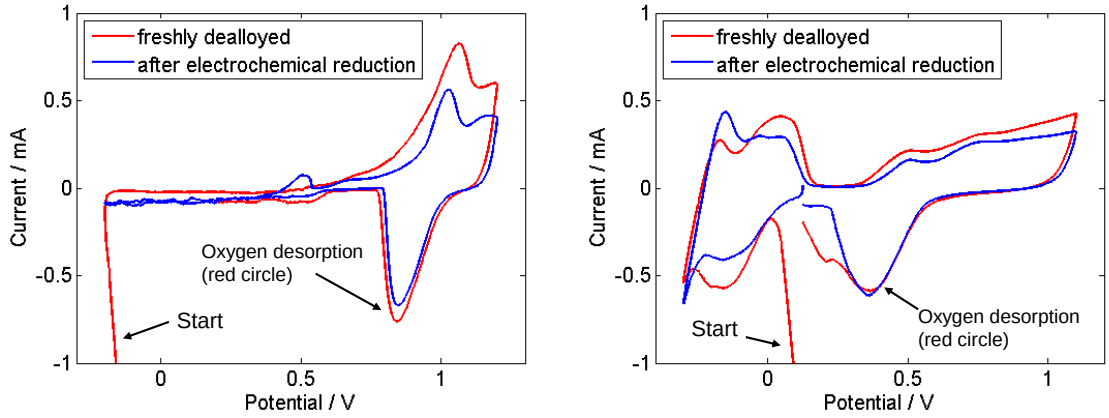

(a) CV of npAu **(b)** CV of npPd

Figure 20: Cyclic voltammograms of npAu and npPd recorded in 10 mM $HClO_4$ and at a scan rate of 0.1 mVs^{-1} of the freshly dealloyed state (red) and after electrochemical reduction (blue).

Since this metallic state is the desired one, great attention is paid to the analysis of the spectra and on a high quality of the fitted equivalent circuits. The determination of the total double layer capacitance, the pore resistance and the subsequent calculation of the pore radius and pore length is done with electrodes in this state. The spectrum of npAu is much easier to fit compared to npPd. Different types of equivalent circuits have been used to approximate the gold spectrum.

The impedance spectrum of the nanoporous gold sample in Fig. 21a shows two negative data points (Fig. 21b) at very high frequencies (100000 Hz and 69643 Hz), which are an indication for an inductive contribution. These two data points are measurements artefacts. Since this contribution decreases with decreasing frequencies, these data points can be neglected. Therefore the impedance spectrum for this npAu sample starts in the following sections at the third measurement point, which is recorded at a frequency of 48502 Hz. Since the frequency points are log spaced between the starting and end point, atypical values like 69643 Hz or 48502 Hz occur (see below e.g. Fig. 22).

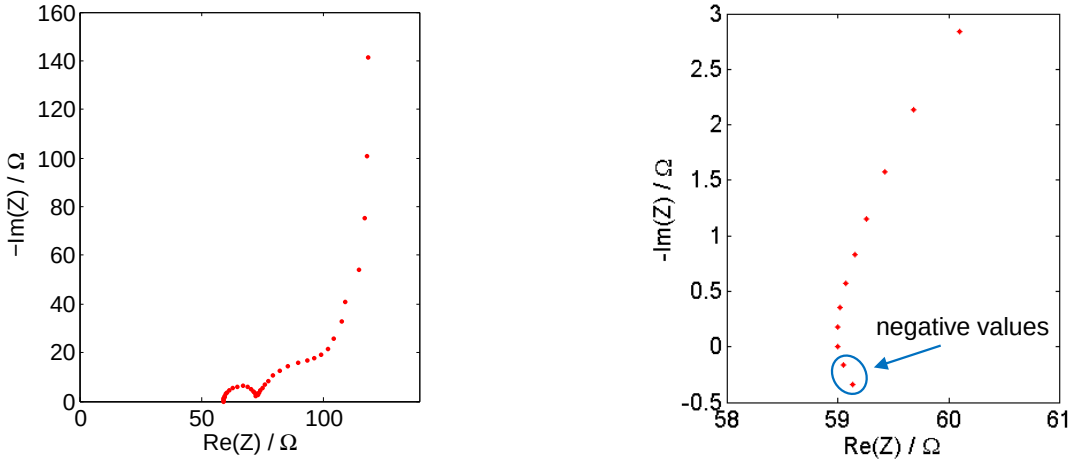

(a) Impedance spectrum

(b) Enlarged very high frequency part of the impedance spectrum (a)

Figure 21: Impedance spectrum of npAu recorded at 200 mV with frequencies between 100000 and 0.017 Hz

4.3.1 Equivalent Circuits after de Levie and Keiser (RC Elements, npAu)

As one can see in Fig. 22 for npAu, the impedance spectrum after stripping differ from those with a primary oxide (Fig. 17). Especially the low frequency part has a steeper increase in the impedance loci. The only similarity in the spectra is the high frequency arc. In the middle and low frequency regime, the npAu spectrum has at first a quarter circular-like behavior with a subsequent nearly vertical increase in the imaginary part of the impedance.

In Fig. 23a, 23b, 23c and 23d equivalent circuits with a different number of RC elements following the theories of de Levie and Keiser are shown for npAu. Again the first resistance, framed blue, corresponds to the electrolyte resistance. R_e varies only marginally over the four circuits. In the Fig. 23a, 23b and 23c, the first RC element, framed green, describes the high frequency semicircle, as shown in Fig. 24a. The semicircle in Fig. 23d is described by the first two RC elements, framed green. This can be demonstrated by comparing 24b and 24c: By fitting the semicircle with only one RC element, the accordance of the equivalent circuit

with the measured spectrum is not given. A better fit quality is obtained, if the semicircle is described by two RC elements. The remaining RC elements, framed red, correspond to the middle and low frequency regime of the spectrum. To distinguish the particular parts of the equivalent circuit, the RC elements corresponding to the high frequency semicircle are added in series after the electrolyte resistance. The remaining elements are added in the transmission line and describe the middle and low frequency part of the spectrum.

The circuit 23a consisting only of three RC elements in figure shows some deviations from the spectrum in the middle frequency regime, where a quarter circular-like shape occurs. Circuits with four and more RC elements exhibit a very good accuracy and the difference in their fits is very small. Therefore the fit quality increases with the number of RC elements, but physical interpretation becomes more complex.

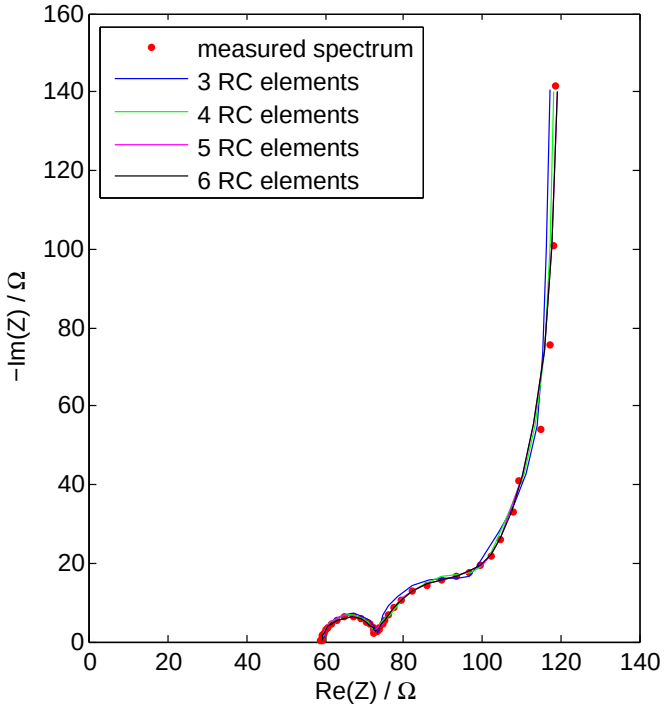

Figure 22: Impedance spectrum (red dots) of npAu recorded at 200 mV with frequencies between 48502 and 0.017 Hz with fits according to equivalent circuits 23a (blue), 23b (green), 23c (magenta) and 23d (black).

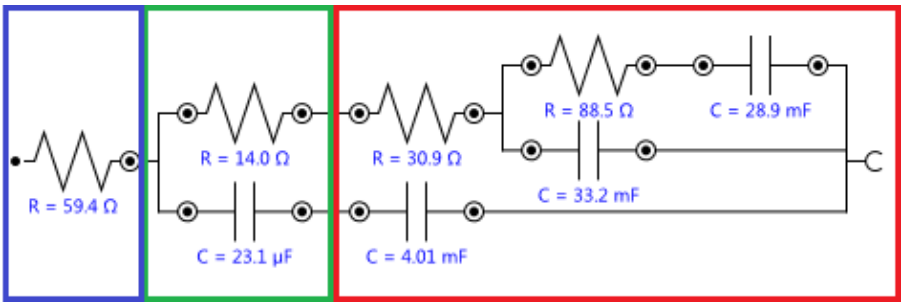

(a) Equivalent circuit consisting of three RC elements

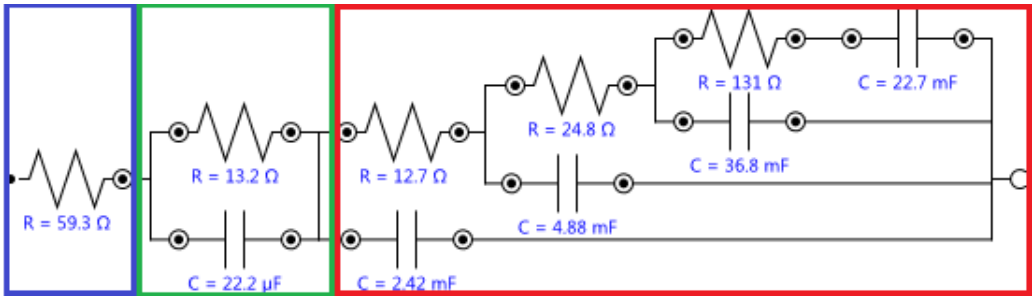

(b) Equivalent circuit consisting of four RC elements

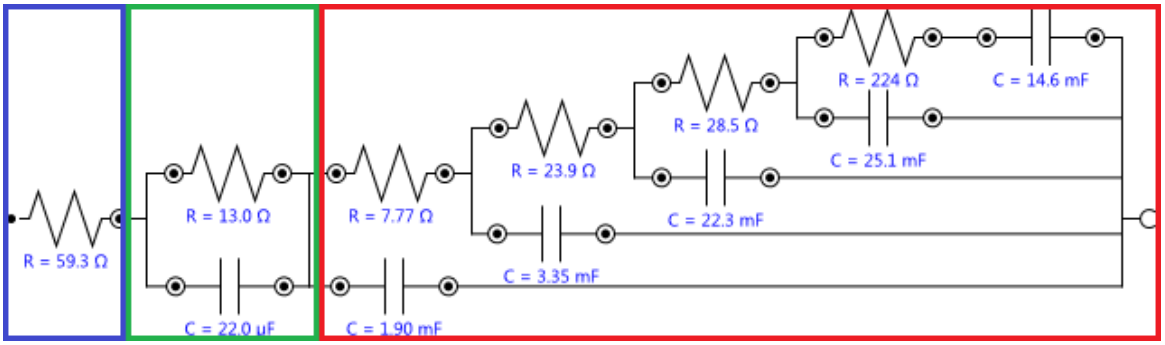

(c) Equivalent circuit consisting of five RC elements

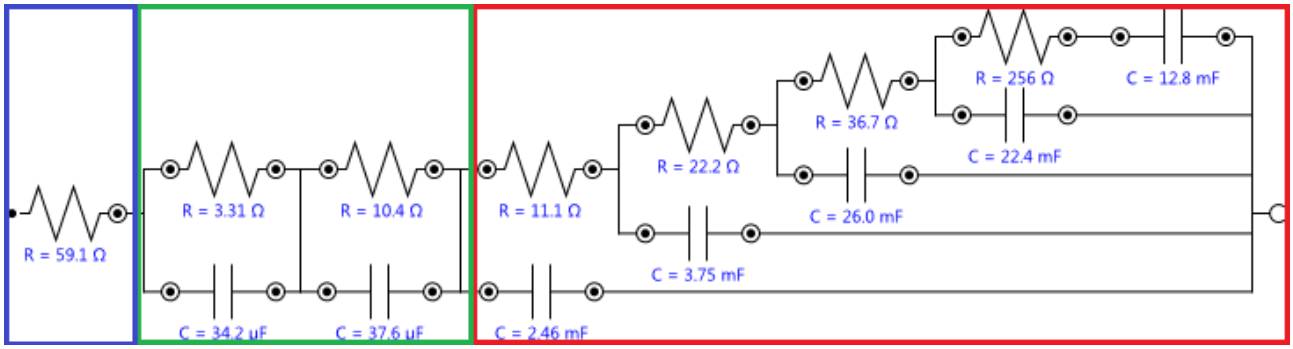

(d) Equivalent circuit consisting of six RC elements

Figure 23: Equivalent circuits of the impedance spectrum of npAu shown in Fig. 22. As for npAu (Fig. 18), blue frame: electrolyte resistance; green frame: high frequency arc; red frame: middle and low frequency range.

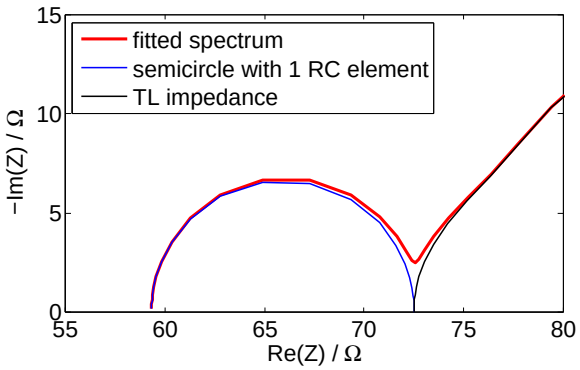

(a) Fit of first semicircle in 23a, 23b and 23c by of one RC element

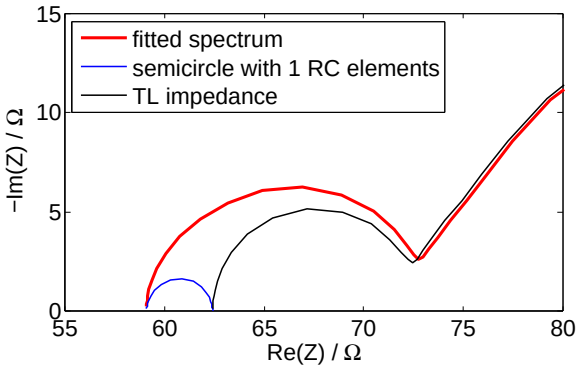

(b) Fit of first semicircle in 23d consisiting of one RC element

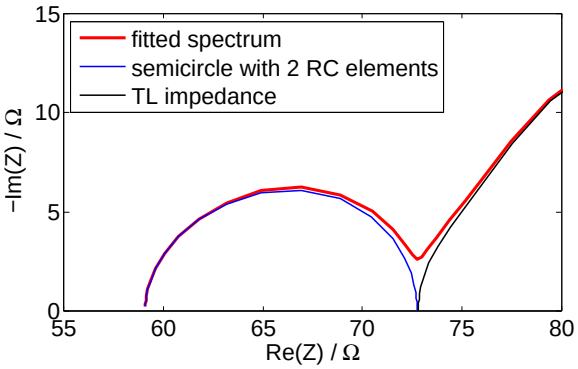

(c) Fit of first semicircle in 23d consisiting of two RC element

Figure 24: Comparison of part of the impedance spectra between 55 Ω and 80 Ω obtained for fits of Fig. 23. The high frequency semicircle is fitted using one RC element in (a) and (b), or two RC elements in (c). The red fitted spectrum labels the whole equivalent circuit, the blue spectrum corresponds to the high frequency semicircle, fitted by one or two RC elements, and the black transmission line impedance spectrum describes the remaining RC elements in the circuit.

4.3.2 Equivalent Circuits after de Levie and Keiser (RC/RQ Elements, npAu)

In Fig. 25a, the same impedance spectrum of npAu as in Fig. 22 was fitted with a transmission line consisting of one RC element and two RQ elements, which is shown in 25b. The RC element, framed green, fits the high frequency semicircle and the RQ elements, framed red, are needed for the remaining spectrum. The value of the electrolyte resistance and the impedance of the semicircle are in good accordance with the circuits above. It should be pointed out that the exponent N of the last constant phase element has a value larger than one. The exponent N should only have values between 0 and 1. Therefore although the fit accuracy is very good, the validity is questionable. Equivalent circuits with less or more than two RQ elements do not provide the desired quality.

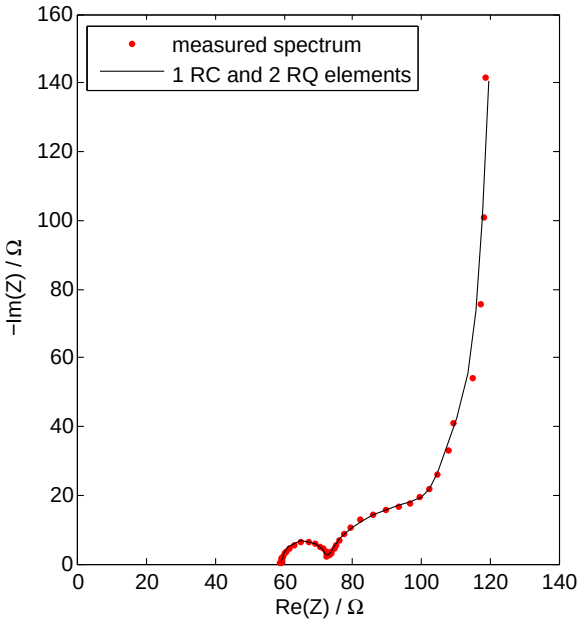

(a) Impedance spectrum and fitted equivalent circuit (b)

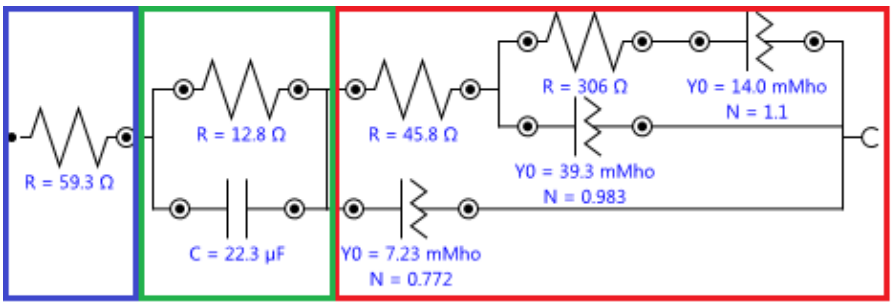

(b) Equivalent circuit consisting of one RC and two RQ elements

Figure 25: Analysis of impedance spectrum of Fig. 22 (npAu, 200 mV, 48502-0.0017 Hz) with RC element (high frequency arc, green framed) and RQ elements (middle and low frequency, red framed). Blue frame: electrolyte resistance.

4.3.3 Equivalent Circuits after Eloot (RC Elements, npAu)

The impedance spectrum of npAu (Fig. 26) has been fitted with an equivalent circuit given in Fig. 27 based on the theory following Eloot et al.[22]. In Sect. 2.4.2, the particular parts of the equivalent circuit have been explained. The electrode impedance is neglected in the used equivalent circuit. To fit the entire spectrum with this model, an additional RC element for the high frequency arc, framed green, has to be added between the electrolyte resistance and the transmission line. The value of R_e, framed blue, and the impedance of the semicircle, framed green, are again in good accordance with the values obtained in the measurements above. Eloots equivalent circuit fits the middle and the low frequency part of the spectrum with high quality.

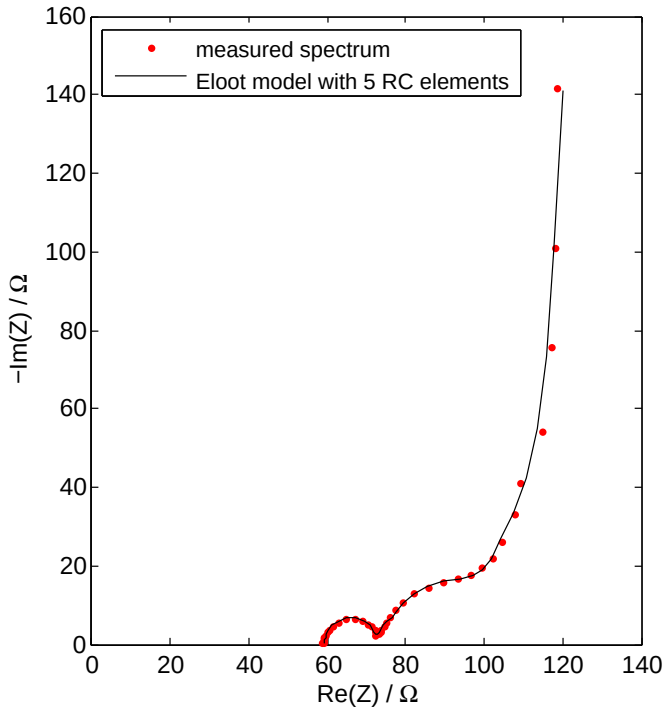

Figure 26: Analysis of impedance spectrum of Fig. 22 (npAu, 200 mV, 48502-0.0017 Hz) with an equivalent circuit after Eloot.

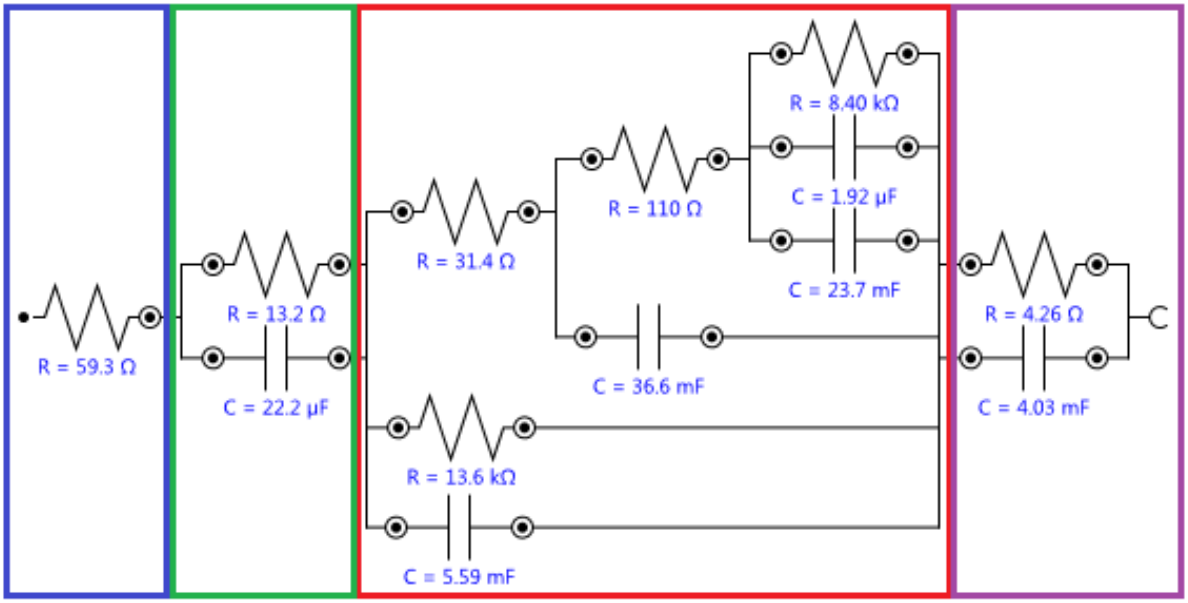

Figure 27: Equivalent circuit corresponding to the model after Eloot for the npAu spectrum shown in Fig. 26. Blue frame: electrolyte resistance; green frame: high frequency arc; red frame: middle and low frequency part; violet frame: material layer impedance.

4.3.4 Modified Equivalent Circuits after Eloot (RC Elements, npAu)

By further neglecting the pore mouth resistance and pore base impedance of the model following the theory of Eloot, the impedance spectrum of npAu (Fig. 28) is fitted with the modified equivalent circuits shown in Fig. 29.

In the equivalent circuit in 29a, the high frequency arc is modeled by only one RC element, framed blue, in contrast to those one shown in 29b and 29c, where two elements are needed to fit the semicircle. The middle and low frequency part, framed red, of all circuits is again described by the Eloot model with a different number of elements. By neglecting the high Ohmic resistances, as described above, the fits can be improved further.

The only difference between the modified Eloot circuits presented in 29 and the transmission line model of de Levie and Keiser (Fig. 23) is the additional material layer impedance, framed violet, which is the last element in the circuits according to Eloot.

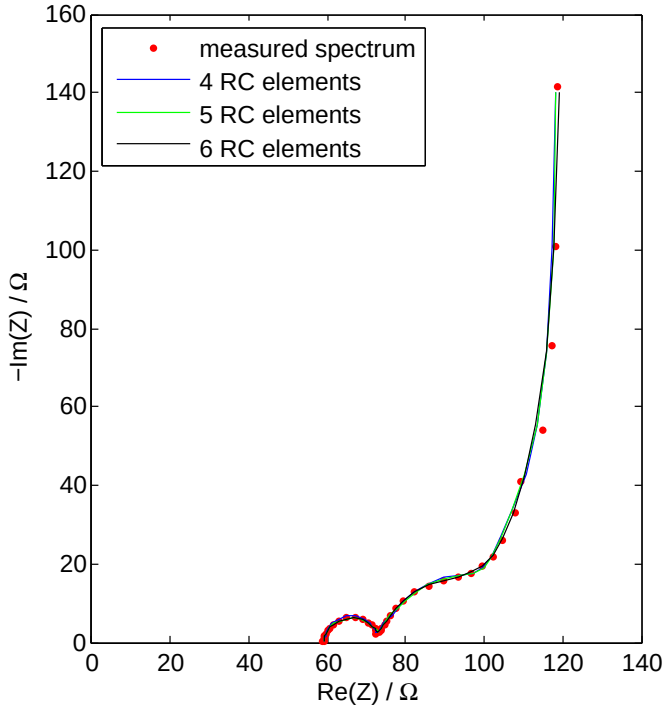

Figure 28: Analysis of Fig. 22 with modifed Eloot model. Equivalent circuits see Fig. 29a, b, c.

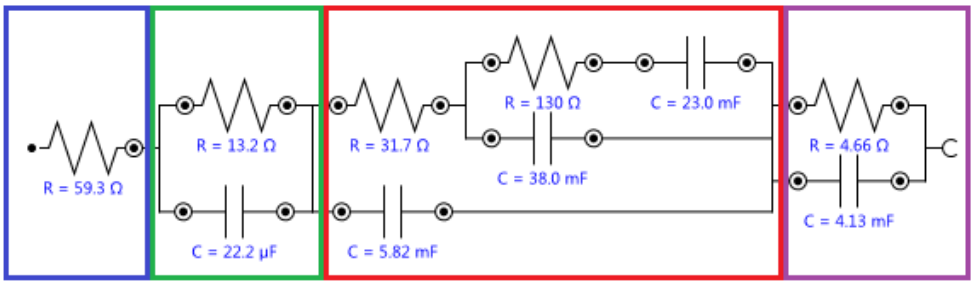

(a) Equivalent circuit consisting of four RC elements

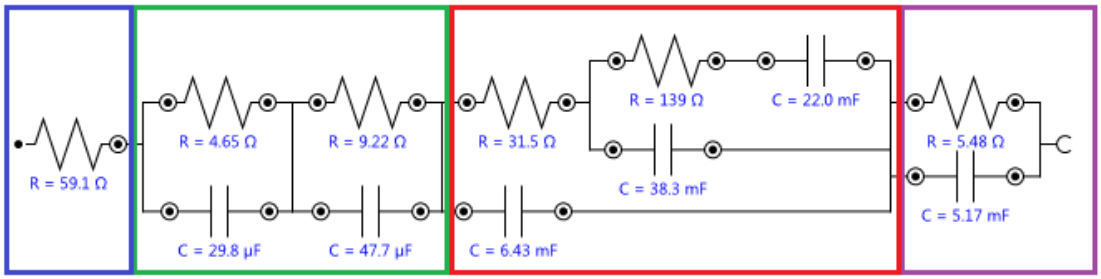

(b) Equivalent circuit of five RC elements

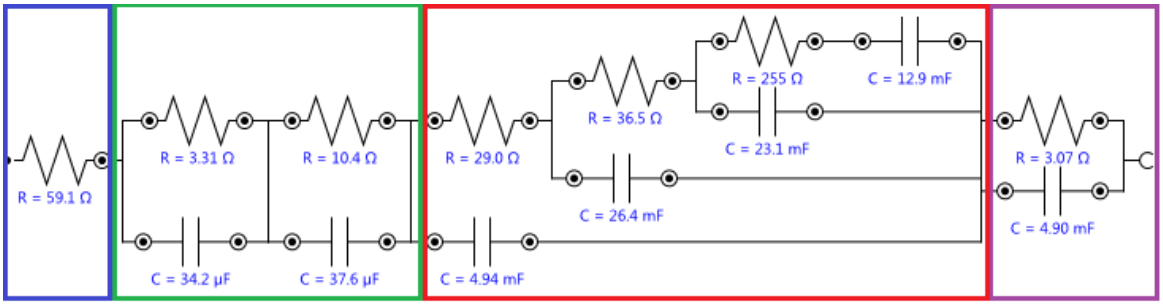

(c) Equivalent circuit consisting of six RC elements

Figure 29: Equivalent circuits according to a modified model after Eloot for the npAu spectrum shown in Fig. 28. Blue frame: electrolyte resistance; green frame: high frequency arc; red frame: middle and low frequency part; violet frame: material layer impedance.

4.3.5 Calculation of Pore Resistance and Total Capacitance (npAu)

As already mentioned in Sect. 2.4.2, the total capacitance and the pore resistance can be calculated from the equivalent circuit after Eq. (31) and (32). As discussed by Landesfeind et al.[16], only the capacities and resistances of the transmission line are used. Table 2 lists the obtained values from the model after de Levie and Keiser (Fig. 23) and the modified model after Eloot (Fig. 29). In equivalent circuits consisting of constant phase elements, e.g. circuit 25b, the CPEs have to be converted into capacities with the help of the corresponding charge transfer resistances, as mentioned in Sect. 2.4.1, Eq. (11). Since no charge transfer resistances are contained in the circuit, no conversion is possible. The equivalent circuit recommended by Eloot has a total capacitance C_{tot} = 66 mF and a pore resistance R_{pore} = 141 Ω which is in good accordance with all the other fits, but the errors are unrealistic high. The reason are the two parallel-connected resistances and capacities. Since the corresponding values of the particular elements can be interchanged within these parallel connections, the errors rise dramatically.

With the obtained capacities, the total surface area A after Eq. (30) is caluclated. A specific double layer capacitance C_{dl} between 20 and 30 $\frac{\mu\mathrm{F}}{\mathrm{cm}^2}$ [21] is used in these calculations. By knowing A and the sample mass m, the specific surface area α can be calculated via Eq. (36). Although the microbalance has a measurement uncertainty of Δm = ±0.001 mg, Δm is assumed higher, because the sample mass is calculated after dealloying and should account for incomplete etching of the less noble component. The calculated mass of the sample is $m = (25 \pm 1)$ mg. The values of the specific surface area are listed in Table 3.

Table 2: Calculated values of the total capacitance C_{tot} and the pore resistance R_{pore} of npAu with their uncertainty ΔC_{tot} and ΔR_{pore} for equivalent circuits after de Levie and Keiser (LK) and Eloot (E) with a different number of RC elements. χ^2 gives the quality of the fitted equivalent circuit.

Circuit	$\boldsymbol{\chi^2}$	$\boldsymbol{C_{\mathrm{tot}}}$ / **mF**	$\boldsymbol{\Delta C_{\mathrm{tot}}}$ / **mF**	$\boldsymbol{R_{\mathrm{pore}}}$ / **Ω**	$\boldsymbol{\Delta R_{\mathrm{pore}}}$ / **Ω**
LK 3 RC	0.0061	66	4	119	13
LK 4 RC	0.0023	67	4	168	21
LK 5 RC	0.0017	67	14	284	88
LK 6 RC	0.0011	67	13	329	119
E 4 RC	0.0023	67	3	162	18
E 5 RC	0.0015	67	2	171	18
E 6 RC	0.0011	67	13	321	114

Table 3: Calculated values of the total surface area A and the specific surface area α of npAu for equivalent circuits after de Levie and Keiser (LK) and Eloot (E) with a different number of RC elements. $C_{\mathrm{dl}} = 20 - 30\ \frac{\mu\mathrm{F}}{\mathrm{cm}^2}$, $m = 25 \pm 1$ mg.

Circuit	$\boldsymbol{A}$ / $\mathbf{cm}^2$	$\boldsymbol{\alpha}$ / $\mathbf{m}^2\mathbf{g}^{-1}$
LK 3 RC	2200 – 3300	9 – 13
LK 4 RC	2200 – 3400	9 – 14
LK 5 RC	2200 – 3400	9 – 14
LK 6 RC	2200 – 3400	9 – 14
E 4 RC	2200 – 3400	9 – 14
E 5 RC	2200 – 3400	9 – 14
E 6 RC	2200 – 3400	9 – 14

The total capacities C_{tot} in Table 2 and the specific surface area α in Table 3 stay constant in both models and are therefore independent on the number of RC elements. In contrast R_{pore}, ΔC_{tot}, and ΔR_{pore} in Table 2 increase with the number of elements. Both models are in good accordance, since for a particular number of circuit elements, the capacitance and resistance values are almost the same. Because of reasons explained in 5.1, the equivalent circuit after the model of de Levie and Keiser with 4 RC elements is the means of choice for further calculations and analysis.

4.3.6 Equivalent Circuits after de Levie and Keiser (RC Elements, npPd)

As one can see in Fig. 30, the impedance spectrum after stripping differs from those with a primary oxide (Fig. 19). In comparison to the primary oxide spectrum, the impedance spectrum of the electrochemical reduced npPd has a very small slope followed by a nearly vertical increase in impedance at low frequencies.

The spectrum of nanoporous palladium (Fig. 30a) has been fitted with the equivalent circuit presented in 30b. As already mentioned, the shape of the spectrum differs from that of nanoporous gold (e.g. Fig. 22). R_{e}, framed blue in the ciruit, is smaller compared to the npAu electrode and the high frequency semicircle, framed green, is much bigger and described by two RC elements. The remaining spectrum is fitted by the transmission line, framed red. In the very low frequency range, the fitted equivalent circuit and the spectrum differ. The fit shows a steeper increase than that observed in the measurement. A better accordance cannot be obtained by using more or less elements in the circuit.

The calculated values of the total capacitance and the pore resistance with their uncertainties are listed in Table 4. A specific double layer capacitance between 23.1 and 44.5 $\frac{\mathrm{m}^2}{g}$ and a calculated sample mass of $m = (12 \pm 1)$ mg is taken. The resulting total surface area A is therefore between 6400 and 12400 cm^2 and the specific surface area α between 53 and 103 $\frac{\mathrm{m}^2}{\mathrm{g}}$.

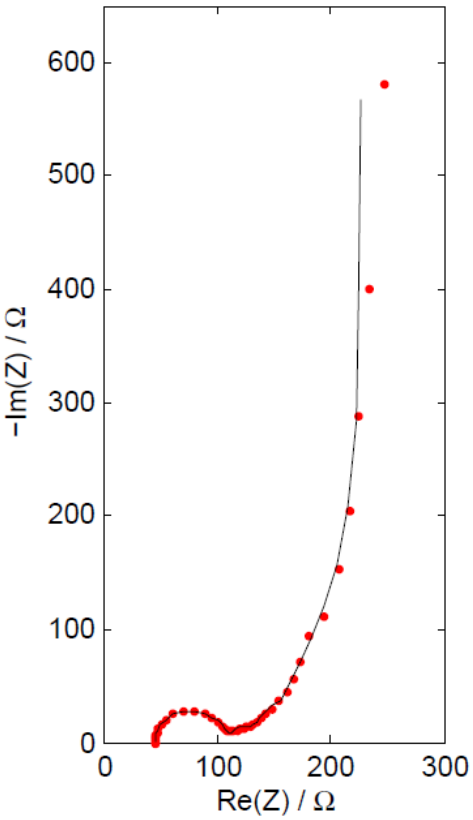

(a) Impedance spectrum and fitted equivalent circuit 30b

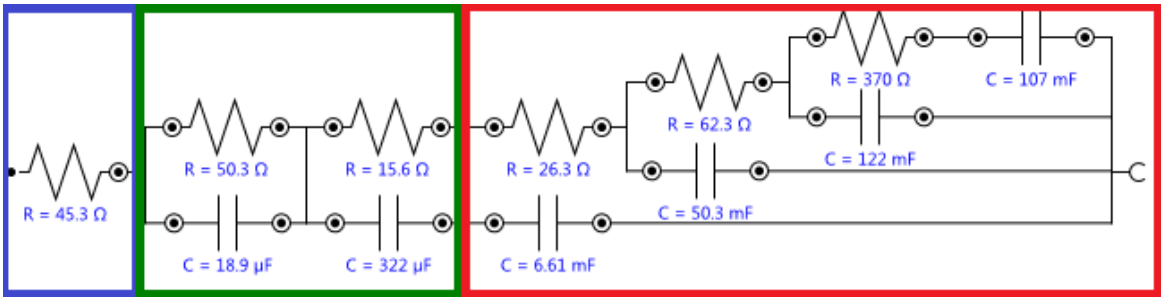

(b) Equivalent circuit consisting of five RC elements

Figure 30: Impedance spectrum of npPd without primary oxide recorded at 125 mV with frequencies between 100000 and 0.001 Hz. Equivalent circuit after the model of de Levie and Keiser (b) is added to the spectrum. Blue frame: electrolyte resistance; green frame: high frequency arc; red frame: middle and low frequency range.

Table 4: Calculated values of the total capacitance C_{tot} and the pore resistance R_{pore} of npPd with their absolute uncertainties ΔC_{tot} and ΔR_{pore} for an equivalent circuit after de Levie and Keiser (LK) consisting of five RC elements. χ^2 gives the quality of the fitted equivalent circuit.

χ^2	C_{tot} / mF	ΔC_{tot} / mF	R_{pore} / Ω	ΔR_{pore} / Ω
0.0079	286	19	457	53

4.4 EIS of a Partly Etched npAu Platelet

In the following chapter a sample is used, in which the upper part consists of the initial $Ag_{75}Au_{25}$ alloy and the lower part has been dealloyed to get a nanoporous structure. The unetched alloy part is connected by a clamp to the potentiostat, while only the nanoporous part of the sample was immersed in the electrolyte, as shown in the electrochemical cell setup Fig. 15b. In such a sample setup, no additional wire is needed for connection.

Impedance spectra were measured at two different immersion depths of the nanoporous sample. For the spectrum shown in Fig. 31a, only the nanostructured part was in contact with the electrolyte. In contrast to all other spectra presented so far, no high frequency arc is observed. Instead the impedance loci rise linearly at high frequencies and show a steep increase towards the middle and low frequency range. This can be explained directly via the equivalent circuit (Fig. 31b), which consists only of R_e, framed blue, and the framed blue transmission line. The fit of the circuit perfectly matches the spectrum.

In Fig. 32a, besides the nanostructure also part of the alloy was in contact with the electrolyte. At a first glance the spectrum shows no difference compared to that one presented in Fig. 31. However, when magnifying the high frequency part, as shown in Fig. 32b, a small arc becomes visible. This behavior is also represented in the equivalent circuit Fig. 32c. In this circuit, an additional RC element appears, framed green, which describes the high frequency shape of the spectrum. The element causing the arc has been separated from the transmission line.

To summarize this observation, if only the nanostructured part is in contact with the electrolyte, no additional high frequency arc is observed. If also the alloy is immersed, a semicircle appears, which is however small compared to the samples discussed in Sect. 4.3.

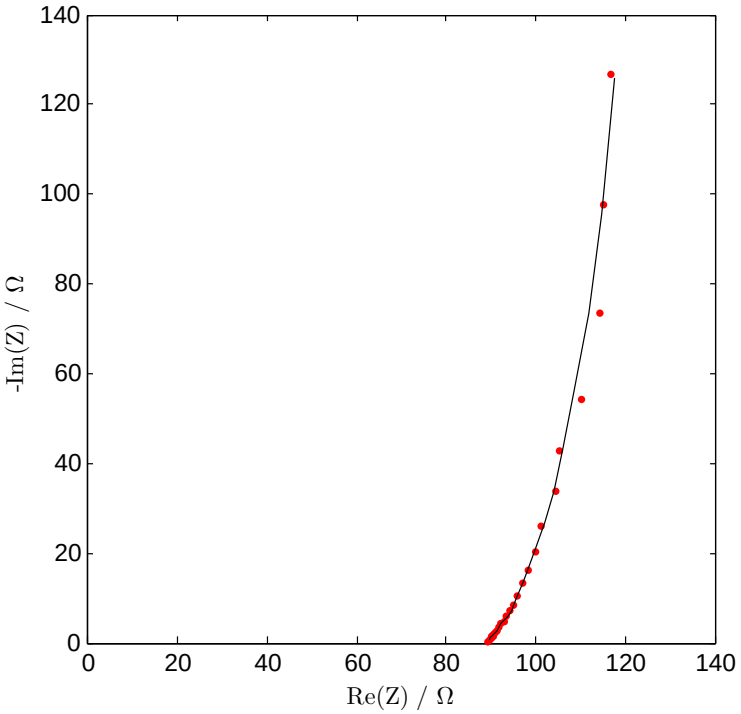

(a) Impedance spectrum and fitted equivalent circuit (b)

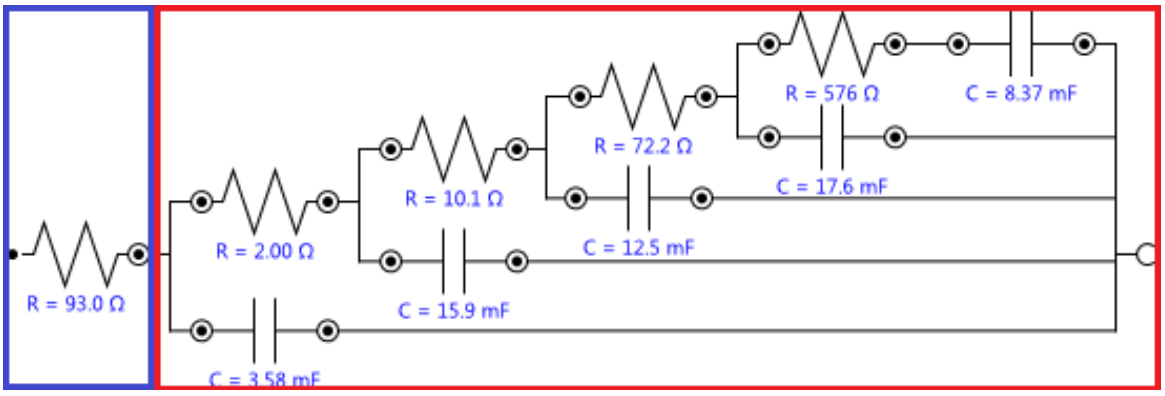

(b) Equivalent circuit consisting of five RC elements

Figure 31: Impedance spectrum (a) of npAu at 200 mV and frequencies between 100000 and 0.02 Hz. Only the nanoporous structure is in contact with the electrolyte. The equivalent circuit (b) is presented and the corresponding fit is added to the spectrum. Blue frame: electrolyte resistance; red frame: middle and low frequency range.

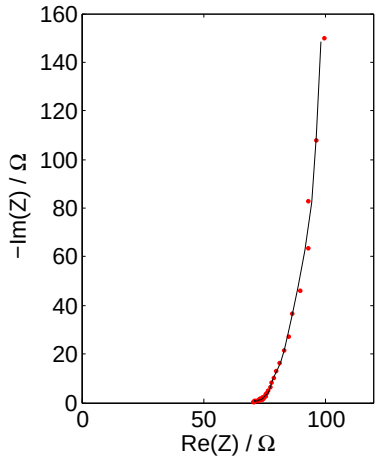

(a) Impedance spectrum and fit according equivalent circuit 32c

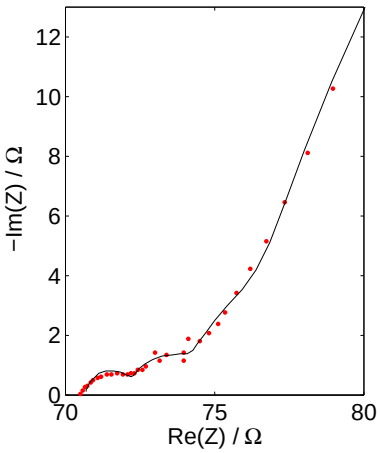

(b) detailed impedance spectrum between 70−80 Ω and fitted equivalent circuit 32c

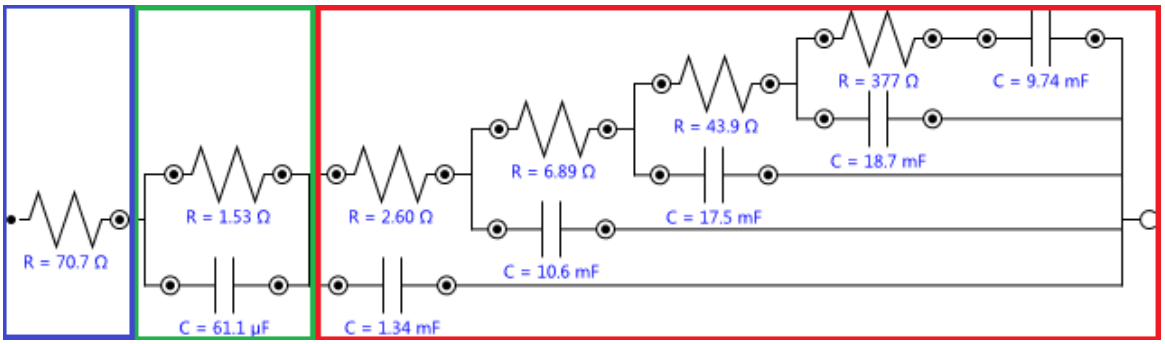

(c) Equivalent circuit consisting of five RC elements

Figure 32: Impedance spectrum of npAu (a) at 200 mV and frequencies between 26827 and 0.02 Hz, with magnification shown in (b). Compared to Fig. 31, both the nanoporous structure and the $Ag_{75}Au_{25}$ alloy is in contact with the electrolyte. The equivalent circuit is presented in (c) and the corresponding fit is added to the spectrum. Blue frame: electrolyte resistance; green frame: high frequency arc; red frame: middle and low frequency range.

4.5 EIS after Coarsening (npAu)

In the following section two nanoporous gold electrodes, which were produced and strucutally coarsened under different conditions, are investigated. The sample shown in Fig. 33 was dealloyed in 0.1 M H_2SO_4 and is labeled as sample A, whereas for the sample in Fig. 34 1 M $HClO_4$ was used and is labeled as sample B. In this context one has to draw attention to the different shape of the initial states of the two nanoporous electrodes. Not only the electrolyte resistance, but also the high frequency arc is different. Sample A dealloyed in H_2SO_4 shows a more semicircle like behavior in the middle frequency range, whereas sample B prepared via $HClO_4$ has a more quarter circular-like shape. The npAu sample shown in Fig. 34 has been discussed in detail in the Sect. 4.1, 4.2 and 4.3. The initial state spectra of the two npAu electrodes have been fitted with an equivalent circuit after the model of de Levie and Keiser (Fig. 33c and 34c). The last resistance in Fig. 33c is very large and has an uncertainty of 25%, so the reliability has to be viewed sceptically.

Since the specimen has been removed from the electrolyte during aging, the distance between the electrode and the reference electrode can change upon re-inserting of the specimen into the electrochemical cell. This causes a different electrolyte resistance before and after coarsening [25]. Sample A in Fig. 33 was aged at ambient conditions, sample B in Fig. 34 for two hours at 150°C. The final sample states are presented in the Fig. 33b and 34b. While the initial states of the samples are different, the coarsened ones have more in common. The electrolyte resistance decreases in both spectra after coarsening and the high frequency arc increases. These facts can also be proved by the equivalent circuits shown in Fig. 33d and 34d. Both hf semicircles are described by two RC elements. Furthermore the shape of the middle and low frequency range tends more towards a linear behavior, with a slope of about 45°. In the very low frequency part, however, significant differences are observed. The sample in Fig. 33b shows a less steep increase in the impedance loci than the sample shown in Fig. 34b. By comparing these very low frequency parts of the spectra with the initial states Fig. (33 and 34), the shapes stayed almost the same. Therefore the coarsening process changes primarily the high and middle frequency range. However, the impedance spectra of the coarsened sample due to various electrochemical treatments changed much more than those coarsened at higher temperatures, where still a slight similarity in the middle frequency range can be observed.

Since the pore resistance changes significantly with the equivalent circuit size, the same number of RC elements in the circuit before and after coarsening should be used for comparing the calculated values of C_{tot} and R_{pore}. In Table 5 the values of the fitted spectra are listed. The total capacitance decreases in both samples after coarsening. While for the sample aged due to a variety of electrochemical treatments the capacitance changes only from (35 ± 2) mF to (22 ± 2) mF, the capacitance of the sample coarsened at 150°C changes from (67 ± 4) mF to (28 ± 1) mF. The uncertainties of the pore resistances are high compared to those of the

capacities. From the capacities, the surface areas A are calculated after Eq. (30) by using a specific double layer capacitance between 20 and 30 $\frac{\mu F}{cm^2}$ [21]. Table 6 shows the specific surface areas α, calculated according to Eq. (36) by using the surface areas A and the sample masses m. Since the values of α are independent of the sample geometry and their mass, they can be compared directly. The specific surface areas before coarsening match well in spite of the different dealloying procedure. After coarsening, the values differ, which can be assigned to different levels of aging, which is explained in more detail in Sect. 5.2.

Table 5: Calculated values of the total capacitance C_{tot} and the pore resistance R_{pore} of npAu before and after coarsening with their absolute uncertainties ΔC_{tot} and ΔR_{pore}. Equivalent circuits after de Levie and Keiser were used. χ^2 gives the quality of the fitted equivalent circuit. The sample aged due to a variety of electrochemical treatments is labeled with npAu 1, the sample coarsened at 150°C with npAu 2. The states i and c denote initial and coarsened state, respectively.

sample	**state**	χ^2	C_{tot} / mF	ΔC_{tot} / mF	R_{pore} / Ω	ΔR_{pore} / Ω
npAu 1	i	0.0018	35	2	4000	1000
npAu 1	c	0.0020	22	2	1300	200
npAu 2	i	0.0023	67	4	280	90
npAu 2	c	0.0008	28	1	190	20

Table 6: Calculated values of the total surface area A and the specific surface area α of npAu before and after coarsening. Sample npAu 1: aged due to a variety of electrochemical treatments; Sample npAu 2: coarsened at 150°C. The states i and c denote initial and coarsened state, respectively. For calculations, the double layer capacities are taken from Table 5, the specific double layer capacitance is chosen between 20 and 30 $\frac{\mu F}{cm^2}$ and the masses are $m = (12 \pm 1)$ mg for sample npAu 1 and $m = (25 \pm 1)$ mg for sample npAu 2.

sample	**state**	A / cm^2	α / m^{2}g^{-1}
npAu 1	i	1200 - 1800	10 - 15
npAu 1	c	700 - 1100	6 - 9
npAu 2	i	2200 - 3400	9 - 14
npAu 2	c	900 - 1400	4 - 6

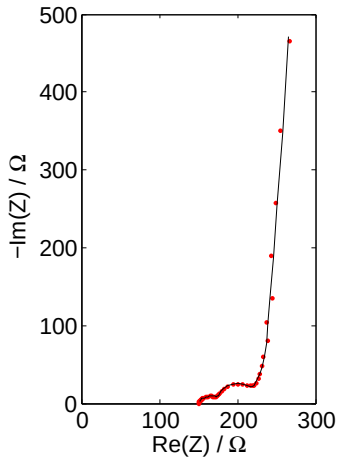

(a) Impedance spectrum and fitted equivalent circuit (c)

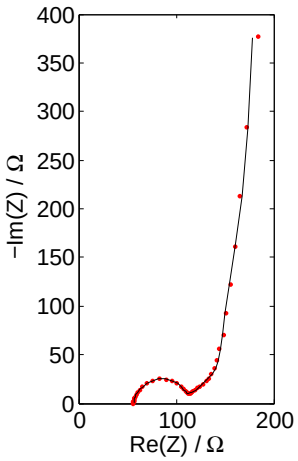

(b) Impedance spectrum after coarsening and fitted equivalent circuit (d)

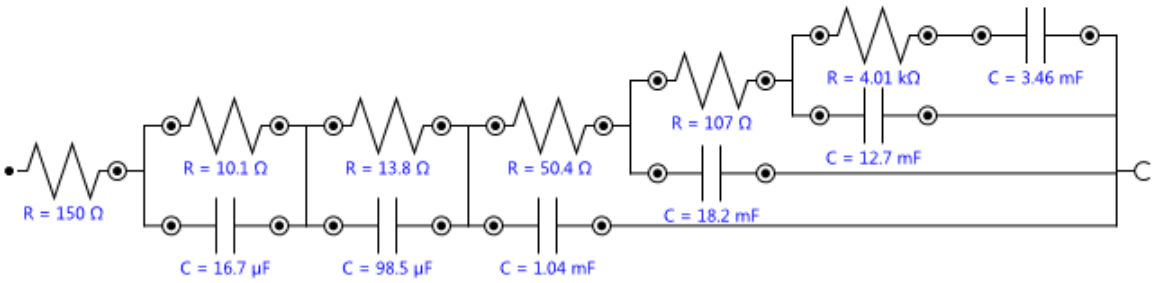

(c) Equivalent circuit for spectrum (a) consisting of five RC elements

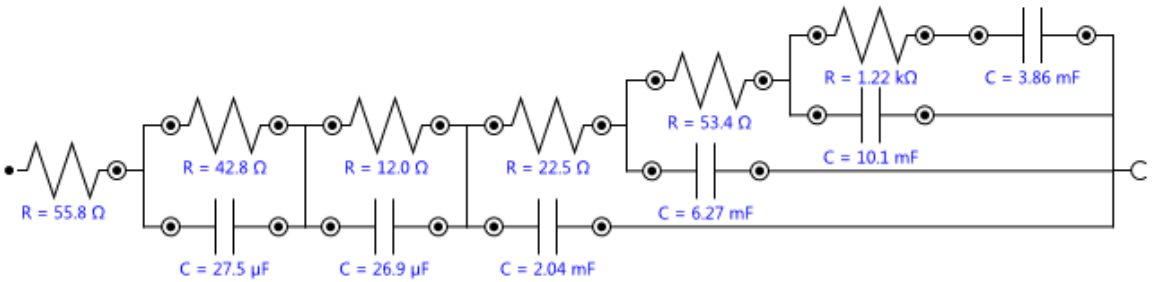

(d) Equivalent circuit for spectrum (b) consisting of five RC elements

Figure 33: Impedance spectrum of npAu prepared by dealloying in H_2SO_4 before and after coarsening. Spectra were recorded at 200 mV with frequencies between 100000 and 0.01 Hz before and with frequencies between 100000 and 0.02 Hz after aging at ambient conditions. The equivalent circuits are presented and the corresponding fits are shown the spectra.

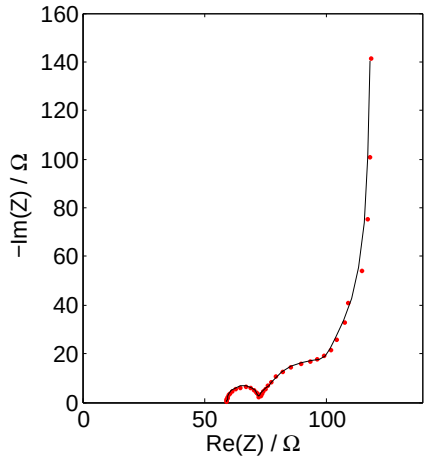

(a) Impedance spectrum and fitted equivalent circuit (c)

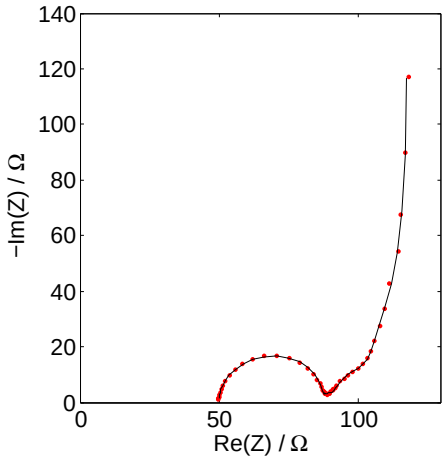

(b) Impedance spectrum after coarsening and fitted equivalent circuit (d)

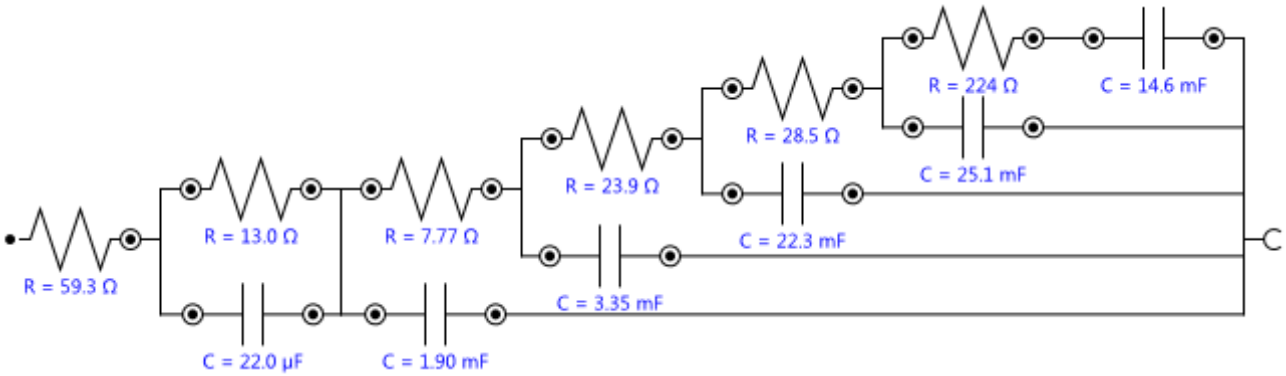

(c) Equivalent circuit for spectrum (a) consisting of five RC elements

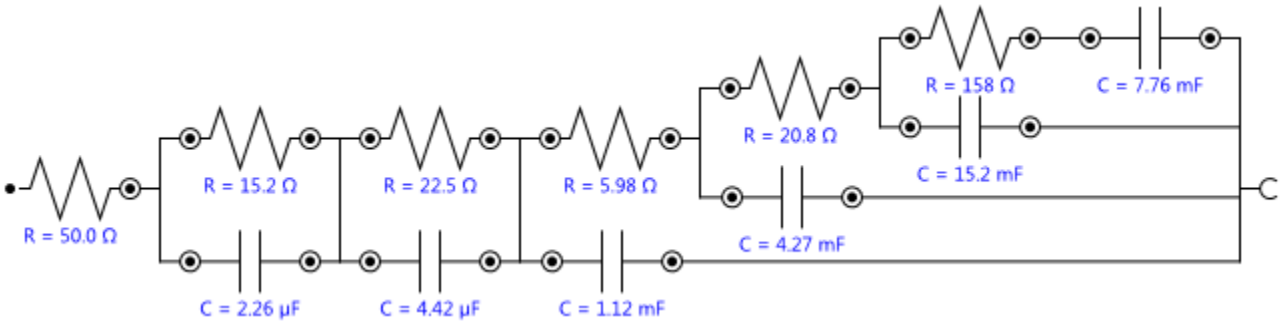

(d) Equivalent circuit for spectrum (b) consisting of five RC elements

Figure 34: Impedance spectrum of npAu prepared by dealloying in $HClO_4$ before and after coarsening. Spectra were recorded at 200 mV with frequencies between 48502 and 0.018 Hz before and with frequencies between 100000 and 0.05 Hz after coarsening. Coarsening was achieved 150°C for 2 hours. The equivalent circuits are presented and the corresponding fits are shown in the spectra.

4.6 Impedance Spectroscopy in Chemically Active Regimes (npAu, npPd)

All impedance spectra presented so far were recorded for samples in the electrochemical double layer regime. In this section spectra taken in different chemical active regimes are investigated. The coarsened nanoporous gold sample B (Fig. 33b) was used for investigating npAu. For the measurements on npPd, a new sample is used. A chronoamperometry-potential-step (current flow measured at constant potential) precedes the EIS measurements. After the current flow stopped, the impedance spectra were measured.

4.6.1 Impedance Spectra and Total Capacitance of npAu in Different Chemical Regimes

Impedance spectra of the npAu sample were taken at five different potentials chosen between −100 and 1100 mV. Therefore a closer look on the cyclic voltammogram, shown in Fig. 35, is necessary to see which reactions take place in this potential window. As already mentioned in Sect. 2.2, nanoporous gold has a very broad double layer region, which spreads from −200 to about 500 mV. The origin of the small anodic peak at about 500 mV, which cannot be assigned to gold, remains unclear at this point. At 900 mV oxygen adsorption starts in the anodic branch, which gets desorbed in the cathodic branch between 1200 and 600 mV.

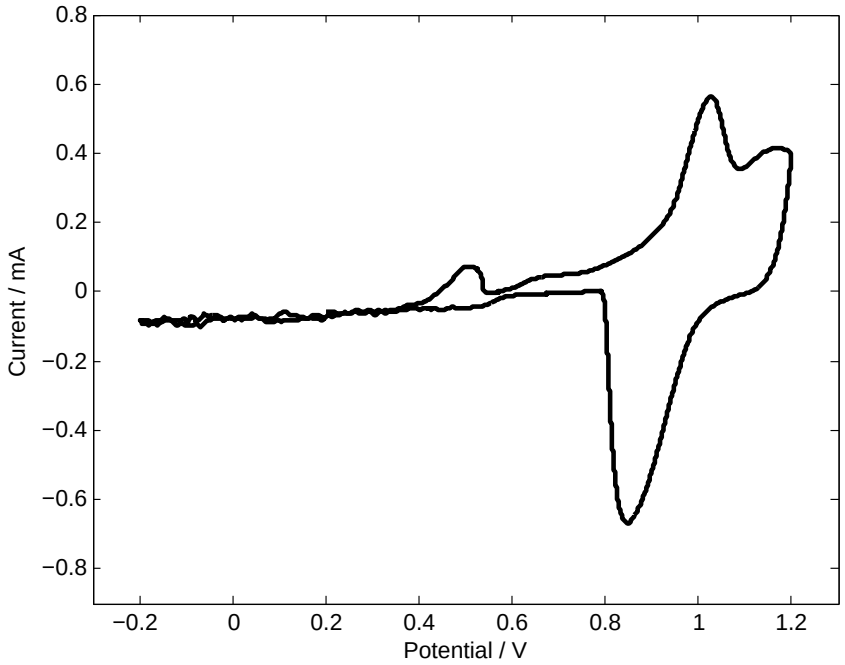

Figure 35: Cyclic voltammogram of npAu aged due to a variety of electrochemical treatments in 10 mM $HClO_4$ with a scan rate of 1 mVs^{-1}.

In Fig. 36, impedance spectra in the double layer region in a potential range between −100 and 300 mV are shown. No electrochemical reactions reactions are expected in this region. The spectra at 300 and 200 mV can hardly be distinguished, the shape of the impedance loci have already described in Sect. 4.5. Upon decreasing the potential, the middle frequency range starts at slightly higher imaginary values, while the shape stays nearly the same. As a consequence, the linear part of the impedance loci starts at higher imaginary values. Furthermore, the sharp bend of the spectra starts at higher frequencies and the increase gets steeper at decreasing potentials. The slope of the low frequency part at −100 mV tends to infinity. Additional to the sharp bend at higher frequencies, more negative imaginary values at a given frequency are observed.

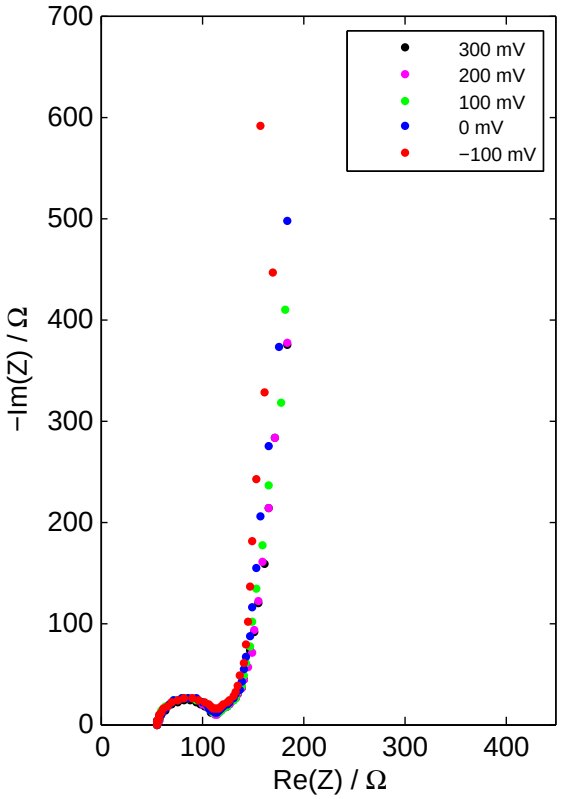

Figure 36: Impedance spectra of npAu with a frequency range of 100000 to 0.02 Hz at potentials between −100 and 300 mV. Sample aged due to a variety of electrochemical treatments.

Fig. 37 shows impedance spectra in the potential range between 400 and 600 mV, which is also in the double layer region. Since no reactions should take place, the shape of the impedance spectra would be expected to look similar as in Fig. 36. However, with increasing potential, the shape changes significantly. The reason for this may be found in the unexpected peak described in cyclic voltammogram (Fig. 35) between 400 and 600 mV. At 600 mV, the impedance loci shows a more semi-circle like behavior in the high frequency range again.

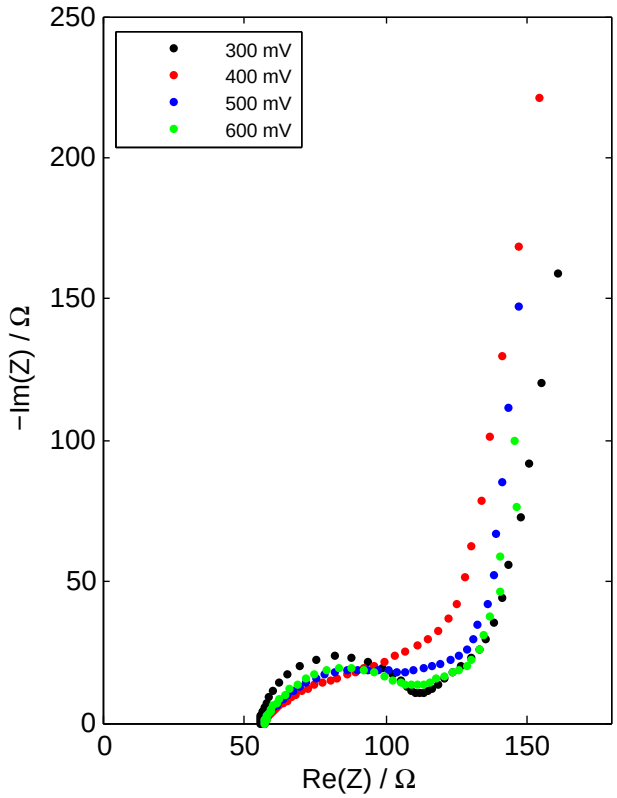

Figure 37: Impedance spectra of npAu with a frequency range of 100000 to 0.05 Hz at potentials between 400 and 600 mV. Sample aged due to a variety of electrochemical treatments.

In the spectra taken at potentials between 700 and 900 mV (Fig. 38), the high frequency range shows a semi-circle like behavior. The shape of the impedance spectra look similar to those in Fig. 36. By increasing the potential, the impedance loci of the high frequency arc tend more towards the real axis. Furthermore the imaginary impedance values at a certain frequency decreases with increasing potential. At 900 mV the very low frequency part deviates from the observed behavior at other potentials and tends more towards the real axis.

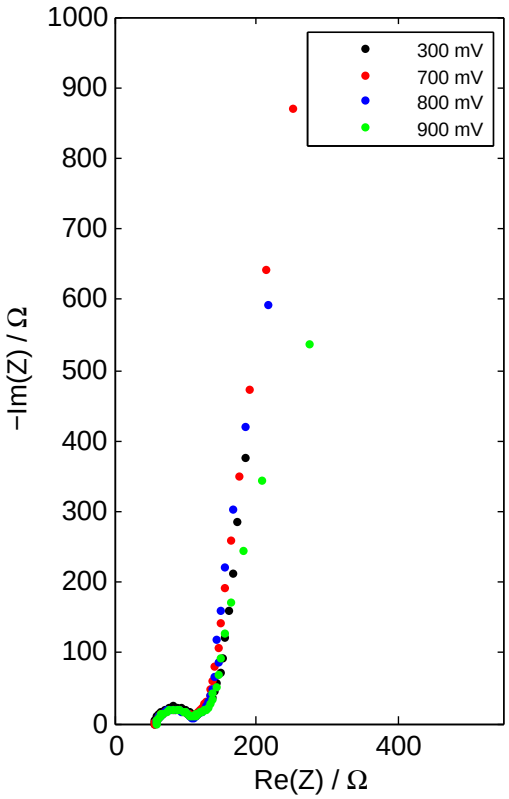

Figure 38: Impedance spectra of npAu recorded at potentials between 700 and 900 mV in a frequency range of 100000 to 0.01 Hz. Sample aged due to a variety of electrochemical treatments. The 300 mV spectrum is measured only to 0.02 Hz.

By increasing the frequency above 900 mV, as shown in Fig. 39, the low frequency region of the spectrum changes significantly. Between 950 and 1000 mV the impedance loci converge to the onset of an additional semicircle. Such a behavior is an indication of charge transfer at the electrode-electrolyte interface[4,16]. In the anodic part of this potential window, oxygen adsorption starts whereas in the cathodic part oxygen desorption occurs. Since the onset potentials of both reactions are close for each other, an amplitude of 10 mV of the ac signal is sufficient to adsorb and desorb oxygen on the electrode surface. This charge transfer can be seen in the Nyquist plot as the onset of an additional semicircle. Above 1000 mV the low frequency part re-approaches the initial behavior.

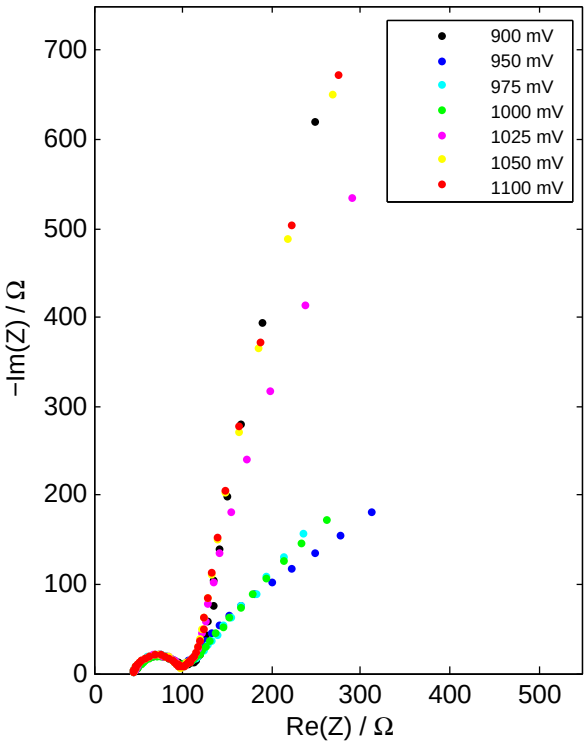

Figure 39: Impedance spectra of npAu in a frequency range of 100000 to 0.01 Hz at potentials between 900 and 1100 mV. Sample aged due to a variety of electrochemical treatments.

The different shapes of the impedance spectra in the high potential region require an adjustment of the corresponding equivalent circuits. Fig. 40 shows the impedance spectrum at 1000 mV and the circuit used for the fit. The high frequency arc is described by the first RQ element, the remaining spectrum by the second RQ element. This second element contains the charge transfer resistance, for which the fit gives a high value with also a high error is very large ($R_{\mathrm{ct}} = (5700 \pm 2900)\ \Omega$). Since for a charge transfer resistance a small value is expected, this resistance value is not very reasonable.

In Fig. 41, the impedance spectrum at 1100 mV is shown. As already described, only the very low frequency part of the spectra in Fig. 41a shows an onset of a charge transfer reaction. The corresponding equivalent circuit in Fig. 41b has almost the same structure as that one used for the fit of the spectrum at 200 mV in Fig. 33d. The only difference is the additional charge transfer resistance parallel to the last capacitance. This resistance is necessary to achieve a suitable quality of the fit. Since only the very low frequency region is affected, a charge transfer resistance of $R_{\mathrm{ct}} = (2900 \pm 200)\ \Omega$ appears reasonable.

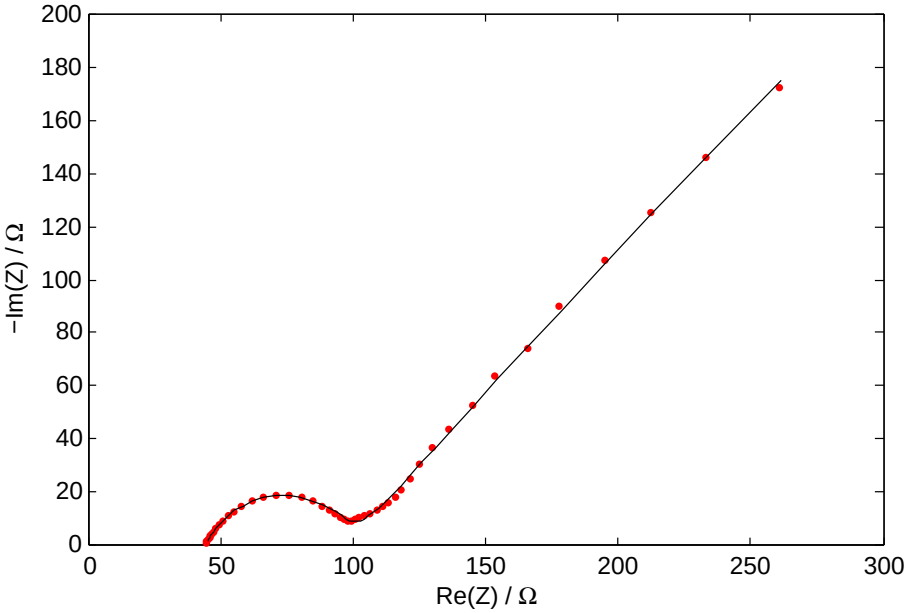

(a) Impedance spectrum and fitted equivalent circuit 40b

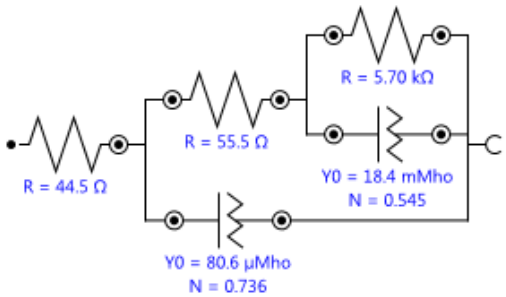

(b) Equivalent circuit consisting of 2 RQ elements

Figure 40: (a) Impedance spectrum of npAu aged by a variety of electrochemical treatments. Spectrum taken at 1000 mV, 100000 - 0.01 Hz. Fitted line corresponds to equivalent circuit in part (b).

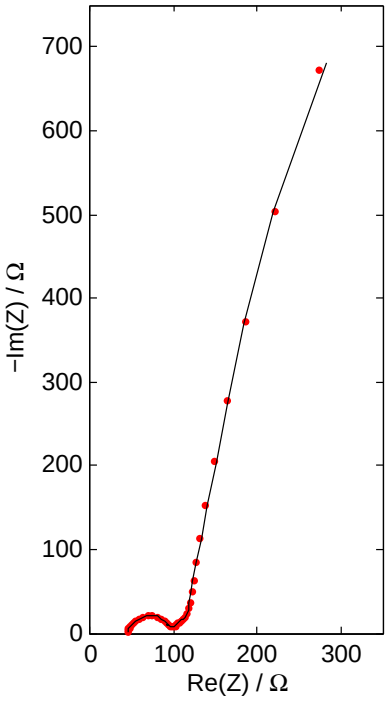

(a) Impedance spectrum and fitted equivalent circuit 41b

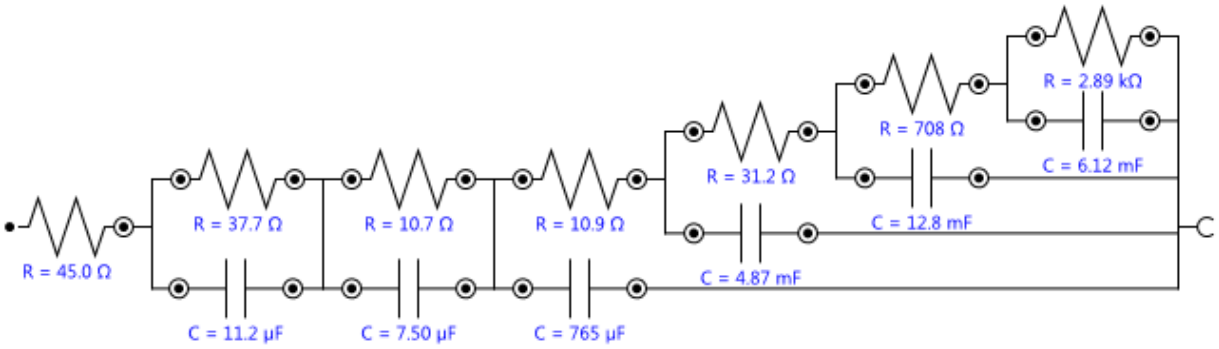

(b) Equivalent circuit consisting of six RC elements

Figure 41: (a) Impedance spectrum of npAu aged by a variety of electrochemical treatments. Spectrum taken at 1100 mV, 100000 - 0.01 Hz. Fitted line corresponds to equivalent circuit in part (b).

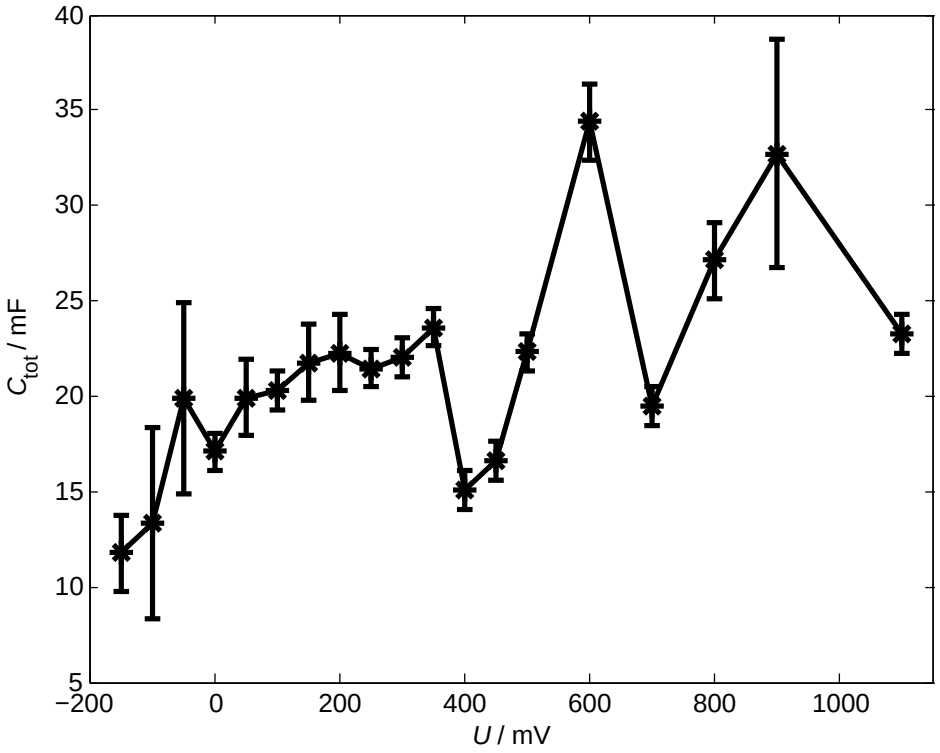

Figure 42: Total capacitance C_{tot} of the npAu sample aged by a variety of electrochemical treatments.

Fig. 42 shows the total capacity of the material in dependence of the applied potential. The total capacitance C_{tot} is deduced from the circuit fitted to each spectrum. C_{tot} increases with increasing potential in the double layer region from −150 to 400 mV. For potentials higher than 400 mV, the values fluctuate. The lower C_{tot} at 400 and 450 mV may reflect the unexpected peak observed in the CV in that potential range. The capacitance value at 1100 mV was calculated via the specific double layer capacitance for gold. At such a potential the surface is covered with oxygen, the use of this conversion factor is not very accurate. Since the variations in the total capacitance are smallest between 50 to 400 mV, impedance spectra should be recorded in that potential window for reasons of reproducibility.

4.6.2 Hydrogen in npPd

As already mentioned in Sect. 2.2, the double layer region nanoporous palladium spreads out from lower than 0 up to about 600 mV, as shown in Fig. 43. At more negative potentials, npPd has the ability to absorb hydrogen. For the impedance measurements of this phenomena, a freshly prepared and already cycled nanoporous electrode is used.

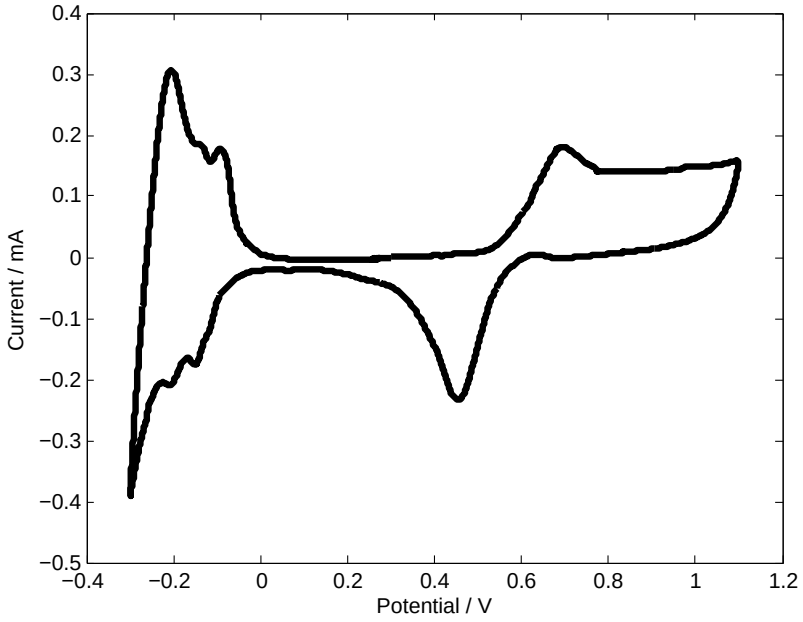

Figure 43: Cyclic voltammogram of npPd in 10 mM $HClO_4$ with a scan rate of 0.1 mVs^{-1}.

Three impedance spectra recorded in the double layer region are shown in Fig. 44a. The difference in the spectra shape between 100 and 150 mV is marginally. They consist of a high frequency arc, a linear behavior at medium frequencies and a steep increase in the low frequency range. In the low frequency branch, the imaginary impedance at a given frequency has a lower value at 100 mV than at 150 mV. Exemplary the impedance spectrum at 150 mV and the corresponding equivalent circuit is shown in Fig. 45. For the total capacitance C_{tot} a value of (15 ± 1) mF and for the pore resistance R_{pore} a value of $(607 \pm 55)\ \Omega$ is obtained. With a specific double layer capacitance between 23.1 and 44.5 $\frac{\mu F}{cm^2}$ [6] and a mass sample m of (12 ± 1) mg, a total surface area A of $(300 - 600)$ cm^2 and a specific surface area α of $(3 - 5)$ $\frac{m^2}{g}$ is obtained.

The high and the middle frequency part of the spectrum at 0 mV is similar to the other two spectra, but at low frequencies the increase in the impedance loci are not so steep. This deviation is an indication for a beginning faradaic (charge transfer) process at lower potentials.

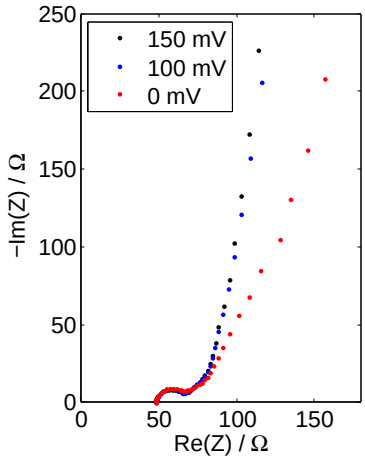

(a) potentials between 150 and 0 mV

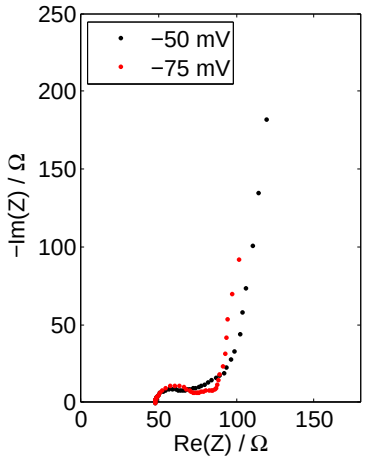

(b) potentials between −50 and −75 mV

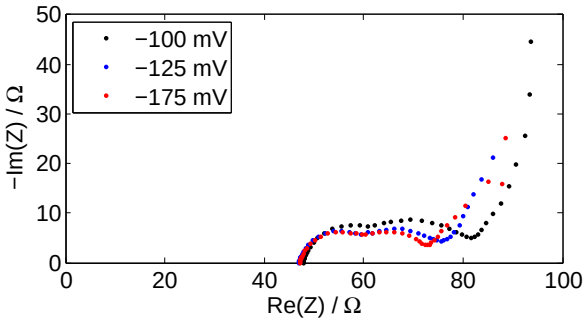

(c) potentials between −100 and −175 mV

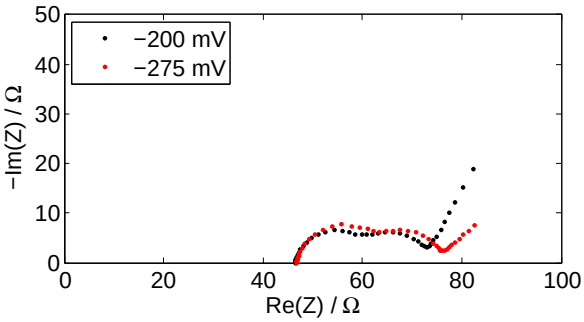

(d) potentials between −200 and −275 mV

Figure 44: Impedance spectra of npPd measured at different potentials between −275 and 150 mV in a frequency range of 100000 to 0.01 Hz.

At negative potentials in the hydrogen region, the shape of the impedance spectra changes significantly. Fig. 44b shows impedance spectra at hydrogen adsorption and absorption starts. The high frequency arc of the spectrum at −50 mV is not changed significantly. In the middle frequency range, the impedance loci show a very flat increase and rise towards high frequencies. At −75 mV the hf semicircle gets bigger. Although the impedance loci show almost a flat behavior in the middle frequency region, an onset for an additional arc can be seen. At low frequencies the usual sharp bend in the loci appears, but at a lower resistance and frequency value compared to higher potentials.

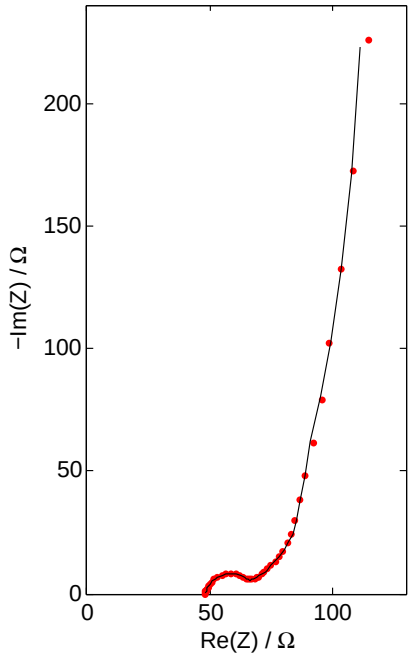

(a) Impedance spectrum at 150 mV

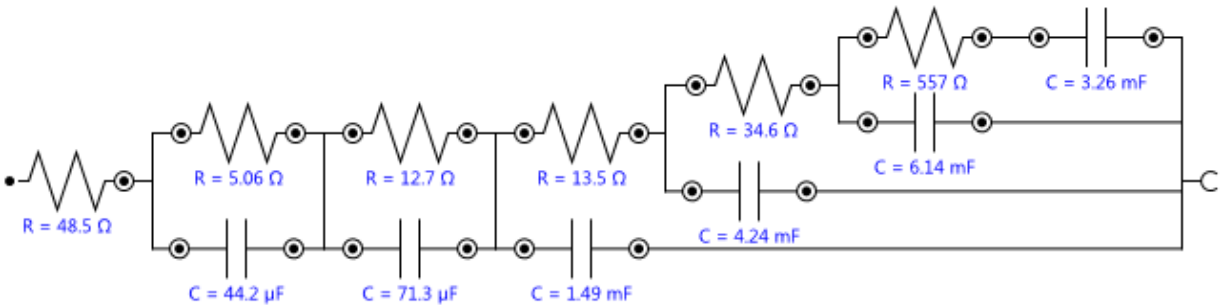

(b) Equivalent circuit consisting of 5 RC elements

Figure 45: (a) Impedance spectrum of npPd recorded at 150 mV (see Fig. 44) with fit according to circuit shown in (b).

By lowering the potential further, an additional arc grows in the middle frequency range, as shown in Fig. 44c. As mentioned already above, the sharp bend at low frequencies tends to lower resistance values with decreasing potential. At −100 mV, the very low frequency region shows a steep increase in the impedance loci. This behavior changes at −125 mV and especially at −175 mV, where this part rises linearly, but at an slighter angle.

By further decreasing the potential, as shown in Fig. 44d, the above described behavior continuous. At −275 mV the straight line shows an onset of a curvature. This is an indication that the hydrogen evolution has started. Since this change from a straight line to an arc is not very noticeable in the spectra, the equivalent circuits help to reinforce this change. The spectra in Fig. 46 are fitted with the same equivalent circuit. The first RQ element is responsible for

the first arc, the second RQ element for the second arc. The low frequency part in Fig. 46a is a straight line and is described by the last element of Fig. 46c. The corresponding resistance is called the hydrogen evolution resistance R_{ev}[4]. R_{ev}, framed red, is very high in this spectrum ($R_{ev} \approx 1.1$ TΩ). The correctness of this value is questionable and its error is enormous, anyhow the high value R_{ev} may indicate that no hydrogen evolution occurs. The reciprocal, R_{ev}^{-1}, is therefore extreme small, and can therefore be neglected in such a spectrum. In Fig. 46b, the low frequency part tends towards an arc. The hydrogen evolution resistance, framed red, in the corresponding equivalent circuit (Fig. 46d) is $R_{ev} = (53 \pm 10)$ Ω. Because of this relative small resistance, a hydrogen evolution reaction is possible and the last RQ element describes the beginning low frequency arc.

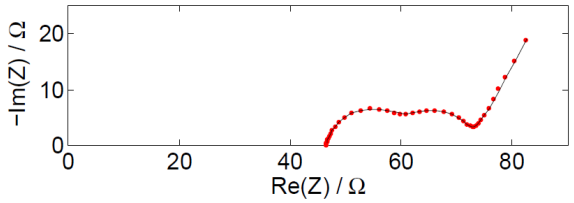

(a) Impedance spectrum at −200 mV

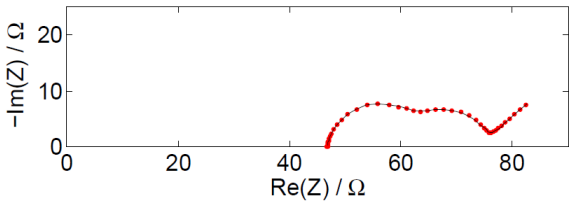

(b) Impedance spectrum at −275 mV

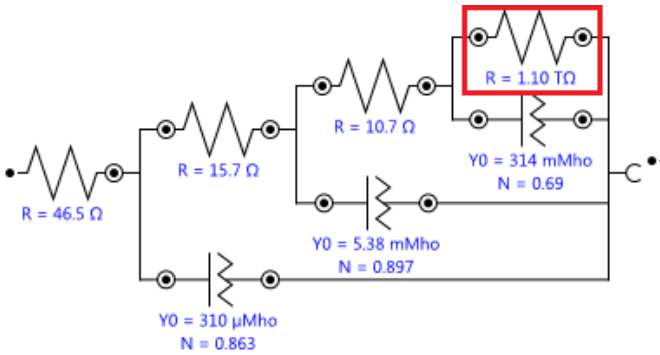

(c) Equivalent circuit of 46a

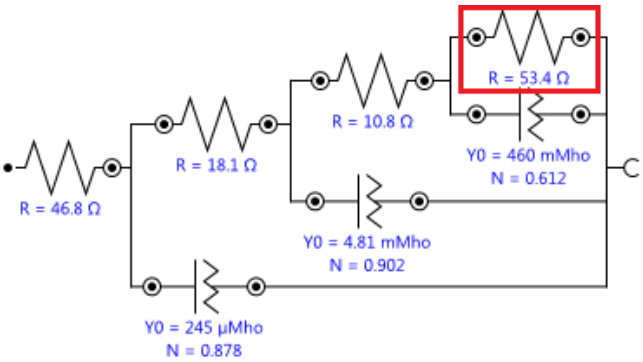

(d) Equivalent circuit of 46b

Figure 46: Impedance spectra of npPd at −200 and −275 mV (see Fig. 44).

The specific surface area α of $(3-5)$ $\frac{m^2}{g}$ of this nanoporous palladium sample is very low compared to literature[26]. A potential explanation would be that during the formation of the $Co_{75}Pd_{25}$ alloy, the tip of the arc melter was in contact with the sample. Therefore, copper could be inhomogeneously incorporated into the alloy. This can have an effect on the performance of the alloy during dealloying. Therefore, this sample is neglected in the further analysis in Sect. 5.

5 Analysis and Discussion

In this chapter the results presented in Sect. 4 are analyzed and further interpretation is given. A sharper focus is laid on the equivalent circuit of the impedance spectrum in Sect. 5.1. The pore structure deduced from the spectrum is discussed in Sect. 5.2.

5.1 Equivalent Circuit of the Entire Spectrum

In the following interpretation of the results concerning the equivalent circuit is presented. In Sect. 5.1.1 and 5.1.2, the particular elements of the circuit are assigned to their physical meaning in the impedance spectrum. From the equivalent circuit the pore resistance and the total capacitance of an electrode can be determined. The received values are compared with the values obtained directly from the spectrum in Sect. 5.1.3 and in Sect. 5.1.4 with values already known from cyclic voltammetry measurements. In Sect. 5.1.5 the final equivalent circuit is shown as a conclusion.

5.1.1 Contact Impedance

In this section further analysis of the high frequency arc is made. Since the majority of measurements have been made with nanoporous gold, these samples are in the focus in this section. The necessary measurement results for the interpretation are taken from Sect. 4.2, 4.3 and 4.4. In Sect. 4.2 and 4.3 the nanoporous sample is connected via a wire to the potentiostat (measurement setup Fig. 15a). Whereas in Sect. 4.4, the unetched part is connected by a clamp to the potentiostat, while the nanoporous part of the sample was immersed in the electrolyte (measurement setup Fig. 15b). These two setups give different impedance spectra.

The samples connected via a wire to the setup show at high frequencies a semicircle like behavior, irrespective of the nanoporous material used (e.g. Fig. 22). Whereas by using the partly etched npAu platelet, the high frequency arc is avoided by choosing only the nanostructured part to be in contact with the electrolyte (Fig. 31). Therefore, an obvious explanation for the appearance of the high frequency arc is the contact impedance Z_{cont}, caused by the connection between the nanoporous electrode and the wire. Z_{cont} consists of the contact resistance R_{cont} and the contact capacitance C_{cont}. An additional contribution to the arc might arise from the connection of the wire to the measurement setup via a clamp.

Z_{cont} is indirectly proportional to the contact area A_{cont}. Since A_{cont} between the electrode and the measurement instrument is much larger in the case of the nanostructure/alloy sample, the contact resistance can be expected to be smaller. Obviously it is so small that no contribution of Z_{cont} is visible in the impedance spectrum in Fig. 31. If also the alloy is in contact with the electrolyte (Fig. 32), the partly etched npAu platelet shows a small arc at high frequencies. Since the unetched alloy influences the spectra, it may be concluded that also the metallic wire,

which is used in the other sample set up in Sect. 4.2 and Sect. 4.3, may cause an additional contribution to the contact impedance.

In Sect. 4.5, coarsened samples are investigated. The contact impedance has increased and the specific surface decreases after coarsening. Since the contact impedance is indirectly proportional to the contact area, Z_{cont} rises because A_{cont} has become smaller.

The circuit elements describing the contact impedance have already been assigned in Sect. 4.2 and 4.3. Exemplary Fig. 22 and 23 are mentioned here. In Fig. 24 the measured high frequency parts of Fig. 22 are compared with the fitted ones of the equivalent circuits shown in Fig. 23. Fig. 24 is very meaningful for evaluating which RC element and how many of them fit this high frequency semicircle. For a better overview, the elements responsible for the contact impedance, as shown e.g. in Fig. 23, are connected in series between the electrolyte resistance and the remaining part of transmission line and are framed green. By increasing the number of elements in the equivalent circuit, the fit improves, as shown e.g. in Fig. 22, and two or more RC elements describe the high frequency arc. The effect of splitting the contact impedance in two components is demonstrated in Fig. 23c and Fig. 23d. In Fig. 23c one RC element describes the high frequency arc, whereas in Fig. 23d two elements are used for the fit of this part of the spectrum. By using more RC element to fit the contact impedance, the fit quality improves and the high frequency arc is better approximated.

The contact impedance is also discussed by Qu et al.[27], where this high frequency arc is interpreted as the result of the connection between a porous hierarchial carbon aerogel monolith electrode and a wire used as current collector. This is a further indication that the high frequency arc in the impedance spectra of the nanoporous metal electrodes is caused by the contact impedance. By applying a contact pressure, Z_{cont} can significantly be reduced. Furthermore to minimize or even prevent this contribution, silver epoxy can be used as a pore-filling conductive adhesive. By using these assumptions for further impedance spectroscopy measurements of the nanoporous metals, Z_{cont} might be reduced. Landesfeind et al.[16] found small contact capacities in the equivalent circuits describing the impedance spectra of a three-electrode Li-ion battery. This is in good agreement with the equivalent circuits in Sect. 4.2, 4.3 and 4.4, where C_{cont} is in the μF range.

In summary, the high frequency arc is caused by the contact of the nanoporous electrode with the wire, which serves as a current collector. This is in good accordance with literature. Further a small contribution to the high frequency arc by contact between the current collector and the measurement instrument as well as by the wire itself is suggested. The high frequency part of the spectrum is therefore caused by the sample/measurement set up and has to be neglected for pore structure analysis.

5.1.2 Transmission Line

In the middle to low frequency part, the spectrum is very sensitive to the chemical state (before or after stripping) and the pore shape. This section deals with the segment of the equivalent circuit which corresponds to the middle and low frequency region. The results obtained especially in Sect. 4.3 are the basis for interpretation in this section.

The pore resistance R_{pore} and the total capacitance C_{tot} are material properties. Independent of the circuit dimensions, their values should stay constant. Therefore it is essential to find an equivalent circuit, which gives the correct values of R_{pore} and C_{tot}. According to Fig. 23 and 28, the calculated total pore resistance increases, as shown in Table 2 and Fig. 47. Although a better accordance of the equivalent circuit with the impedance spectrum is achieved by including more RC elements in the circuit, the fits assign values of the pore resistance with decreasing quality. In contrast to R_{pore}, the total capacitance is independent of the pore geometry, so C_{tot} stays constant even if the number of circuit elements is increased. Therefore not the quality of the fitted equivalent circuit should be taken as criterion, but rather the quality of the obtained R_{pore} and C_{tot} values.

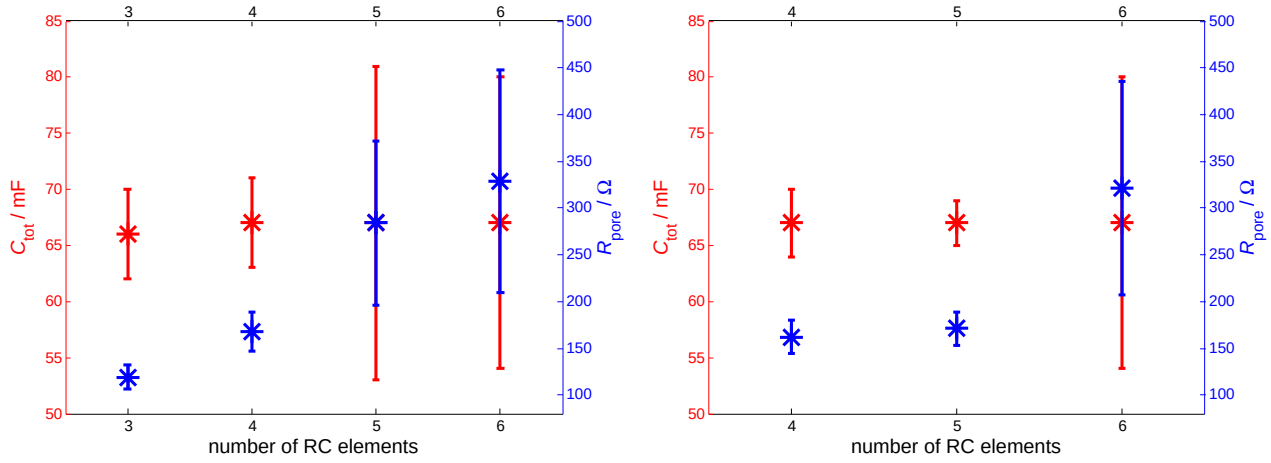

(a) Model after de Levie and Keiser **(b)** Model after Eloot

Figure 47: Values of the total capacitance C_{tot} and the pore resistance R_{pore} of Table 2 plotted as a function of the number of RC elements for the transmission line model after de Levie and Keiser and the model of Eloot.

The equivalent circuit after the model of de Levie[18] and Keiser et al.[19] consists only of the electrolyte resistance, the contact impedance and the transmission line. In contrast, the model after Eloot et al.[22] also considers the material layer impedance as an additional element and therefore one RC element more in the equivalent circuit. Because of this material layer impedance, the equivalent circuit after Eloot needs one more element than the circuit after de Levie and Keiser to gain a transmission line with the same number of RC elements. Since the error of the calculated values scales with the total circuit size, as shown in Fig. 47, a

transmission line in the model after Eloot has a larger error than that of de Levie and Keiser. Therefore the equivalent circuits after de Levie and Keiser should be preferred due to the minor error at the same transmission line size. Within these equivalent circuits, the fitted circuits of Fig. 23 consisting of five and six RC elements have a very large error and the circuit with three RC elements a bad fit quality. Therefore the equivalent circuit consisting of four RC elements, shown in Fig. 23b, is the only circuit with a low pore resistance error and still a good accordance of the fit with the measured spectrum. This equivalent circuit is therefore chosen as the best one for fitting the impedance spectrum of the nanoporous gold sample dealloyed in $HClO_4$ and for calculating the pore resistance and the total capacitance of the electrode.

Equivalent circuits can also be constructed with resistances and constant phase elements. As already mentioned in Sect. 2.4.1, a constant phase element represents a purely capacitive response at the pore surface[28] and can account for geometrical non-idealities such as surface roughness or distributed parameters[29]. In general, it is much more difficult to find an equivalent circuit consisting of CPEs with the desired quality in blocking condition . An additional difficulty in blocking condition is the neglection of the charge transfer resistance parallel to the capacitance. To calculate the corresponding capacitance from the constant phase element, a parallel charge transfer resistance is needed. In contrast, in non-blocking condition a charge transfer at the interface is possible. The interface impedance consists therefore of a parallel-connection of a capacitance or a constant phase element with a charge transfer resistance. The calculation of the capacitance from a CPE is therefore straight forward. As shown, e.g., in Fig. 40 or 46, with few RQ elements the impedance spectra are very well fitted. An equivalent circuit with RC elements would need much more circuit elements to produce a fit with the same quality. In Fig. 41, an onset of charge transfer can be observed at very low frequencies. The equivalent circuit is constructed after the model of de Levie and Keiser in blocking condition, but with an additional charge transfer resistance at the last capacitance. Without this charge transfer resistance R_{ct}, the accordance of the fit with the spectrum would not be achieved. This equivalent circuit is an intermediate state between a blocking and a non-blocking condition.

5.1.3 Fit Quality

By now the total capacitance and the pore resistance have been determined by summation of the particular resistances R_i and capacities C_i of the equivalent circuit. However, R_pore and C_tot can also be deduced from the impedance spectrum itself. A comparison between the values obtained via the equivalent circuit and those obtained directly from the spectrum is made in this section.

Since $C = -\frac{1}{2\pi f Im(Z)}$, the total electrode capacitance C_tot can be estimated by calculating the value $-\frac{1}{2\pi f Im(Z)}$ for each frequency point. The frequency independent plateau value at low frequencies f gives then the value of C_tot [30]. The corresponding plot of the npAu sample described in Sect. 4.3 is shown in Fig. 48. To resolve the entire plateau, the frequency spectrum should have been extended to lower values. So only the onset of the flattening behavior can be seen in the present data. The increasing capacitance towards lower frequencies is caused by the deeper penetration depth of the ac signal into the pore. The low frequency limit of the capacitance in Fig. 48 is about $C = (70 \pm 2)$ mF. This is in good accordance with the total capacitance obtained via the equivalent circuits. For a circuit after de Levie and Keiser with a total number of 4 RC elements $C_\mathrm{tot} = (67 \pm 4)$ mF (Table 2).

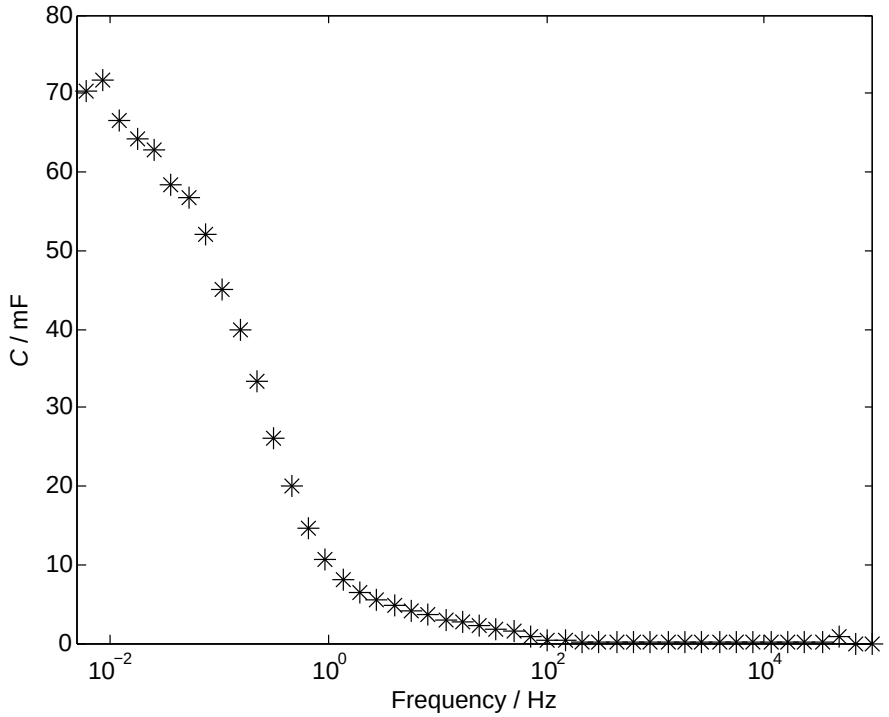

Figure 48: Capacitance of the npAu sample described in Sect. 4.3, Fig. 22, at a certain frequency plotted over frequency.

As already mentioned in the fundamental part 2.4.2, according to the theory of Keiser et al. [19] the sharp bend at low frequencies occurs at $R_\Omega = \frac{R_{\mathrm{pore,s}}}{3}$. $R_{\mathrm{pore,s}}$ is the pore resistance estimated from the impedance spectrum. Whereas following the theory of Eloot et al. [22] the sharp bend appears at $R_\Omega = \Lambda_\mathrm{g} \cdot R_{\mathrm{pore,s}}$ which depends on the pore shape via the geometry constant Λ_g. An estimation for R_{pore} is obtained using $\Lambda_\mathrm{g} = \frac{1}{3}$, which is valid for cylindrical pores. $R_{\mathrm{pore,s}}$ is therefore $3 \cdot R_\Omega$. The value of R_Ω is estimated, as mentioned by Landesfeind et al. [16], by approximating the very low frequency range of the spectrum with a straight. The resistance value of the intersection of this straight minus the electrolyte and the contact resistance gives then R_Ω.

In Fig. 49, the impedance spectrum of the nanoporous gold sample of Sect. 4.3 (Fig. 22) is shown along with two straight lines inserted in the plot, following Landesfeind et al. [16]. The line in Fig. 49 with a smaller slope neglects the contribution of the electrolyte resistance and the contact impedance and approximates the first increase in the impedance loci of the transmission line. The second line represents the slope of the spectrum at very low frequencies. Since the spectrum does not show a abrupt bend, the straight line at low frequencies is not unambiguously defined.

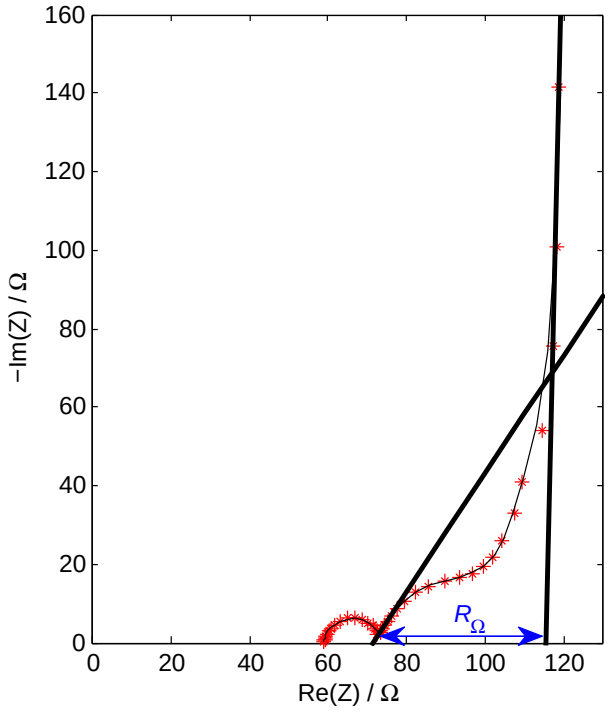

Figure 49: Determination of R_Ω from the impedance spectrum of a npAu sample of Sect. 4.3, Fig. 22, in the Nyquist plot representation.

The linear equations obtained via these two lines are:

$$g_1(r) = 1.5 \cdot r - 108, \tag{38}$$

$$g_2(r) = 47 \cdot r - 5418. \tag{39}$$

The corresponding intersections with the x-axis are $r_1 = 71\ \Omega$ and $r_2 = 116\ \Omega$. As reading error $\pm 5\ \Omega$ is assumed for r_1 and r_2. Following the method of Landesfeind et al.[16] R_Ω is then the difference between these two resistance values:

$$R_\Omega = (45 \pm 10)\ \Omega.$$

After the model of Keiser et al.[19], the pore resistance determined via the impedance spectrum is three times the value of R_Ω:

$$R_{\text{pore,s}} = 3 \cdot R_\Omega = (135 \pm 30)\ \Omega.$$

As discussed in Sect. 5.1.2, the equivalent circuit after the model of de Levie and Keiser consisting of four RC elements is chosen for fitting the spectrum. The calculated pore resistance of the circuit is $R_{\text{pore,c}} = (168 \pm 21)\ \Omega$. Taking into account the uncertainties, this value is consistent with that derived from R_Ω ($R_{\text{pore,s}} = (135 \pm 30)\ \Omega$).

The geometry constant can be defined as the ratio between the experimentally estimated R_Ω and the pore resistance calculated from the equivalent circuits. With $R_\Omega = (45 \pm 10)\ \Omega$ and $R_{\text{pore,c}} = (168 \pm 21)\ \Omega$, the geometry constant is:

$$\Lambda_{\text{g}} = 0.27 \pm 0.09.$$

For the nanoporous palladium sample of Sect. 4.3 (Fig. 30a), R_Ω has been determined from Fig. 50. The corresponding linear equations read:

$$g_1(r) = 0.4 \cdot r - 37, \tag{40}$$

$$g_2(r) = 12.4 \cdot r - 2495. \tag{41}$$

The resulting intersections with the x-axis are $r_1 = 90\ \Omega$ and $r_2 = 201\ \Omega$. Again as reading error $\pm 5\ \Omega$ is assumed for r_1 and r_2.

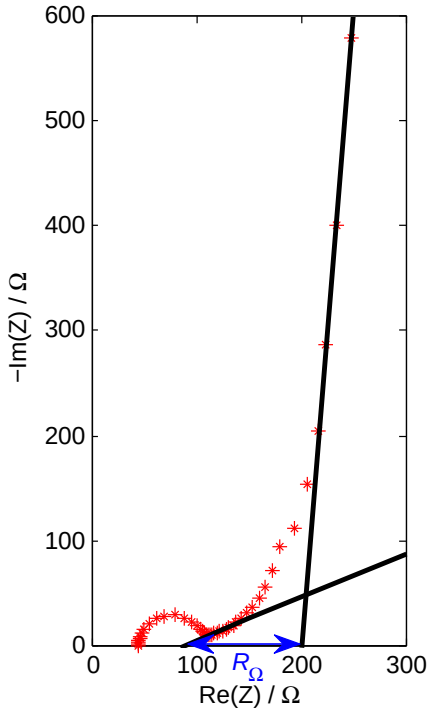

Figure 50: Determination of R_Ω from the impedance spectrum of a npPd sample of Sect. 4.3 in the Nyquist plot representation.

The values of R_Ω and $R_{\text{pore,s}}$ can therefore be estimated as:

$$R_\Omega = (111 \pm 10)\ \Omega,$$

$$R_{\text{pore,s}} = 3 \cdot R_\Omega = (333 \pm 30)\ \Omega.$$

This value is smaller than that calculated from the equivalent circuit, which is $R_{\text{pore,c}} = (457 \pm 53)\ \Omega$. The geometry factor deduced from $R_{\text{pore,c}}$ and R_Ω is:

$$\Lambda_{\text{g}} = 0.24 \pm 0.05.$$

For the sake of completeness, Table 7 summarizes the experimentally determined pore resistance and the geometry constants of the other npAu sample dealloyed in H_2SO_4 (Sect. 4.5, Fig. 33a) and the coarsened nanoporous gold samples (33b and 34b).

Since for the npAu 1 sample the values of $R_{\mathrm{pore,s}}$ and $R_{\mathrm{pore,c}}$ are for unknown reasons far apart, the geometry constant is fairly low. The large uncertainty of $\Delta\Lambda_{\mathrm{g}}$ is caused by the relatively large errors of R_{Ω} and $R_{\mathrm{pore,c}}$. By comparing the values of the coarsened nanoporous gold samples with the initial nanoporous samples (Table 7), the pore resistance decreased and the geometry constant increased due to coarsening.

Since for the npAu 2 sample the best equivalent circuit is found to consists of four RC elements (Sect. 5.1.2), for the calculation of the pore resistance of the coarsened npAu 2 sample an equivalent circuit consisting also of four RC elements is used. This is justified by the fact, that the pore resistance changes significantly with the equivalent circuit size. Therefore, the R_{pore}-value in Table 7 differs from that one in Table 5, where an equivalent circuit consisting of five RC elements was used.

Table 7: Experimentally determined pore resistance $R_{\mathrm{pore,s}}$, calculated pore resistance of the transmission line $R_{\mathrm{pore,c}}$ and the geometry constant Λ_{g} with their uncertainties $\Delta R_{\mathrm{pore,s}}$, $\Delta R_{\mathrm{pore,c}}$ and $\Delta\Lambda_{\mathrm{g}}$. Data for $R_{\mathrm{pore,c}}$ are taken from Table 2, 4 and 5. In contrast to Sect. 4.5, for the npAu 2 (c) sample, an equivalent circuit consisting only of four RC elements is used.
npAu 1: nanoporous gold sample dealloyed in $HClO_4$; npAu 1 (c): npAu 1 sample aged due to a variety of electrohemical treatments; npAu 2: nanoporous gold sample dealloyed in H_2SO_4; npAu 2 (c): npAu 2 sample coarsened at 150°C for 2 h; npPd: nanoporous palladium sample dealloyed in H_2SO_4 (Fig. 30a);

sample	$\boldsymbol{R_{\mathrm{pore,c}}}$ / **Ω**	**Δ** $\boldsymbol{R_{\mathrm{pore,c}}}$ / **Ω**	$\boldsymbol{R_{\mathrm{pore,s}}}$ / **Ω**	**Δ** $\boldsymbol{R_{\mathrm{pore,s}}}$ / **Ω**	$\boldsymbol{\Lambda_{\mathrm{g}}}$	$\boldsymbol{\Delta\Lambda_{\mathrm{g}}}$
npAu 1	4000	1000	210	30	0.02	0.01
npAu 1 (c)	1300	330	75	30	0.06	0.02
npAu 2	168	21	135	30	0.27	0.09
npAu 2 (c)	135	18	96	30	0.71	0.17
npPd	457	53	333	30	0.24	0.05

To summarize these findings, only for the npAu 1 and the coarsened npAu 1 sample the pore resistance calculated from the different equivalent circuits matches the resistance value determined by the impedance spectrum within the given uncertainties. For all other samples, the $R_{\mathrm{pore,s}}$ and $R_{\mathrm{pore,c}}$ values are far apart. Concerning the calculation of the pore resistance, one has to remark that the resistance value determined via the impedance spectrum is obtained with three times R_{Ω}, i.e., with a given geometry factor which has to be taking into account for assessing R_{pore}. In fact, however, the geometry factor is not known.

5.1.4 Specific Surface Area

In this section the obtained total capacitance values from electrochemical impedance spectroscopy measurements are compared with results known from cyclic voltammetry (CV) measurements. Both, CV and EIS, measure a differential capacitance $C_{\text{diff}} = \frac{dq}{d(\psi_S)}$. q denotes the electric charge, ψ_S the electrode potential, i.e. the electric potential difference between the electrode surface and the electrode bulk of the electrolyte[31]. The results of the two methods might deviate from each other. Broadband EIS spectra resolve different processes taking place on different time scales. In cyclic voltammetry measurements, a much smaller time window, determined by the scan rate variation, is used. Discrepancies might be caused by faradaic reactions at the electrode/electrolyte interface and electrode-surface inhomogeneities. To obtain the same amount of information with CV measurements as via EIS, the scan rate has to varied over several orders of magnitude[31,32].

Since the obtained capacitance depends also on the sample mass, the specific surface area α (Eq. (36)) is used for comparison. For this purpose, the total surface area A has to be estimated, which is calculated via the specific double layer capacitance C_{dl} (Eq. (30)), which depends very sensitively on the electrolyte concentration[33]. For npAu in 10 mM $HClO_4$, C_{dl} lies between 20 and 30 $\frac{\mu F}{cm^2}$[30,33]. For nanoporous palladium in $HClO_4$ such a conversion factor was not found in the literature. Although the interactions between palladium and ClO_4^- are weaker than with HSO_4^-/SO_4^{2-}[5], as a rough approximation the specific double layer capacitance of palladium in sulfuric acid was used, which was reported to be between 23.1 and 44.5 $\frac{\mu F}{cm^2}$[6]. Since a variety of different specific double layer capacities is found in literature a large and a small C_{dl} value is taken as a conversion factor and used for error estimation. In Table 8, the specific surface areas already calculated in Table 3 and 6 and Sect. 4.3.6 are listed for comparison.

Table 8: Total surface area A, sample mass m with uncertainty Δm and specific surface area α taken from Tables 3 and 6 and Sect. 4.3.6.
npAu 1: nanoporous gold sample dealloyed in H_2SO_4 (Fig. 33a); npAu 1 (c): npAu 1 sample aged due to a variety of electrochemical treatments (Fig. 33b); npAu 2: nanoporous gold sample dealloyed in $HClO_4$ (Fig. 22); npAu 2 (c): npAu 2 sample coarsened at 150°C for 2 h (Fig. 34b); npPd: nanoporous palladium sample dealloyed in H_2SO_4 (Fig. 30a).

sample	$\boldsymbol{A}$ / $\mathbf{cm^2}$	$\boldsymbol{m}$ / **mg**	$\boldsymbol{\Delta m}$ / **mg**	$\boldsymbol{\alpha}$ / $\mathbf{m^2 g^{-1}}$
npAu 1	1200 – 1800	12	1	10 – 15
npAu 1 (c)	700 – 1100	12	1	6 – 9
npAu 2	2200 – 3400	25	1	9 – 14
npAu 2 (c)	900 – 1400	25	1	4 – 6
npPd	6400 – 12400	12	1	53 – 103

The npAu 2 sample (Table 8) has also been investigated by double layer cyclic voltammetry measurements. With this steady state method a specific surface area α of approximately 10 $\frac{m^2}{g}$ was found by E. Hengge[34]. These cyclic voltammetry measurements have been performed in 1 M $HClO_4$, a potential window between −100 and 300 mV and with scan rates of 5, 10, 15, 20, 25 and 30 mVs^{-1}. The CV measurement value is in very good agreement with the corresponding value obtained from EIS measurements ($\alpha = (9 - 14)\ \frac{m^2}{g}$).

Although two different electrolytes are used for the electrochemical dealloying process, the calculated values of the specific surface area of the nanoporous gold electrodes (Table 8) are very similar. Cattarin et al.[30] found a specific surface area between 10 and 15 $\frac{m^2}{g}$, which is in very good agreement with the values found by EIS measurements for the npAu 1 and npAu 2 sample.

As shown in Table 8, the specific surface area α decreases due to coarsening. The specific surface area of the npAu 1 sample, which was aged due to a variety of electrochemical treatments at ambient temperatures, changed not as much as α of the npAu 2 sample, which is coarsened at 150°C for 2 h. Since temperature plays a major role during the coarsening process of porous samples, this finding is in good agreement with literature[25]. But as found by investigating the npAu 1 sample, also electrochemical treatments can affect changes in the specific surface area and therefore in the capacitance.

For npPd a specific surface area α of about 30 $\frac{m^2}{g}$ was estimated by Steyskal et al.[26]. In this publication, α was determined via CV double layer measurements in sulfuric acid of nanoporous palladium electrodes, produced by electrochemical dealloying a $Co_{75}Pd_{25}$ alloy similar as used for the EIS investigations in the present work.

The specific surface area for nanoporous palladium has also been estimated with the CV method in H_2SO_4 as electrolyte solution in this Master Thesis. As already mentioned, for H_2SO_4 the specific double layer capacitance is known. The specific surface area obtained via double layer capacitance measurements and Eq. (30) and (36) is about 26 $\frac{m^2}{g}$. This value is in good agreement with the results of Steyskal et al.[26]. Since the specific double layer capacitance of palladium in $HClO_4$ is approximated by the value of palladium in H_2SO_4, the deviating value of α of the npPd sample must originate from the approximation of this specific double layer capacitance.

Since ClO_4^- does not undergo a specific adsorption on palladium, in contrast to HSO_4^-/SO_4^{2-} ions, the anion experiences weak electrostatic interaction with the surface, which gives rise to physisorption, only[5]. As a hypothesis, this weaker interaction of ClO_4^- with the electrode surface has to cause a different specific double layer capacitance compared to HSO_4^-/SO_4^{2-} ions.

5.1.5 Concluding Remarks on Equivalent Circuits

In this section the knowledge gain on the impedance spectra of nanoporous metals and the corresponding equivalent circuits is discussed. In Fig. 51 a typical impedance spectrum obtained from nanoporous gold is presented. With the equivalent circuit shown in Fig. 52, the spectrum can be fitted. The first part (I.) belongs to the electrolyte resistance R_{e}, the second (II.) one to the contact impedance, and the third one to the transmission line fitting the middle and low frequency range of the spectrum. In Sect. 4.6.1, investigations concerning the dependence of the shape of the impedance spectrum on the potential were made. As shown in Fig. 42, the total capacitance in the medium range of the double layer region is almost independent of the applied potential. Therefore impedance spectra without charge transfer should be recorded in such a potential range.

Based on experiments with two different sample setups (shown in Sect. 4.2, 4.3 and 4.4) the high frequency arc, which occurs independently of the sample material, is assigned to the contact impedance Z_{cont}. Z_{cont} is a result of the connection between the nanoporous sample and the wire which serves as current collector, as discussed in Sect. 5.1.1. The middle and low frequency part of the impedance spectrum is fitted by the transmission line. Equivalent circuits after the model of de Levie and Keiser, constructed of RC elements, turned out to be the best choice. As discussed in Sect. 5.1.2, the total capacitance C_{tot} is independent of the circuit dimensions, whereas the pore resistance rises with the number of RC elements. The quality of the fitted spectrum does not improve significantly by increasing the circuit size. Since the uncertainties of C_{tot} and R_{pore} depend on the circuit dimension, it is advantageous to include not more elements than needed for the desired fit quality. In general, impedance spectra in non-blocking conditions are better fitted by equivalent circuits consisting of constant phase elements.

Only the third region of the spectrum reflects the pore shape. For the calculation of the pore raidus (Eq. (33)), the pore length (Eq. (34)) and the number of pores (Eq. (35)) the total capacitance C_{tot} is calculated from the equivalent circuit. Since not the whole pore resistance is needed for the calculation of l_{pore}, but only R_{Ω} , this resistance value is estimated geometrically from the spectrum.

For the nanoporous gold sample, investigated in Sect. 4.3, the ideal equivalent circuit is that one shown in Fig. 23b. Constructed of 4 RC elements, the equivalent circuit has the desired fit quality in combination with low errors of the circuit elements. Z_{cont} consists of one resistance and one capacitance, the transmission line is built up by three RC elements. Furthermore the experimentally determined pore resistance and that one calculated from the equivalent circuit matches within the given uncertainties. The calculated geometry constant is $\Lambda_{\mathrm{g}} = 0.27 \pm 0.09$.

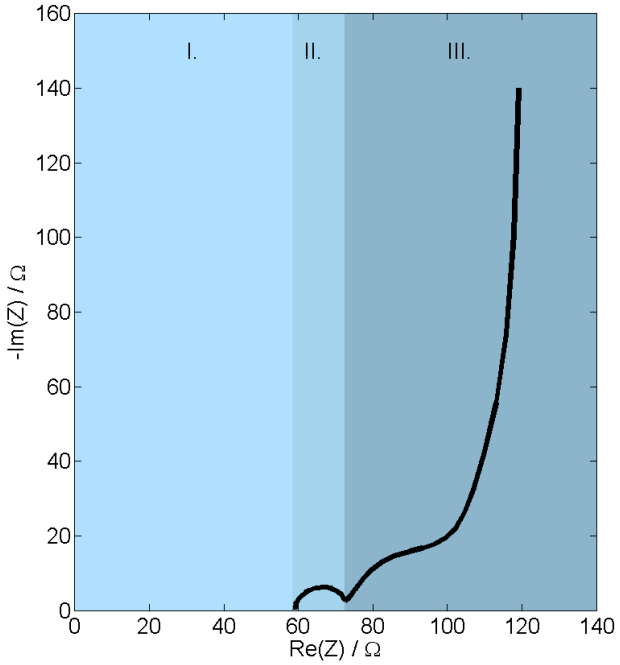

Figure 51: Impedance spectrum of one of the nanoporous samples used in this master thesis. Region I. represents the electrolyte resistance R_{e}, region II. to the contact impedance Z_{cont} and region III. to the transmission line impedance $\frac{Z_{\mathrm{pore}}}{n}$. The corresponding equivalent circuit is shown in Fig. 52.

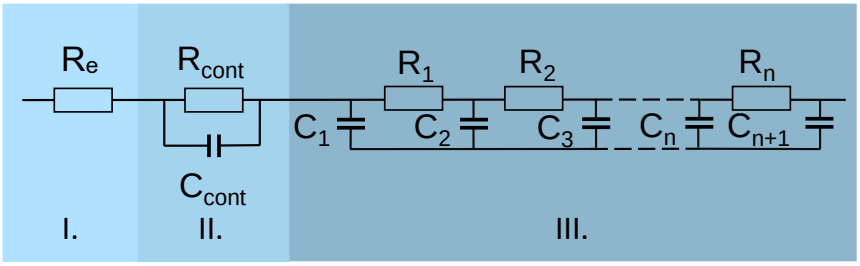

Figure 52: Equivalent circuit of the nanoporous samples used in this master thesis. Region I. corresponds to the electrolyte resistance R_{e}, region II. to the contact impedance Z_{cont} and region III. to the transmission line impedance $\frac{Z_{\mathrm{pore}}}{n}$. The corresponding impedance spectrum is shown in Fig. 51.

5.2 Pore Structure Analysis at Low Frequencies

As outlined in Sect. 5.1.2, the middle and low frequency part of the spectrum is very sensitive to the nanoporous material, the chemical state (before or after stripping or coarsening) and the pore shape. For fitting this part, a transmission line is used. In this section the focus will be on the estimation of the pore shape via the impedance spectrum and the calculation of the pore radius, the pore length and the number of pores. To do so, the high frequency arc is neglected in the analysis, but is still plotted in the figures (e.g. Fig. 53).

5.2.1 Pore Shape

In the model after Keiser et al.[19] and Eloot et al.[22], the pore geometry is considered in the impedance calculations. These models have already been presented in Sect. 2.4.2. Keisers model is very simple and considers only the capacitance at the pore walls and the electrolyte resistance in the pores, called the pore resistance. In the model after Eloot more parameters, such as a non-negligible electrode impedance, are considered. Therefore, a more detailed analysis is possible. These two theories describe ideal porous systems, where the pores are arranged parallel to each other and no crossing of the pores occurs. Since dealloyed metals have a very complex, sponge-like geometry, the theories give only a rough estimation of the pore shape.

To determine the **pore shape after Keiser et al.[19]**, one compares the shape of the measured impedance spectra with those given in Fig. 12. In this theory, the impedance loci of each spectrum commences with a phase angle of 45°, then it deviates from a linear slope and finally rises vertically at low frequencies. The sharp bend in the spectrum occurs at exactly one third of the pore resistance. In Fig. 53, impedance spectra of the four different nanoporous samples are shown, which have been investigated and discussed in the previous sections. The pore shape can be estimated by comparing the impedance curves following the theory of Keiser (Fig. 12) with the spectrum of the nanoporous metal electrode. Although the impedance spectra of the nanoporous gold samples dealloyed in H_2SO_4 and $HClO_4$ look quite similar, that one dealloyed in 1 M H_2SO_4 (Fig. 53a), labeled as npAu sample 1, has a quasi-spherical pore shape (Fig. 12, number **4**). In contrast, that one dealloyed in 1 M $HClO_4$ (Fig. 53b), labeled as npAu sample 2, has a rhombohedral shape (Fig. 12, number **3**). The npPd sample (Fig. 53c) cannot unambiguously be attributed to one of the pore shape curves in Fig. 12. This sample shows a commencing increase in the impedance loci of about 22.5°, whereas all calculated pore shapes of Keiser have an increase of exactly 45° at the beginning. So in the case of the first npPd sample, this theory cannot give an estimation of the pore shape.

To improve the determination of the **pore shape**, the **model after Eloot et al.** [22] is used. In this theory, the sharp bend in the spectrum appears at $\Lambda_g \cdot R_{pore}$. The geometry factor Λ_g depends directly on the pore shape. Further the increase in the impedance loci at high frequencies can deviate from a 45° phase angle. To estimate the pore shape, the impedance spectra have to be compared with Fig. 13, as described in the following.

The **npAu sample dealloyed in 1 M H_2SO_4** (Fig. 53a) has a commencing slope of about 50°. As mentioned in the fundamental part (Sect. 2.4.2, Fig. 13), a phase angle larger than 45° (pore shape and pore shape curves **a** and **b**) is an indication of a conical pore shape. At lower frequencies the impedance loci tend towards the real axis. In comparison with Fig. 13, the pore shape corresponds to curve **e**, this points to a rhombohedral pore shape. Based on these observations, it is suggested that the radius of the pore mouth is slightly bigger than the radius deep inside the pore and the pores have a rhombohedral pore shape. The model of Keiser and Eloot have in common, that the pores have a convex shape. After Keiser the pores have a quasi cylindrical pore shape, after Eloot a more rhombohedral shape is assumed. A R_Ω-value of $70 \pm 10\ \Omega$ and a geometry constant of $\Lambda_g = 0.02 \pm 0.01$ have been estimated in Sect. 5.1.3, Table 7. For such a pore shape, the value of the geometry constant is expected to be significantly higher, approximately between a value of 0.2 and 0.45 (as shown in Fig. 13). Since Λ_g is calculated by the ratio of the experimentally determined R_Ω-value and the calculated pore resistance, this leads to the assumption that R_{pore} determined via the equivalent circuit is far too high.

The spectrum of the **npAu sample dealloyed in 1 M $HClO_4$** (Fig. 53b), shows a slope of approximately 56° at the beginning of the middle frequency range. Subsequently, the increase in the impedance loci stagnates in the commencing low frequency part. By comparing Fig. 53b with Fig. 13, a rhombohedral shape is estimated. By combining these observations, a rhombohedral pore shape is estimated, where the pore mouth has a larger radius than the pore base. Therefore the model after Keiser and Eloot provide a similar result. The geometry constant, estimated in Sect. 5.1.3, Table 7, is $\Lambda_g = 0.27 \pm 0.09$.

Since for the formation of the two nanoporous gold samples different electrolytes are used, the effect of the electrolytes on the pore shape can be compared. Although the impedance spectra deviate from each other, a rhombohedral pore shape is estimated for both nanoporous samples independent of the electrolyte (H_2SO_4 or $HClO_4$). One possible hypothesis for the different impedance spectra shape might be the different period of time needed for the dealloying process. Since in $HClO_4$ the formation of the nanoporous structure is faster than in H_2SO_4, on the one hand the sample gets much more oxidized and hinders the motion of the noble atoms from the bulk to the outer ligament area. On the other hand, the interfacial diffusion is truncated by the limited timescale needed for dealloying. So with H_2SO_4 as electrolyte, more remaining noble atoms accumulate on the macroscopic outer surface area and therefore narrow the pore entrance.

The impedance spectrum of the **nanoporous palladium sample** (Fig. 53c) has two phase angles in the middle frequency part. It starts with a phase angle of about 22.5° and changes than to about 60°. By comparing this behavior with Fig. 13, the most similar shape is the impedance spectrum with the label **c**. Therefore the pore have a deltoid like shape. A geometry factor of $\Lambda_g = 0.24 \pm 0.05$ is an additional indication for such a shape. By using the model after Eloot et al. [22], the pore shape of this nanoporous sample can be estimated.

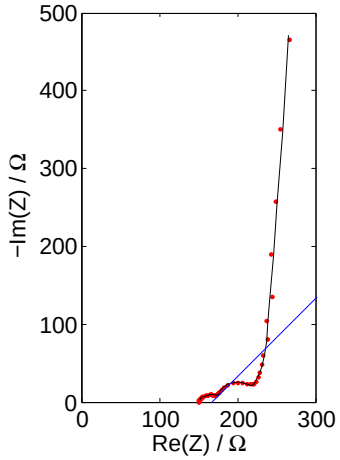

(a) npAu sample 1, dealloyed in H_2SO_4, data from Fig. 33a.

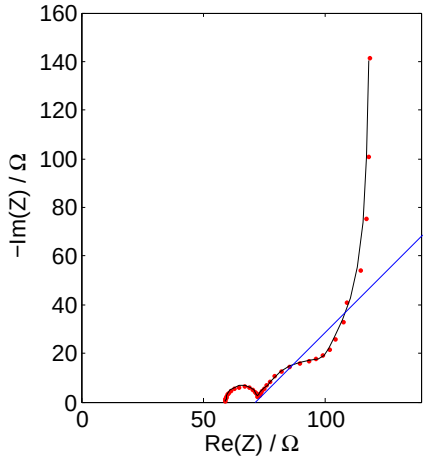

(b) npAu sample 2, dealloyed in $HClO_4$, data from Fig. 22.

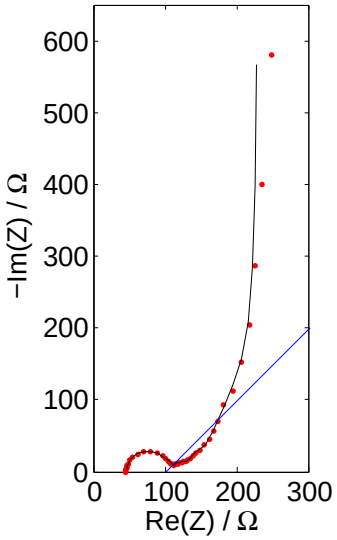

(c) npPd sample, data from Fig. 30a.

Figure 53: Impedance spectra of npAu and npPd samples, data taken from Fig. 22, 30a and 33a. Blue straight with 45° slope for comparison with the phase angle in the middle frequency range.

In Fig. 54, the **coarsened nanoporous gold samples** are shown once again. As already mentioned in Sect. 4.5, the shape of the spectra changes after coarsening. By analyzing the spectra after the model of Keiser, both samples have more or less a cylindrical pore shape. The same finding is obtained by the model of Eloot. The sample aged due to a variety of electrochemical treatments at ambient conditions (Fig. 54a) has a phase angle of about 43°, which does not change over the whole middle frequency range. In contrast, the phase angle of the sample coarsened at 150°C for 2 h (Fig. 54b) is about 48°, and the shape of the spectrum has a slight bending in the middle frequency range.

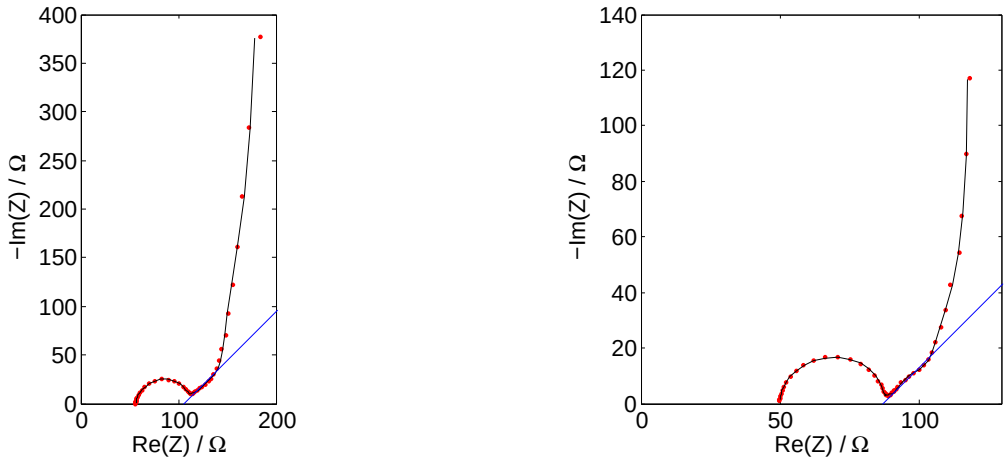

(a) npAu sample 1, coarsened due to a variety of electrochemical treatments, data from Fig. 33b.

(b) npAu sample 2, coarsened at 150°C for 2 h, data from Fig. 34b.

Figure 54: Impedance spectra of coarsened npAu samples, data taken from Fig. 33b and 34b. Blue straight with 45° slope for comparison with the phase angle in the middle frequency range.

5.2.2 Pore Size Distribution

The models after de Levie, Keiser and Eloot have in common that the phase angle approaches 90° at low frequencies. This results in a vertical line in the Nyquist plot, as shown e.g. in Fig. 12. A deviation from a phase angle of 90° is a result of a pore size distribution. Many impedance spectra of porous materials show a deviation from such a 90° phase angle, even at very low frequencies[35]. Also the investigated samples in Fig. 53 show such a behavior. Since such a deviation from the theoretical predicted shape is a common result, Song et al. [35,36] includes in their model a pore size distribution to describe the inclined line of impedance at low frequencies.

By looking at the spectra of the nanoporous samples, the npAu dealloyed in $HClO_4$ and the npPd sample 1 show only at very low frequencies an almost vertical line. Although a phase angle of 90° is reached, the spectra seem to be smeared out in the low frequency range and no abrupt transition to an increase in the impedance with a phase angle of 90° is observed.

This is also an indication for a pore size distribution [35,36]. The low frequency part of the npAu sample dealloyed in H_2SO_4 has a slope of about 86° and reaches the vertical line only at very low frequencies. The slopes are obtained by fitting the last few data points in the spectrum and are, therefore, only a rough estimation. A larger divergence of the low frequency straight line from the vertical implies a greater distribution.

The low frequency part of the coarsend npAu 1 sample shown in Fig. 54a has a slope of about 85°, the coarsened npAu 2 sample in Fig. 54b a slope of 87°. Both samples therefore have a certain pore size distribution and do not reach the purely capacitive behavior with a phase angle of 90°. Since the low frequency phase angles change from 90° to 87° and from 86° to 85°, the pore size distribution has increased after coarsening. Such a behavior is in conflict with literature, where Kelly et al. [25] found an decrease in the pore size distribution after coarsening. The reason for the increase of the pore size distribution after coarsening for the samples in Fig. 54 is unknown.

A pore size distribution can also be identified by analyzing the equivalent circuits of the fitted spectra. The resistance values of the circuits, for example in Fig. 23, increase from the first to the last element. This is an indication that the pores do not have an uniform size, but rather a size distribution. R_i and C_i can be considered as the resistance and the capacitance of a pore with a certain pore size. The time constant $\tau_i = R_i \cdot C_i$ indicates how fast this pore can be accessed by the ac signal. An equivalent quantity to τ_i is the penetration depth $\lambda_i = \sqrt{\frac{Z_i}{R_i}}$. The penetration depth implies how far the ac signal at a certain frequency gets into the pore. As described in Eq. (12), the pore resistance R_i is indirectly proportional to the pore radius. Therefore the smaller the pore radius, the larger is the pore resistance and the time constant and the smaller is the penetration depth [36,37,38,39]. In Fig. 55 these facts are summarized. Using only few RC elements can therefore be seen as averaging over the different pore radii of the pore structure.

Since the pore resistance is indirectly proportional to the pore radius, the R_i values decrease after coarsening. This can be seen by comparing Fig. 33c with 33d and Fig. 34c with 34d.

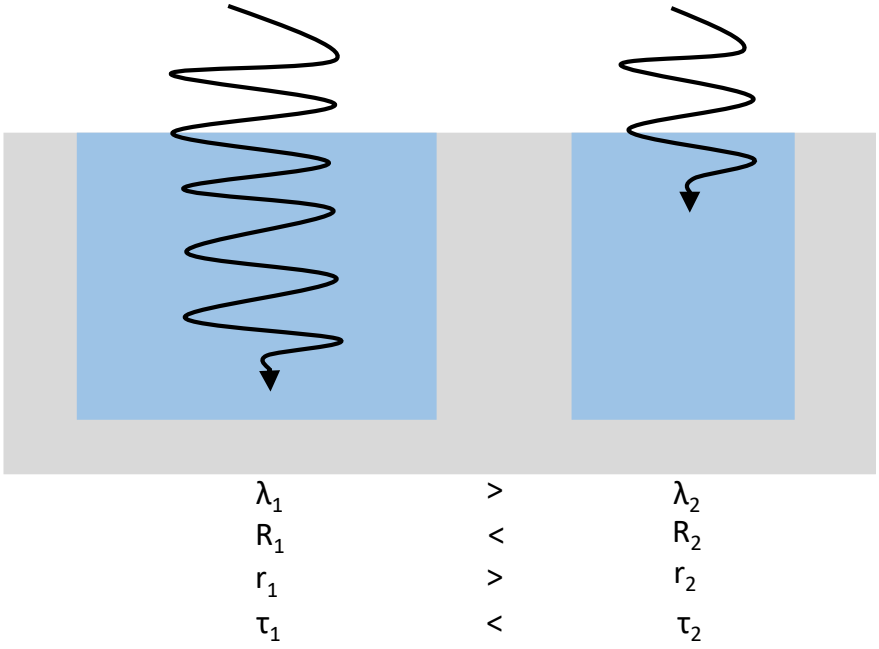

Figure 55: Variation of penetration length λ of ac signal with structural pore parameters (schematically). $r_{1,2}$: pore radius; $R_{1,2}$: pore resistance; $\tau_{1,2}$: time constant.

5.2.3 Calculation of Pore Volume and Macroscopic Sample Thickness

The macroscopic thickness of the nanoporous electrode can approximately be calculated from the volume change during dealloying via:

$$\frac{\Delta V_{\text{alloy}}}{V_{\text{alloy}}} \approx 3 \cdot \frac{\Delta d_{\text{alloy}}}{d_{\text{alloy}}}, \tag{42}$$

which holds for small dimensional changes of an isotropic solid. With the volume change of approximately 30%[40] ($\Delta V_{\text{alloy}} = 0.3 \cdot V_{\text{alloy}}$), a thickness change of 10% occurs. The macroscopic thicknesses of the nanoporous samples after dealloying can therefore be estimated by:

$$d_{\text{np}} = 0.9 \cdot d_{\text{alloy}} \tag{43}$$

In Table 9, the measured thickness of the initial alloy d_{alloy} and the macroscopic sample thickness of the nanoporous sample d_{np} with their uncertainties Δd_{alloy} and Δd_{np} are listed. Since the npAu sample 1 (dealloyed in H_2SO_4) and npAu sample 2 (dealloyed in $HClO_4$) have the same initial alloy thickness, also the macroscopic thickness of the nanoporous sample is approximately the same.

Table 9: Measured thickness of the initial alloy d_{alloy} and the macroscopic thickness of the nanoporous sample d_{np} with their uncertainties Δd_{alloy} and Δd_{np}.

sample	d_{alloy} / μm	Δd_{alloy} / μm	d_{np} / μm	Δd_{np} / μm
npAu	170	10	153	11
npPd	250	10	225	11

The total volume of the pores V_{pore} is a central factor for the calculation of the pore radius, but very difficult to determine experimentally. Therefore, an estimation was made based on the volume of the alloy before dealloying which can easily be measured. For a silver gold and for a cobalt palladium alloy a macroscopic shrinkage of up to 30 % during the electrochemical dealloying was reported[40,41]. Therefore the total macroscopic volume of the nanoporous sample V_{np} was estimated as 70% of the initial volume of the alloy V_{alloy}:

$$V_{\text{np}} = 0.7 \cdot V_{\text{alloy}}. \tag{44}$$

Since during the dealloying process a nanoporous structure is formed in a self-similar way[42,43], the final pore volume V_{pore} can roughly be estimated as the half total macroscopic volume of the nanoporous sample[44]:

$$V_{\text{pore}} = \frac{V_{\text{np}}}{2}^{2}. \tag{45}$$

In Table 10, the values of the measured volume of the initial alloy V_{alloy}, the macroscopic nanoporous volume V_{np} and the pore volume V_{pore} with their uncertainties ΔV_{alloy}, ΔV_{np} and ΔV_{pore} are listed. Since no change in the pore volume is assumed due to coarsening, V_{pore} stays the same for the coarsened nanoporous gold samples.

Table 10: Measured volume of the initial alloy V_{alloy}, the macroscopic nanoporous volume V_{np} and the pore volume V_{pore} with their uncertainties ΔV_{alloy}, ΔV_{np} and ΔV_{pore}.
npAu 1: npAu sample dealloyed in H_2SO_4 (Fig. 33a); npAu 2: npAu sample dealloyed in $HClO_4$ (Fig. 22); npPd: sample of Fig. 30a;

sample	V_{alloy} / mm^3	ΔV_{alloy} / mm^3	V_{np} / mm^3	ΔV_{np} / mm^3	V_{pore} / mm^3	ΔV_{pore} / mm^3
npAu 1	2.6	0.8	1.8	0.6	0.9	0.3
npAu 2	5.1	1.2	3.6	0.8	1.8	0.4
npPd	3.8	1.2	2.7	0.8	1.4	0.4

[2]By assuming a mass change due to dealloying of 65%, which is indeed the case for the used alloys, and a volume change of 70%, V_{pore} can also be estimated as followed:
$\frac{m_{\text{np}}}{m_{\text{alloy}}} = 0.35 = \frac{V_{\text{lig}}}{V_{\text{alloy}}} \rightarrow \frac{V_{\text{np}}}{V_{\text{alloy}}} = \frac{V_{\text{pore}}}{V_{\text{alloy}}} + \frac{V_{\text{lig}}}{V_{\text{alloy}}} \rightarrow 0.7 = \frac{V_{\text{pore}}}{V_{\text{alloy}}} + 0.35 \rightarrow V_{\text{pore}} = 0.35 \cdot V_{\text{alloy}}$

5.2.4 Pore Parameters (Radius, Length and Number of Pores)

Via electrochemical impedance spectroscopy an estimation of the pore radius, the pore length and the number of pores is possible. The corresponding formulas for the calculation are given in Sect. 2.4.2 in Eq. (33), (34) and (35). Theses formulas describe cylindrical pores and, therefore, provide not more than average values for non-cylindrical systems.

The values needed for the calculation of the pore parameters are listed in Table 11. By using Eq. (33), (34) and (35) and the values of Table 11, the pore radius, the pore length, and the number of pores are calculated. The obtained results are shown in Table 12.

Table 11: Values required for the calculation of the pore parameters. Data taken from Table 7, 8 and 10.
npAu 1: nanoporous gold sample dealloyed in H_2SO_4 (Fig. 33a); npAu 1 (c): npAu 1 sample aged due to a variety of electrochemical treatments (Fig. 33b); npAu 2: nanoporous gold sample dealloyed in $HClO_4$ (Fig. 22); npAu 2 (c): npAu 2 sample coarsened at 150°C for 2 h (Fig. 34b); npPd: nanoporous palladium sample dealloyed in H_2SO_4 (Fig. 30a).

sample	V_{pore} / mm^3	ΔV_{pore} / mm^3	A / cm^2	R_Ω / Ω	ΔR_Ω / Ω
npAu 1	0.9	0.3	1200 - 1800	70	10
npAu 1 (c)	0.9	0.3	900 - 1400	25	10
npAu 2	1.8	0.4	2200 - 3400	45	10
npAu 2 (c)	1.8	0.4	900 - 1400	32	100
npPd	1.4	0.4	6400 - 12400	111	10

Table 12: Calculated pore radius r_{pore}, pore length l_{pore} and number of pores n per cm^2. For the calculation of l_{pore} (Eq. 34) the electrolyte conductivity $\sigma = (5.65 \pm 0.01)\ \frac{\mathrm{mS}}{\mathrm{cm}}$ of 10 mM $HClO_4$ is used. The abbreviations of the samples are the same as in Table 11.

sample	r_{pore} / nm	l_{pore} / μm	Δl_{pore} / μm	n / $10^6 \cdot$ cm^{-2}
npAu 1	10 – 15	330	80	3.2 – 4.8
npAu 1 (c)	16 – 25	200	70	3.2 – 5.0
npAu 2	11 – 16	370	50	2.7 – 3.9
npAu 2 (c)	26 – 39	310	80	1.3 – 2.0
npPd	2 – 4	510	90	7.8 – 15.6

As already discussed in Sect. 5.1.4, for the specific double layer capacitance C_{dl} a variety of values is found in literature. As a result, a total surface area window, calculated via Eq. (30), is obtained. For the npAu 1 sample, e.g., A is about 1200 – 1800 cm^2. Since for the calculation of the pore radius r_{pore} (Eq. (33)) and the number of pores n (Eq. (35)) the total surface area is needed, a r_{pore} and a n window is received too. For the npAu 1 sample, e.g., r_{pore} is about 10 – 15 nm. The pore length is independent of the specific double layer capacitance and therefore the error Δl_{pore} is calculated following the rules of uncertainty propagation.

The calculated pore parameters of the coarsened nanoporous gold samples (Table 12) are in very good accordance, although two different electrolytes are used for the formation of the nanoporous structure. By comparing the obtained results of Table 12 with literature, a pore radius of about 20 nm and a number of pores of about $6 \cdot 10^{10}$ cm^{-2} for nanoporous gold were found by Cattarin et al.[30]. The pore radius is in very good agreement with literature, whereas the number of pores is too low. For this discrepancy in the number of pores, no explanation was found. Kelly et al.[25] estimated a pore radius of 9 nm and a number of pores of 10^{11} cm^{-2} following the model of Keiser. Again r_{pore} is in fairly good agreement with literature. The number of pores per cm^2 is again lower. For this lower number of pores no possible explanation was found.

The structural pore parameters change upon coarsening (Table 12). As already discussed in Sect. 5.1.4, the temperature plays a major role during the coarsening process and strongly effects the degree of coarsening[25]. The pore radius of the npAu 1 sample aged due to a variety of electrochemical treatments increased not so much as the npAu 2 sample coarsened at 150°C. The pore length decreases slightly and the number of pores stays almost the same.

The increase of the pore radius due to coarsening is in good accordance with literature. As discussed by Kelly et al.[25], a lower aging temperature has little effect on the average pore parameters because the finest pores, which coarsen at such temperatures, make up a small fraction only of the total surface area. The higher aging temperature affects the finest pores as well as larger pores[25]. Therefore, a major change in the pore parameters can be observed.

The calculated pore radius of the nanoporous palladium sample is slightly too low. In literature, values between 5 and 20 nm for npPd fabricated by dealloying $Co_{80}Pd_{20}$ were found[45]. Since the rough approximation for the calculation of the pore volume (Sect. 5.2.3) does not show an effect on the calculated values of the nanoporous gold samples, it is assumed that V_{pore} also has no influence on the results for the nanoporous palladium samples. Instead it is suggested that the deviation from the values cited in literature are caused by the approximations made during the determination of the total surface area, which has been already discussed in detail in Sect. 5.1.4. This assumption is based on the fact, that the specific surface area obtained via double layer measurements of a nanoporous palladium sample, prepared of the same initial alloy as the npPd sample was made of, is about 26 $\frac{\text{m}^2}{\text{g}}$. By using the corresponding total surface area A of approximately 3170 cm^2 and a V_{pore} of (1.4 ± 0.4) mm^3 (Table 11), via Eq. (33) a pore radius of about 9 nm is obtained. This r_{pore} value is in good accordance with literature[45].

5.2.5 Comparison of Ligament Size with Pore Radius

The pore volume can only be roughly estimated via the volume change during dealloying and the self-similar structure, as described in Sect. 5.2.1. Therefore the value of V_{pore} is rather uncertain. The ligament size can be calculated without knowing this factor. Therefore this value can be used to check if the obtained pore radius is in the correct order of magnitude.

After Cattarin et al.[21], the ligament size d_{lig} can be calculated by taking into account only the bulk density ρ of the nanoporous material, the specific surface area α and a pore shape dependent pre-factor, which is 4 for cylindrical pores:

$$d_{\text{lig}} = \frac{4}{\rho\alpha} = 2 \cdot r_{\text{lig}}, \tag{46}$$

where r_{lig} denotes the average ligament radius.

In Table 13, the calculated ligament sizes, ligament radii and the pore radii are listed. The ligament sizes d_{lig} for nanoporous gold are in good accordance with literature, where values of $d_{\text{lig}} = 14 - 21$ nm are found[30]. By comparing r_{lig} and r_{pore}, the pore radii are larger than the ligament radii in all six cases. Although nanoporous gold is formed in more or less a self-similar way[42,43], the morphology and topology of npAu strongly depends on the composition of precursor alloys and the dealloying conditions. In the case of an $Ag_{75}Au_{25}$ alloy, a mean pore size 50% larger than the ligament size is found by Detsi et al.[46]. This ratio was determined via electron tomography studies of a dealloyed gold leaf[47,48]. Since the same alloy composition was used in this thesis as of Detsi et al.[46], similar results are expected, which indeed is the case.

Table 13: Ligament size d_{lig} and average ligament radius r_{lig} according tp Eq. 46. Bulk densities: $\rho_{\text{Au}} \approx 19\ \frac{\text{g}}{\text{cm}^3}$, $\rho_{\text{Pd}} \approx 12\ \frac{\text{g}}{\text{cm}^3}$. r_{pore} is shown for comparison, the corresponding data are taken from Table 12.

sample	$\boldsymbol{d_{\text{lig}}}$ **/ nm**	$\boldsymbol{r_{\text{lig}}}$ **/ nm**	$\boldsymbol{r_{\text{pore}}}$ **/ nm**
npAu 1	14 – 21	7 – 11	10 – 15
npAu 1 (c)	23 – 35	12 – 18	16 – 25
npAu 2	15 – 23	8 – 12	11 – 16
npAu 2 (c)	35 – 53	18 – 27	26 – 39
npPd	3 – 6	2 – 3	2 – 4

Although the calculated pore radius of the nanoporous palladium sample is too small (see Sect. 5.2.4), the ligament size is in good accordance with the pore size. Therefore r_{lig} and r_{pore} are caused by the same error. This error is the surface area. As the total capacitance C_{tot} of palladium is determined in the same way as for the gold samples, the deviation of the specific surface area α may arise from the adapted specific double layer capacitance of Pd in H_2SO_4. So for the calculation of the pore structure parameters, the specific double layer capacitance in

$HClO_4$ should be determined for palladium, or an electrolyte has to be used for which C_{dl} is known, e.g. sulfuric acid.

Summarizing, by comparing r_{lig} and r_{pore}, the assumption made in Sect. 5.2.3 for the calculation of the pore volume lead to correct values of r_{pore} and can therefore be used for approximating V_{pore}.

5.2.6 Pore Length and Tortuosity

The calculated pore lengths l_{pore} (Table 12) are much longer than the macroscopic thickness of the nanoporous sample d_{np} (Table 9). This is an indication for tortuous pores. In the simplest case, the tortuosity τ of a porous electrode material is the ratio of the microscopic path length l_{pore} normalized by the Cartesian distance d_{np} between the endpoints of the path[49]:

$$\tau = \frac{l_{\mathrm{pore}}}{d_{\mathrm{np}}}. \tag{47}$$

The calculated values of the tortuosity are listed in Table (14).

Table 14: Tortuosity τ obtained from Eq. 47 with the following parameters. Pore length l_{pore}: data from Table 12; macroscopic sample thicknesses: d_{npAu} = (153±11) μm and d_{npPd} = (225 ± 11) μm; (c) denotes the coarsened state.

sample	$\boldsymbol{\tau}$	$\boldsymbol{\Delta\tau}$
npAu 1	2.16	0.68
npAu 1 (c)	1.31	0.55
npAu 2	2.42	0.50
npAu 2 (c)	2.03	0.67
npPd	2.27	0.51

In addition to the tortuosity, the **porosity** plays an important role. After the definition of Gibson and Ashby[50], the porosity ϵ is the fraction of the pore space in the nanoporous foam. Simply spoken: $\epsilon = 1 - \frac{\rho^*}{\rho_{\mathrm{s}}}$, where ρ^* is the nanoporous foam density, ρ_{s} the density of the solid and $\frac{\rho^*}{\rho_{\mathrm{s}}}$ the relative density[50]. Based on this definition, ϵ is estimated by replacing the relative density by the fraction of the ligament volume $V_{\mathrm{lig}} = \frac{m_{np}}{\rho_{\mathrm{bulk}}}$ and the macroscopic volume $V_{\mathrm{mac}} = 0.7 \cdot \frac{m_{\mathrm{alloy}}}{\rho_{\mathrm{alloy}}}$ of the nanoporous structure:

$$\epsilon = 1 - \frac{\rho_{\mathrm{alloy}}}{0.7 \cdot \rho_{\mathrm{bulk}}} \cdot \frac{m_{\mathrm{np}}}{m_{\mathrm{alloy}}}. \tag{48}$$

In this expression, m_{np} is the mass of the electrodes after dealloying, ρ_{bulk} the density of the bulk material and m_{alloy} and ρ_{alloy} denotes the mass and the density of the initial alloy.

Table 15: Porosity ϵ obtained from Eq. 48 with the following parameters. Densities: $\rho_{\text{alloy,AgAu}}$ = 12.7 $\frac{\text{g}}{\text{cm}^3}$, $\rho_{\text{alloy,CoPd}}$ = 9.6 $\frac{\text{g}}{\text{cm}^3}$, $\rho_{\text{bulk,Au}}$ = 19.3 $\frac{\text{g}}{\text{cm}^3}$, $\rho_{\text{bulk,Pd}}$ = 12.0 $\frac{\text{g}}{\text{cm}^3}$; Masses: $m_{\text{AgAu1}} = (31.94 \pm 0.01)$ mg, $m_{\text{AgAu2}} = (66.60 \pm 0.01)$ mg, $m_{\text{CoPd1}} = (32.50 \pm 0.01)$ mg and $m_{\text{CoPd2}} = (31.62 \pm 0.01)$ mg; (c) denotes the coarsened state.

sample	$\boldsymbol{\epsilon}$	$\boldsymbol{\Delta\epsilon}$
npAu 1	0.64	0.03
npAu 1 (c)	0.64	0.03
npAu 2	0.64	0.02
npAu 2 (c)	0.64	0.02
npPd	0.58	0.04

Changes in the porosity are reported to occur only above 800°C, due to sintering[51]. Therefore it is assumed that the porosity stays the same for the coarsened npAu 1 and npAu 2 samples, where temperatures far below 800°C are used. Since no density value in literature was found for $Co_{75}Pd_{25}$, it has been calculated using the assumption of a homogeneous solid solution with specific volumes of the components. The calculated porosity value of npPd in Table 15 is smaller compared to values in literature, where ϵ is about 0.62 to 0.76[45].

The tortuosity τ, in combination with the porosity ϵ of the sample, affects the effective transport properties, as e.g. the electrolyte conductivity[52]. The effective electrolyte conductivity κ_{eff}, which has a smaller value than the bulk value κ_0, is described by[53]:

$$\kappa_{eff} = \kappa_0 \frac{\epsilon}{\tau}. \tag{49}$$

The reduction of the effective electrolyte conductivity relative to its corresponding bulk value can be estimated using the MacMullin number Mc[53]:

$$\frac{\kappa_{eff}}{\kappa_0} = \frac{1}{Mc} = \frac{\epsilon}{\tau}. \tag{50}$$

The MacMullin numbers are listed in Table 16. As expected, the more tortuous the pores, the larger Mc and therefore the smaller the conductivity. This means that the effective length an ion must travel through the microstructure of the pores increases[49] or the time an ion needs on his way through the pore increases.

Table 16: Calculated MacMullin number Mc (Eq. (50)) and its uncertainty ΔMc. The values of τ and ϵ are taken from Tables 14 and 15. The abbreviation c stands for coarsened.

sample	$\boldsymbol{Mc}$	$\boldsymbol{\Delta Mc}$
npAu 1	3.38	1.12
npAu 1 (c)	2.05	0.95
npAu 2	3.78	0.86
npAu 2 (c)	3.17	1.15
npPd	3.91	1.15

5.2.7 Concluding Remarks on the Pore Structure

Since nanoporous metals produced by electrochemical dealloying possess intricate and random three-dimensional morphologies[44], the pore shape determination and the calculation of the pore parameters via simple models give only a very rough estimation. The more complex methods are used for the description, the better the nanoporous structure can be analyzed.

The model after Keiser gives a first estimation of the pore shape of the nanoporous electrode (Sect. 5.2.1). Since the model following Eloot includes more possibilities of interpretation, such as the slope of the impedance loci and a shape-dependent geometry factor, this model is better suited for a accurate description. The inclined line of the impedance at low frequencies gives an estimation of the pore size distribution (Sect. 5.2.2).

The macroscopic volume (Sect. 5.2.3) of the samples after dealloying was estimated by a volume shrinkage of 30% of the alloy volume. With this sample volume, the pore radius can be calculated via Eq. (33) (Sect. 5.2.4). Since the pore volume is only a rough estimation, a comparison with the ligament size is necessary. The ligament size can be calculated without knowing the pore volume. The pore length can be calculated via Eq. (34). A larger pore length than the sample thickness is an indication for tortuous pores (Sect. 5.2.6). This tortuosity reduces the conductivity within the pores. Depending on the degree of coarsening, a more or less intense change in the pore parameters is observed.

6 Conclusion

Electrochemical impedance spectroscopy (EIS) is a well established measurement technique for investigating nanoporous metal systems obtained by electrochemical dealloying. In this master's thesis, **EIS** was **introduced at** the **Institute of Materials Physics**. Since nanoporous gold is the most intensively studied dealloyed system, most investigations were made on this material. For comparison measurements on nanoporous palladium were made. The results were extensively discussed with respect to literature as well as with CV double layer measurements, which is a well established method at the Institute of Materials Physics.

The advantages of the EIS method lie in the detailed comparison of the fitted equivalent circuits following the theories of de Levie [18], Keiser et al. [19] and Eloot et al. [22]. This circuits were applied on the two investigated metals, in different chemical states (before and after dealloying and after electrochemical reduction) and regimes (oxygen, double layer, hydrogen). Furthermore the pore volume was approximated from the initial alloy volume by assuming a 30% volume shrinkage and a self similar structure (Sect. 5.2.3).

The $Ag_{75}Au_{25}$ and $Co_{75}Pd_{25}$ alloys have been prepared by arc melting. The nanoporous electrodes were produced by electrochemical dealloying from these initial alloys. **Impedance spectra** were **measured** before and after dealloying and after electrochemical reduction. Some nanoporous gold electrodes have also been coarsened. The measured impedance spectra have a high frequency arc. In the middle frequency part, the shape of the spectrum is very sensitive on the used nanoporous material, the chemical state, and on the pore shape. For nanoporous gold, e.g., a quarter circular behavior is observed. Towards low frequencies a sharp bend towards a phase angle of almost 90° occurs. The spectra are fitted with different equivalent circuit models (Sect. 4.5).

In order to **assign** the **different parts of** the **spectra to** the **corresponding circuit elements**, the high frequency arc was found to be caused by the contact impedance between the nanoporous electrode and the wire, which serves as current collector (Sect. 5.1.1). The remaining spectrum is fitted by the transmission line models after de Levie [18] and Keiser et al. [19] and Eloot et al. [22] (Sect. 5.1.2). After coarsening, a significant change in the impedance spectra can be observed. As a consequence also the fitted equivalent circuits change (Sect. 4.5).

The **total capacitance** $\boldsymbol{C_{\mathrm{tot}}}$ and the **pore resistance** $\boldsymbol{R_{\mathrm{pore}}}$ have been **calculated** from the transmission line (Table 2, Fig. 47). For the nanoporous gold samples, the calculated C_{tot} is in very good agreement with CV double layer measurements and with literature (Sect. 5.1.4). Since for the nanoporous palladium samples an approximated specific double layer capacitance was used, the C_{tot} values show some discrepancies with CV double layer measurements and with literature (Sect. 5.1.4). The pore resistance calculated from the fitted equivalent circuit is very

sensitive on the number of RC elements, whereas the R_{pore} value estimated via the impedance spectrum depends strongly on the approximation of the phase angle at very low frequencies. For some samples these two resistance values show some discrepancies (Table 7). The coarsened npAu samples show smaller C_{tot} and R_{pore} values, which is caused by the reduction of the total surface area and increase of the pore radius.

For nanoporous gold and palladium, the **potential dependence of the impedance spectrum** was investigated (Sect. 4.6). While the spectrum is very stable within the double layer regimes, significant changes occur in chemical active regions, especially for hydrogen absorption in npPd.

Independent of the electrolyte used for the dealloying process, for the nanoporous gold electrodes a rhombohedral **pore shape**, with a pore mouth radius slightly bigger than the radius deep inside the pore, was found. Due to coarsening, the pore shapes of the npAu samples changed to more cylindrical ones. For npPd a deltoid like shape is suggested (Sect. 5.2.1).

The **pore radius** of the nanoporous gold electrode dealloyed in H_2SO_4 (npAu 1) is 10 – 15 nm and for the electrode dealloyed in $HClO_4$ (npAu 2) 9 – 14 nm. These values are again in very good agreement with literature. Due to coarsening, the pore radius of the two nanoporous gold samples increased (Table 12). The npPd sample has a pore radius of about 2 – 4 nm. This value of r_{pore} is slightly too low in comparison with literature which is probably caused by the approximation of the specific double layer capacitance.

Since the pore lengths of the samples (Table 12) are much longer than the macroscopic lengths (Table 9), it is assumed that the pores are tortuous. This **tortuosity** (Table 14) lowers the effective electrolyte conductivity within the pores.

In conclusion, EIS turns out as a powerful supplementary tool in the research field of nanoporous metals prepared by dealloying.

References

[1] L. G. Max and Z. X. Song. *Nanoporous materials: science and engineering.* World Scientific (2004).

[2] B. Tappan, S. Steiner and E. Luther. Nanoporous metal foams. *Angewandte Chemie International Edition*, **49** (2010) 4544. doi:10.1002/anie.200902994.

[3] I. McCue, E. Benn, B. Gaskey and J. Erlebacher. Dealloying and dealloyed materials. *Annual Review of Materials Research*, **46** (2016) 263. doi:10.1146/annurev-matsci-070115-031739.

[4] R. K. Singh, R. Ramesh, R. Devivaraprasad, A. Chakraborty and M. Neergat. Hydrogen interaction (electrosorption and evolution) characteristics of pd and pd3co alloy nanoparticles: An in-situ investigation with electrochemical impedance spectroscopy. *Electrochimica Acta*, **194** (2016) 199 . doi:10.1016/j.electacta.2016.01.231.

[5] M. Grdeń, M. Łukaszewski, G. Jerkiewicz and A. Czerwiński. Electrochemical behaviour of palladium electrode: oxidation, electrodissolution and ionic adsorption. *Electrochimica Acta*, **53** (2008) 7583. doi:10.1016/j.electacta.2008.05.046.

[6] L. lan Fang, Q. Tao, M. fang Li, L. wen Liao, D. Chen and Y. xia Chen. Determination of the real surface area of palladium electrode. *Chinese Journal of Chemical Physics*, **23** (2010) 543. doi:10.1088/1674-0068/23/05/543-548.

[7] D. D. Macdonald. Reflections on the history of electrochemical impedance spectroscopy. *Electrochimica Acta*, **51** (2006) 1376. doi:10.1016/j.electacta.2005.02.107.

[8] W. Schmickler and E. Santos. *Interfacial electrochemistry.* Springer Science & Business Media (2010).

[9] C. H. Hamann and W. Vielstich. *Elektrochemie 3.Auflage.* Wiley/VCH Verlag, Weinheim (1998).

[10] A. A. Isse and A. Gennaro. Absolute potential of the standard hydrogen electrode and the problem of interconversion of potentials in different solvents. *The Journal of Physical Chemistry B*, **114** (2010) 7894. doi:10.1021/jp100402x.

[11] Q. Chen and K. Sieradzki. Spontaneous evolution of bicontinuous nanostructures in dealloyed li-based systems. *Nature materials*, **12** (2013) 1102. doi:10.1038/NMAT3741.

[12] M. E. Orazem and B. Tribollet. *Electrochemical impedance spectroscopy.* John Wiley & Sons (2011).

[13] D. A. Harrington and P. van den Driessche. Mechanism and equivalent circuits in electrochemical impedance spectroscopy. *Electrochimica Acta*, **56** (2011) 8005. doi:10.1016/j.electacta.2011.01.067.

[14] B. Hirschorn, M. E. Orazem, B. Tribollet, V. Vivier, I. Frateur and M. Musiani. Determination of effective capacitance and film thickness from constant-phase-element parameters. *Electrochimica Acta*, **55** (2010) 6218. doi:10.1016/j.electacta.2009.10.065.

[15] R. de Levie. On porous electrodes in electrolyte solutions—IV. *Electrochimica Acta*, **9** (1964) 1231. doi:10.1016/0013-4686(64)85015-5.

[16] J. Landesfeind, D. Pritzl and H. A. Gasteiger. An Analysis Protocol for Three-Electrode Li-Ion Battery Impedance Spectra: Part I. Analysis of a High-Voltage Positive Electrode. *Journal of The Electrochemical Society*, **164** (2017) A1773. doi:10.1149/2.0131709jes.

[17] N. Ogihara, Y. Itou, T. Sasaki and Y. Takeuchi. Impedance spectroscopy characterization of porous electrodes under different electrode thickness using a symmetric cell for high-performance lithium-ion batteries. *The Journal of Physical Chemistry C*, **119** (2015) 4612. doi:10.1021/jp512564f.

[18] R. de Levie. On porous electrodes in electrolyte solutions: I. capacitance effects. *Electrochimica Acta*, **8** (1963) 751. doi:10.1016/0013-4686(63)80042-0.

[19] H. Keiser, K. Beccu and M. Gutjahr. Abschätzung der Porenstruktur poröser Elektroden aus Impedanzmessungen. *Electrochimica Acta*, **21** (1976) 539. doi:10.1016/0013-4686(76)85147-X.

[20] J.-P. Candy, P. Fouilloux, M. Keddam and H. Takenouti. The characterization of porous electrodes by impedance measurements. *Electrochimica Acta*, **26** (1981) 1029. doi:10.1016/0013-4686(81)85072-4.

[21] S. Cattarin, D. Kramer, A. Lui and M. M. Musiani. Preparation and characterization of gold nanostructures of controlled dimension by electrochemical techniques. *The Journal of Physical Chemistry C*, **111** (2007) 12643. doi:10.1021/jp072405c.

[22] K. Eloot, F. Debuyck, M. Moors and A. P. Van Peteghem. Calculation of the impedance of noncylindrical pores Part I: Introduction of a matrix calculation method. *Journal of Applied Electrochemistry*, **25** (1995) 326. doi:10.1007/BF00249650.

[23] O. Poupard, A. Aït-Mokhtar and P. Dumargue. Impedance spectroscopy in reinforced concrete: Procedure for monitoring steel corrosion part i development of the experimental device. *Journal of Materials Science*, **38** (2003) 2845. doi:10.1023/A:1024428317968.

[24] Methrom. Impedance spectroscopy tutorial.

[25] R. G. Kelly, A. J. Young and R. C. Newman. The characterization of the coarsening of dealloyed layers by eis and its correlation with stress-corrosion cracking. In *Electrochemical impedance: analysis and interpretation*. ASTM International (1993).

[26] E.-M. Steyskal, C. Wiednig, N. Enzinger and R. Würschum. In situ characterization of hydrogen absorption in nanoporous palladium produced by dealloying. *Beilstein journal of nanotechnology*, **7** (2016) 1197. doi:10.3762/bjnano.7.110.

[27] Y. Qu, T. F. Baumann, J. G. Santiago and M. Stadermann. Characterization of resistances of a capacitive deionization system. *Environmental Science & Technology*, **49** (2015) 9699. doi:10.1021/acs.est.5b02542.

[28] J. Bisquert. Influence of the boundaries in the impedance of porous film electrodes. *Physical Chemistry Chemical Physics*, **2** (2000) 4185. doi:10.1039/B001708F.

[29] A. J. Zhang, V. I. Birss and P. Vanýsek. Impedance characterization of thin electrochemically formed palladium oxide films. *Journal of Electroanalytical Chemistry*, **378** (1994) 63. doi:https://doi.org/10.1016/0022-0728(94)87057-8.

[30] S. Cattarin, D. Kramer, A. Lui and M. Musiani. Formation of nanostructured gold sponges by anodic dealloying. EIS investigation of product and process. *Fuel Cells*, **9** (2009) 209. doi:10.1002/fuce.200800075.

[31] B. Roling and M. Drüschler. Comments on "Intrinsic limitations of impedance measurements in determining electric double layer capacitances" by H. Wang and L. Pilon [Electrochim. Acta 63 (2012) 55]. *Electrochimica Acta*, **76** (2012) 526. doi:10.1016/j.electacta.2012.03.180.

[32] J. Zheng, P. Goonetilleke, C. Pettit and D. Roy. Probing the electrochemical double layer of an ionic liquid using voltammetry and impedance spectroscopy: A comparative study of carbon nanotube and glassy carbon electrodes in [EMIM]+[EtSO4]-. *Talanta*, **81** (2010) 1045. doi:10.1016/j.talanta.2010.01.059.

[33] J. Clavilier and C. N. V. Huong. Etude de l'interface de l'or polycristallin au contact de solutions aqueuses de perchlorate de potassium et d'acide perchlorique. *Journal of Electro-*

analytical Chemistry and Interfacial Electrochemistry, **80** (1977) 101 . doi:10.1016/S0022-0728(77)80106-X.

[34] E. Hengge. Private communication.

[35] H.-K. Song, Y.-H. Jung, K.-H. Lee and L. H. Dao. Electrochemical impedance spectroscopy of porous electrodes: the effect of pore size distribution. *Electrochimica Acta*, **44** (1999) 3513. doi:10.1016/S0013-4686(99)00121-8.

[36] H.-K. Song, H.-Y. Hwang, K.-H. Lee and L. H. Dao. The effect of pore size distribution on the frequency dispersion of porous electrodes. *Electrochimica Acta*, **45** (2000) 2241. doi:10.1016/S0013-4686(99)00436-3.

[37] M.-S. Wu and P.-C. J. Chiang. Fabrication of nanostructured manganese oxide electrodes for electrochemical capacitors. *Electrochemical and solid-state letters*, **7** (2004) A123. doi:10.1149/1.1695533.

[38] D. Qu and H. Shi. Studies of activated carbons used in double-layer capacitors. *Journal of Power Sources*, **74** (1998) 99. doi:10.1016/S0378-7753(98)00038-X.

[39] J. M. Black and H. A. Andreas. Pore shape affects spontaneous charge redistribution in small pores. *The Journal of Physical Chemistry C*, **114** (2010) 12030. doi:10.1021/jp103766q.

[40] S. Parida, D. Kramer, C. A. Volkert, H. Rösner, J. Erlebacher and J. Weissmüller. Volume change during the formation of nanoporous gold by dealloying. *Phys. Rev. Lett.*, **97** (2006) 035504. doi:10.1103/PhysRevLett.97.035504.

[41] M. Goezsler. Hydrogen Storage and Actuation Properties of Nanoporous Palladium Prepared by Dealloying, Master Thesis. (2017). Technische Universität Graz.

[42] H. Jeon, N.-R. Kang, E.-J. Gwak, J. il Jang, H. N. Han, J. Y. Hwang, S. Lee and J.-Y. Kim. Self-similarity in the structure of coarsened nanoporous gold. *Scripta Materialia*, **137** (2017) 46. doi:10.1016/j.scriptamat.2017.05.009.

[43] Y. Ding and J. Erlebacher. Nanoporous metals with controlled multimodal pore size distribution. *Journal of the American Chemical Society*, **125** (2003) 7772. doi:10.1021/ja035318g.

[44] T. Fujita, L.-H. Qian, K. Inoke, J. Erlebacher and M.-W. Chen. Three-dimensional morphology of nanoporous gold. *Applied Physics Letters*, **92** (2008) 251902. doi:10.1063/1.2948902.

[45] M. Hakamada and M. Mabuchi. Fabrication of nanoporous palladium by dealloying and its thermal coarsening. *Journal of Alloys and Compounds*, **479** (2009) 326. doi:10.1016/j.jallcom.2008.12.078.

[46] E. Detsi, M. van de Schootbrugge, S. Punzhin, P. Onck and J. D. Hosson. On tuning the morphology of nanoporous gold. *Scripta Materialia*, **64** (2011) 319 . doi:10.1016/j.scriptamat.2010.10.023.

[47] X. Lang, H. Yuan, Y. Iwasa and M. Chen. Three-dimensional nanoporous gold for electrochemical supercapacitors. *Scripta Materialia*, **64** (2011) 923 . doi:10.1016/j.scriptamat.2011.01.038.

[48] H. Rösner, S. Parida, D. Kramer, C. Volkert and J. Weissmüller. Reconstructing a nanoporous metal in three dimensions: An electron tomography study of dealloyed gold leaf. *Advanced Engineering Materials*, **9** (2007) 535. doi:10.1002/adem.200700063.

[49] J. Landesfeind, J. Hattendorff, A. Ehrl, W. A. Wall and H. A. Gasteiger. Tortuosity determination of battery electrodes and separators by impedance spectroscopy. *Journal of The Electrochemical Society*, **163** (2016) A1373. doi:10.1149/2.1141607jes.

[50] L. J. Gibson and M. F. Ashby. *Cellular solids: structure and properties*. Cambridge University Press (1999).

[51] Y. chen Karen Chen-Wiegart, S. Wang, Y. S. Chu, W. Liu, I. McNulty, P. W. Voorhees and D. C. Dunand. Structural evolution of nanoporous gold during thermal coarsening. *Acta Materialia*, **60** (2012) 4972 . doi:10.1016/j.actamat.2012.05.012.

[52] I. V. Thorat, D. E. Stephenson, N. A. Zacharias, K. Zaghib, J. N. Harb and D. R. Wheeler. Quantifying tortuosity in porous Li-ion battery materials. *Journal of Power Sources*, **188** (2009) 592 . doi:10.1016/j.jpowsour.2008.12.032.

[53] E. R. Reale and K. C. Smith. Capacitive performance and tortuosity of activated carbon electrodes with macroscopic pores. *Journal of The Electrochemical Society*, **165** (2018) A1685. doi:10.1149/2.0601809jes.

Acknowledgements

I would like to sincerely thank the following persons for their contributions to the success of this master's thesis:

Univ.-Prof. Dr. Roland Würschum, Institute of Materials Physics, TU Graz
For giving me the opportunity to write this master's thesis at the Institute of Materials Physics and for the supervision of this project. His large knowledge in the field of nanomaterials and his valuable comments and inputs during the project considerable improved this thesis.

Dr. Eva-Maria Steyskal, Institute of Materials Physics, TU Graz
For co-supervising this master's thesis and for introducing me into this fascinating field of dealloyed metals. Her vast knowledge in electrochemistry, the professional discussion and her help concerning the interpretation of the measurement results were incredible helpful during the writing of this thesis.

Dipl.-Ing. Markus Gößler, Institute of Materials Physics, TU Graz
For the close, excellent, and patient cooperation in the first months, for introducing me to the different electrochemical measurement techniques and for solving many issues in the laboratory. Many discussions and his critical analysis of the measurement results have been essential for the success of this master's thesis.

Dipl.-Ing. Elisabeth Hengge, Institute of Materials Physics, TU Graz
For the very good cooperation during the investigations of some nanoporous electrodes.

My colleagues at the Institute of Materials Physics, TU Graz
For the warm welcome at the institute and for the nice working atmosphere.

My family
For their support during my studies. In particular I would like to thank my mother Klaudia and my girlfriend Julia for their patience and their encouragement especially before exams and difficult moments during my studies.